Measurement of the Spin Structure Function G(2) X Q(2) for the Neutron[*]

David E. Reyna

Stanford Linear Accelerator Center
Stanford University
Stanford, CA 94309

SLAC-Report-662
April 1998

---

[*] Ph.D. thesis, American University, Washington D.C. 20016

MEASUREMENT OF THE SPIN STRUCTURE FUNCTION

$g_2(x, Q^2)$ FOR THE NEUTRON

by

David E. Reyna

submitted to the

Faculty of the College of Arts and Sciences

of American University

in Partial Fulfillment of

the Requirements for the Degree

of

Doctor of Philosophy

in

Physics

Chairman:

_____

Raymond G. Arnold

_____

Peter Bosted

_____

Dean of the College

Stephen E. Rock

_____

Date

_____

Zenon M. Szalata

2003

American University

Washington, D.C. 20016

MEASUREMENT OF THE SPIN STRUCTURE FUNCTION $g_2(x, Q^2)$

FOR THE NEUTRON

BY

David E. Reyna

ABSTRACT

The asymmetry $A_2(x, Q^2)$ and structure function $g_2(x, Q^2)$ were measured for the neutron using deep inelastic electron scattering. The measurement was made using the 50 GeV longitudinally polarized electron beam at the Stanford Linear Accelerator Center. The target consisted of gaseous ^{3}He which was polarized through spin exchange with optically pumped rubidium vapor. Data were taken simultaneously with two magnetic spectrometers fixed at 2.75° and 5.5° scattering angles, covering a combined kinematic range of $0.014 \leq x \leq 0.7$ and $1.0 \leq Q^2 \leq 17.0$ $(\text{GeV/c})^2$. The A_2 data were found to be well bounded by the positivity constraint $|A_2| \leq \sqrt{R}$, and most of the data were consistent with zero. The g_2 structure function was found to be consistent with zero and with the twist-2 Wandzura-Wilczek prediction. In addition, the Operator Product Expansion twist-3 matrix element d_2 was calculated from the data and found to be consistent with all theoretical predictions.

ACKNOWLEDGMENTS

This document is the product of many hours of love, sweat, and tears. While I can claim great familiarity with all three, a large number of these hours were not mine. To all those whose efforts made this experiment possible, whether explicitly named or not, I offer my sincerest thanks.

In particular, I offer my extreme gratitude to the American University group at SLAC: Ray Arnold, Peter Bosted, Steve Rock, and Zen Szalata. Each one of you has freely shared your time and experience with me. In addition, your unique relationship with End Station A has provided a learning environment which I think is unparalleled for education in all aspects of this field.

I would like to thank all eighty-three members of the E154 collaboration and the SLAC technicians for making this experiment work. I would especially like to offer my respect and appreciation to the other thesis students on this experiment, Steve Churchwell, Sebastien Incerti, Yury Kolomensky, Michael Olson, Michael Romalis, Frank Sabatie, Todd Smith, Jason Wang, and Piotr Zyla. Everyone knows that graduate students are the real backbone of an experiment, and I'll take this group over any other. My appreciation for your skill and effort is surpassed only by my gratitude for your friendship. We really had something special. I must also

is largely a function of three very special people: Cherie Goodenough, Greg Mitchell, and Jim Quigley. What started on a softball diamond grew into our special club. Your friendship and support have always been there, in spades, and for that you will always be in my heart.

Finally, I would like to thank my family who really laid the foundations for all of this to be possible. To my mother, who has always been there with love and support, and my father who taught me to think, long before I ever knew I'd need to, I am truly grateful for all you have given over these many years.

CONTENTS

LIST OF TABLES

LIST OF FIGURES

CHAPTER 1

INTRODUCTION

For over twenty years, the Standard Model has provided an explanation of our universe that is consistent with experimental results. The Standard Model relies on two very fundamental ideas. First, all matter is composed of fermions (fundamental constituent particles with a spin of $\frac{1}{2}$). There are two types of these fermions: **leptons**, which carry an integer electric charge, such as the electron, and **quarks**, which carry a fractional electric charge $(+\frac{2}{3}e$ or $-\frac{1}{3}e)$. Second, fermions can interact by the exchange of bosons (particles with integer spin). Bosons are the carriers of what we normally call forces or fields of which there are 4 types (gravity, the weak nuclear force, the electro-magnetic force, and the strong force).

Free leptons have been frequently observed in nature. However, at this time, quarks have only been detected in two states: **mesons**, which are composed of quark-antiquark pairs and **baryons**, which are composed of three quarks (the proton and the neutron would be the most common examples of baryons). No free quarks have ever been detected. According to the Standard Model, these observations are a consequence of the nature of the strong force which dominates quark-quark interactions. Since our macroscopic universe is almost entirely made up of atoms which, in turn, are composed of proton and neutron combinations, it is important

that we better understand the properties of the strong force.

The theoretical description of the strong force is the theory of Quantum Chromodynamics (QCD). While QCD is very mathematically complete, several properties of the theory make it very difficult to fully compute real physical processes. The strength of the strong force, for example, grows with increasing distance between the participating particles. In contrast to the $\frac{1}{r^2}$ behavior seen in most macroscopic forces (gravity and electro-magnetic), it is difficult to isolate short-range strong interactions from their external environment. As a result, most predictions of measurable quantities involve the use of perturbative QCD (pQCD) in which the theoretically dominant process is calculated and everything else is treated as an infinite number of small corrections. This has proved quite successful in many applications, but it is not always possible to demonstrate that the corrections will necessarily be small, so the predictive power of pQCD is not always as strong as desired.

One of the areas in which QCD does offer an excellent test with experimental measurements concerns the spin-related structure of the nucleon. Many of the measurable spin properties of the nucleon rely on knowledge of quark distribution functions. Unfortunately, the nucleon quark structure can be very complicated. Under QCD, a nucleon is a combination of three quarks referred to as "valence" quarks. In addition, there exist gluons, which are the mediating bosons of the strong force. These gluons can undergo occasional virtual transitions into a quark-antiquark pair which would propagate for a short distance and recombine into the gluon. Quarks in this virtual fluctuation are referred to as "sea" quarks. It is possible to empir-

ically determine these quark distribution functions over a finite range; however, it

is impossible to make exact calculations using QCD. On the other hand, the deep

inelastic spin structure function g_2 offers a test of QCD that is calculable and is

independent of unknown quark distributions. This thesis will focus on the measure-

ment of g_2 for the neutron performed during the experiment E154 at the Stanford

Linear Accelerator Center (SLAC).

1.1   Deep Inelastic Scattering

The primary interaction of lepton deep inelastic scattering off of a nucleon

is shown in Fig. 1.1. We refer to this as deep inelastic scattering (DIS) since the
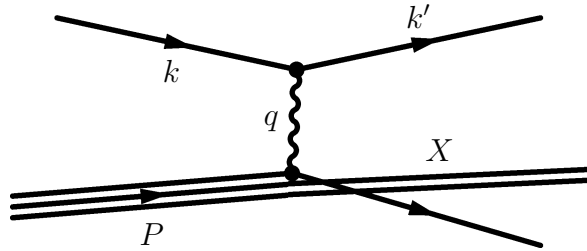
Figure 1.1: The standard DIS reaction $eN \longrightarrow e' + X$.

lepton directly probes the individual quarks independent of the rest of the nucleon.

The kinematic parameters of this reaction are defined in Table 1.1. In a laboratory

experiment the rest mass (M) of the stationary target nucleon is known. We measure

the incoming energy (E_0) of the electron beam, the outgoing energy (E') of the

scattered electron, and the scattering angle (θ) with respect to the beam direction.

From these quantities we can calculate the invariant mass (W^2) of the unmeasured

m	lepton rest mass
M	nucleon rest mass
θ	scattering angle in the laboratory[1]
$k = (E_0, \vec{k})$	four-momentum of the incident lepton
$k' = (E', \vec{k'})$	four-momentum of the scattered lepton
$P = (M, \vec{0})$	four-momentum of the target nucleon
$q = k - k'$	four momentum transfer
$\nu = E_0 - E'$	energy of the virtual photon in the laboratory
$Q^2 = -q^2 = 4E_0 E' \sin^2\left(\frac{\theta}{2}\right)$	(invariant mass)^2 of the virtual photon
$x = \frac{Q^2}{2M\nu}$	Bjorken scaling variable
$y = \frac{\nu}{E_0}$	fractional energy of the virtual photon
$\epsilon^{-1} = 1 + 2\left(1 + \frac{\nu^2}{Q^2}\right)\tan^2\left(\frac{\theta}{2}\right)$	longitudinal polarization of the virtual photon

Table 1.1: Kinematic definitions for DIS in the lab frame.

hadronic products (X), assuming the nucleon is at rest:

$$W^2 = M^2 - Q^2 + 2M\nu. \tag{1.1}$$

To insure that we have inelastic scattering, we define DIS as $W^2 > 4$ GeV^2.

From the Lagrangian, we can write the cross section for this scattering pro-

---

[1]Because we assume that the scattering plane is the same as the plane that includes the polarization vectors for the target and the incoming electrons, we define the angle ϕ between them to be zero. The $\cos(\phi)$ dependence of the cross sections can then be neglected. However, since the spectrometers in this experiment were located on either side of the axis defined by the incoming beam, for perpendicular target polarizations ϕ is actually zero for the spectrometer on the same side as the target polarization vector, and π for the spectrometer on the other side. To account for the resulting sign difference, we used $\theta = -2.75°$ and $\theta = +5.5°$ for the two spectrometers.

cess. The spin averaged part of the Lagrangian yields a cross section which is a function of two spin independent form factors, $F_1(x, Q^2)$ and $F_2(x, Q^2)$:

$$\frac{d^2\sigma}{d\Omega dE'} = \frac{4\alpha^2 (E')^2}{MQ^4} \left[2F_1(x, Q^2) \sin^2\left(\frac{\theta}{2}\right) + \frac{M}{\nu} F_2(x, Q^2) \cos^2\left(\frac{\theta}{2}\right) \right]. \tag{1.2}$$

Here α is the fine structure constant ($\alpha = e^2/4\pi \approx \frac{1}{137}$). Notice that F_1 and F_2 are both functions of the Lorentz invariants x and Q^2, which can be calculated using the measured laboratory kinematics as shown in Table 1.1.

The spin dependent part of the Lagrangian can be written in terms of two additional structure functions, $g_1(x, Q^2)$ and $g_2(x, Q^2)$. We can see the spin dependent part of the cross section most easily by looking at the difference of cross sections for different spin orientations, thereby subtracting out the spin averaged part. We define $\sigma^{\uparrow\uparrow}$ and $\sigma^{\downarrow\uparrow}$ as the cross sections when the longitudinal spins of the target nuclei and the incoming electron are aligned and anti-aligned, respectively. Similarly, we define $\sigma^{\uparrow\rightarrow}$ and $\sigma^{\downarrow\rightarrow}$ to be the cross sections for the two electron helicity states on transversely polarized target nuclei. The cross sections then satisfy

$$\frac{d^2\sigma^{\downarrow\uparrow}}{d\Omega dE'} - \frac{d^2\sigma^{\uparrow\uparrow}}{d\Omega dE'} = \frac{4\alpha^2}{MQ^2} \frac{E'}{E_0} \left[\frac{1}{\nu} g_1(x, Q^2)(E_0 + E'\cos\theta) - \frac{Q^2}{\nu^2} g_2(x, Q^2) \right], \tag{1.3}$$

$$\frac{d^2\sigma^{\downarrow\rightarrow}}{d\Omega dE'} - \frac{d^2\sigma^{\uparrow\rightarrow}}{d\Omega dE'} = \frac{4\alpha^2}{MQ^2} \frac{E'^2}{E_0} \sin(\theta) \left[\frac{1}{\nu} g_1(x, Q^2) + \frac{2E_0}{\nu^2} g_2(x, Q^2) \right]. \tag{1.4}$$

Experimental measurements of these cross-section differences would allow the extraction of these spin-dependent structure functions g_1 and g_2. However, the cross-section differences are very small, and measurements of individual cross

sections would be limited by experimental systematic uncertainties. To reduce the

dependence on these systematic uncertainties, an asymmetry is measured,

$$A_\| = \frac{\sigma^{\downarrow\uparrow} - \sigma^{\uparrow\uparrow}}{\sigma^{\downarrow\uparrow} + \sigma^{\uparrow\uparrow}} \qquad A_\perp = \frac{\sigma^{\downarrow\rightarrow} - \sigma^{\uparrow\rightarrow}}{\sigma^{\downarrow\rightarrow} + \sigma^{\uparrow\rightarrow}}, \tag{1.5}$$

where σ is short for $d^2\sigma/(d\Omega dE')$. From Eqs. 1.3 and 1.4 we can relate the spin

structure functions to these measured asymmetries:

$$g_1(x, Q^2) = \frac{F_1(x, Q^2)}{D'} \left[A_\| + \tan\left(\frac{\theta}{2}\right) A_\perp \right], \tag{1.6}$$

$$g_2(x, Q^2) = \frac{y F_1(x, Q^2)}{2 D' \sin\theta} \left[\frac{E + E' \cos\theta}{E'} A_\perp - \sin\theta A_\| \right]. \tag{1.7}$$

Here we use the following additional definition:

$$D' = \frac{(1 - \epsilon)(2 - y)}{y(1 + \epsilon R(x, Q^2))}.$$

Notice also, that we use the known functions $F_1(x, Q^2)$ and $R(x, Q^2)$. $F_1(x, Q^2)$

is one of the unpolarized structure functions (see Eq. 1.2) and $R(x, Q^2)$ is the ra-

tio of longitudinal to transverse photon absorption cross sections (see Sec. 1.2). In

addition, it is possible to rewrite g_1 and g_2 in terms of the unpolarized structure

function F_1 and F_2 only, using the relation:

$$F_1(x, Q^2) = F_2(x, Q^2) \frac{1 + Q^2/\nu^2}{2x(1 + R(x, Q^2))}. \tag{1.8}$$

The unpolarized structure functions have been well measured to a few percent over a

large kinematic range, and R is typically small (≤ 0.2) with an uncertainty of ± 0.04

in our kinematic range so they have a small effect on our uncertainties. Parameterizations of the experimental data were used to calculate values for these functions at the current kinematics [1, 2].

It is interesting from an experimental perspective to examine the angular dependence of Eqs. 1.6 and 1.7. For small values of θ, the $g_1(x, Q^2)$ dependence on $A_\perp$ is reduced by $\tan(\theta/2)$ and is therefore dominated by $A_\parallel$. Similarly, $g_2(x, Q^2)$ is largely a function of $A_\perp$ at small angles.

1.2   Photon Absorption Cross Sections

Up to this point we have discussed using the DIS cross sections to extract the structure functions which completely describe the structure of the nucleon. However, there is also another notation, which remains from earlier experiments, that can be used to interpret this interaction. The process shown in Fig. 1.1 can be interpreted as having two separate processes, one at each vertex. The upper vertex involves the coupling between a lepton and a virtual photon and can be completely calculated using quantum electrodynamics (QED). The lower vertex involves the absorption of a virtual photon by the nucleon. Earlier experiments frequently described an interaction by the nucleon's absorption cross section relative to the properties of the virtual photon. It is instructive to examine these virtual photon absorption cross sections since there are still several theoretical predictions that can be examined with this data.

From the virtual Compton amplitudes, four independent absorption cross

sections can be extracted: $\sigma^T_{1/2}, \sigma^T_{3/2}, \sigma^L_{1/2}, \sigma^{TL}_{1/2}$. These refer to the absorption cross

sections for virtual photons with transverse (T) or longitudinal (L) polarizations

where the total angular momentum of the photon-nucleon system along the inci-

dent lepton direction is 1/2 or 3/2. σ^{TL} refers to the interference term between

longitudinal and transverse polarization amplitudes. We will also make use of the

averaged transverse absorption cross section σ^T and the ratio of longitudinal to

transverse absorption cross sections $R(x, Q^2)$:

$$\sigma^T(x, Q^2) = \frac{1}{2}\left[\sigma^T_{1/2}(x, Q^2) + \sigma^T_{3/2}(x, Q^2)\right], \tag{1.9}$$

$$R(x, Q^2) = \frac{\sigma^L_{1/2}(x, Q^2)}{\sigma^T(x, Q^2)}. \tag{1.10}$$

These absorption cross sections can be related to the previously defined kinematics

and structure functions:

$$\sigma^T_{1/2}(x, Q^2) = \frac{4\pi^2\alpha}{MK}\left[F_1(x, Q^2) + g_1(x, Q^2) - \frac{2Mx}{\nu}g_2(x, Q^2)\right], \tag{1.11}$$

$$\sigma^T_{3/2}(x, Q^2) = \frac{4\pi^2\alpha}{MK}\left[F_1(x, Q^2) - g_1(x, Q^2) + \frac{2Mx}{\nu}g_2(x, Q^2)\right], \tag{1.12}$$

$$\sigma^L_{1/2}(x, Q^2) = \frac{4\pi^2\alpha}{K}\left[\frac{F_2(x, Q^2)}{\nu}\left(1 + \frac{\nu^2}{Q^2}\right) - \frac{1}{M}F_1(x, Q^2)\right], \tag{1.13}$$

$$\sigma^{TL}_{1/2}(x, Q^2) = \frac{4\pi^2\alpha}{K}\frac{\sqrt{Q^2}}{M\nu}\left[g_1(x, Q^2) + g_2(x, Q^2)\right], \tag{1.14}$$

where $K = \nu - Q^2/2M$ is the incoming photon flux.

Using these absorption cross sections, we can then define two virtual photon-

nucleon asymmetries [3]:

$$A_1(x, Q^2) \equiv \frac{\sigma^T_{1/2}(x, Q^2) - \sigma^T_{3/2}(x, Q^2)}{\sigma^T_{1/2}(x, Q^2) + \sigma^T_{3/2}(x, Q^2)}, \tag{1.15}$$

$$A_2(x, Q^2) \equiv \frac{\sigma_{1/2}^{TL}(x, Q^2)}{\sigma^T(x, Q^2)}. \tag{1.16}$$

From the previous definitions, we can relate these virtual photon-nucleon asymmetries to the measured asymmetries $A_\parallel$ and $A_\perp$,

$$\begin{aligned}
A_1(x, Q^2) &= \frac{g_1(x, Q^2) - \gamma^2 g_2(x, Q^2)}{F_1(x, Q^2)} \\
&= \frac{A_\parallel}{D(1 + \zeta\eta)} - \frac{\eta A_\perp}{d(1 + \zeta\eta)},
\end{aligned} \tag{1.17}$$

$$\begin{aligned}
A_2(x, Q^2) &= \frac{\gamma(g_1(x, Q^2) + g_2(x, Q^2))}{F_1(x, Q^2)} \\
&= \frac{\zeta A_\parallel}{D(1 + \zeta\nu)} - \frac{A_\perp}{d(1 + \zeta\nu)},
\end{aligned} \tag{1.18}$$

with the following additional definitions:

$$\gamma^2 = \frac{Q^2}{\nu^2},$$
$$\eta = \frac{\epsilon\sqrt{Q^2}}{E_0 - \epsilon E'},$$
$$\zeta = \eta\frac{1 + \epsilon}{2\epsilon}.$$

$$D = \frac{1 - \frac{E'\epsilon}{E_0}}{1 + \epsilon R(x, Q^2)},$$
$$d = D\sqrt{\frac{2\epsilon}{1 + \epsilon}},$$

1.3 Theoretical Motivation

In the previous sections, the definitions of the structure functions $g_1(x, Q^2)$ and $g_2(x, Q^2)$ were developed, as well as the two virtual photon-nucleon asymmetries $A_1(x, Q^2)$ and $A_2(x, Q^2)$. These functions have kinematic dependencies which, under the E154 conditions, allow us to recognize that $g_1(x, Q^2)$ and $A_1(x, Q^2)$ are dominated by the experimental asymmetry $A_\parallel$. Similarly, $g_2(x, Q^2)$ and $A_2(x, Q^2)$

are dominated by the experimental asymmetry $A_\perp$.

Most of the history of spin structure measurements have focused on measurements of $A_\parallel$, giving results for g_1 and A_1. This thesis will focus on the transverse results ($A_\perp$) from E154. The following sections are presented to introduce the theoretical concepts involved in interpreting the perpendicular data with respect to g_2 or A_2. A more thorough and complete survey of the theoretical framework underlying the spin structure of the nucleon is provided by Anselmino, Efremov, and Leader [4].

1.3.1   Quark Parton Model

In the naive Quark Parton Model (nQPM), the nucleon is considered to be made of collinear, free quarks. These quarks do not interact with each other and each carry a fraction x' of the nucleon's four-momentum. DIS reactions can then be described in the nQPM as the incoherent sum over all possible lepton-quark interactions between the incoming lepton and the constituent quarks [4].

The g_2 structure function is directly dependent on the transverse momentum distribution of the constituent quarks. Since the nQPM assumes no transverse momentum for the constituent quarks, the prediction for g_2 is trivial:

$$g_2(x) = 0. \tag{1.19}$$

A non-zero value for g_2 can be obtained by allowing the quarks to have an intrinsic Fermi motion inside the nucleon. A transverse momentum distribution from this can then allow transverse spin dependent terms to arise. Anselmino, Efremov,

and Leader [4] calculated g_2 under these assumptions. Boosted to a fast frame where the spins of the quarks can be considered collinear with the spin of the nucleon, they get the following expression:

$$g_2(x) = \frac{1}{2} \sum_q e_q^2 \left(\frac{m_q}{xM} - 1 \right) \Delta q(x), \tag{1.20}$$

where $\Delta q(x)$ is the difference between the number density of quarks with the same helicity as the nucleon and those with opposite helicity and the sum is over all quark flavors. Notice that this is heavily dependent on quark mass effects. In fact, if the quark masses are allowed to be different from the bare quark masses, representing the fact that these are actually bound quarks, this result ceases to be gauge invariant. However, if we assume m_q to be the constituent quark mass, then $m_q = xM$, and we return to the previous result in Eq. 1.19. This delicate sensitivity to quark mass effects makes it very difficult to trust any purely parton model calculations for g_2, and experimental results are difficult to interpret under this framework.

1.3.2   Bag Models

Bag models describe the nucleon by a region of space or "bag" which is capable of containing quark and gluon fields. The partons are confined to the bag by a universal pressure, B, but are only weakly coupled to one another inside [5]. Thus the nucleon is defined more by the boundary conditions of the bag rather than the quark-gluon or gluon-gluon interactions. Many bag models exist which differ by their definition of the boundary conditions, the number and type of fields contained in the bag, or the calculation scheme used to extract observational results.

Recent theoretical work has extended the scope of bag models to provide calculations of deep-inelastic structure functions which are consistent with experimental data. Most of these use the MIT bag model [5] or a modification of it. In the MIT bag model, the bag is assumed to have a constant fixed radius, and all explicit gluonic degrees of freedom are neglected.

The transverse spin structure function g_2, has been calculated using the original MIT bag model by Jaffe and Ji [6], and other modified versions of the MIT bag model by Schreiber et al. (SST bag model [7]) and by Stratmann (MOD model [8]). For this work, the calculations by Stratmann are used (shown in Fig. 1.2) as a representative of these calculations based on the MIT bag model.

In addition to the calculations discussed above, the so called center-of-mass (CM) bag model [9] was used by Song [10] to provide calculations for the spin structure functions. Unlike the MIT bag model in which the bag is static and hence the center of mass is at rest, the CM bag model re-defines the parameters of the bag in terms of it's center of mass. It is argued [9] that the center of mass degree of freedom is important when considering deep inelastic scattering in which the recoil of the nucleon can be significant. The calculations of g_2^n using the CM bag model [10] are compared in Fig. 1.2 to the MIT bag model based calculations of Stratmann and to the QCD based calculation of Wandzura and Wilczek [19] (see Sec. 1.3.4). It is interesting to note that the structures of the two predictions are quite different.
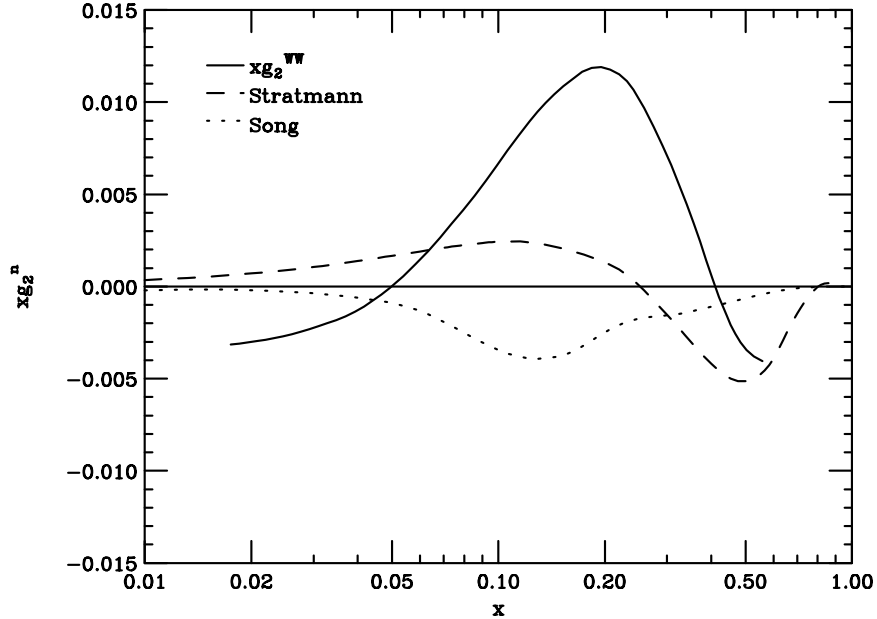
Figure 1.2: Bag model predictions for xg_2^n. Shown are the calculated predictions for xg_2^n using bag models by Stratmann [8] (dashed) and Song [10] (dotted). In addition, these predictions are compared with the QCD based relation from Wandzura and Wilczek [19] (solid) as described in Eq. 1.25 and calculated from a fit to experimental data for g_1^n.

1.3.3   Operator Product Expansion

The Operator Product Expansion (OPE) is a technique first introduced by Wilson [11]. In general, the OPE concerns the quantum field theory operators that describe an interaction over a short distance. These operators, or products of operators, are not always calculable. Wilson developed a method for expressing the product of such operators as an infinite sum over simpler local operators as long as the distance scale was sufficiently small:

$$\mathcal{A}(x)\mathcal{B}(y) = \sum_n C_n(x-y)\mathcal{O}_n(x). \tag{1.21}$$

Here, $\mathcal{A}(x)$ and $\mathcal{B}(y)$ are the original operators at locations x and y, respectively. The $\mathcal{O}_n(x)$ are the local operators and the $C_n(x-y)$ are the coefficients. This expansion is motivated by the fact that the $\mathcal{O}_n$ are easily calculable, and for many

physics processes, only a finite number of terms contribute.

In the case of spin-dependent DIS, it turns out that the OPE can be organized by a combination of the dimensionality and spin of the operators. This combination is referred to as twist [12] where the lowest order term is twist-2. When organized in this fashion, the expansion can be related to a power series in the previously defined variable $1/\sqrt{Q^2}$. For the Q^2 of this experiment $(1.0 < Q^2 < 17.0)$, only the first few terms of the power series (lowest orders of twist) are expected to contribute.

As mentioned previously, the real benefit of the OPE is that these terms can be calculated exactly. Normally these terms are manipulated in the form of a matrix whose elements are related to the individual components of the expansion. The lowest order matrix elements have been related to the moments of the experimentally measurable spin structure functions,

$$\int_0^1 x^n g_1(x, Q^2) dx = \frac{a_n}{2}, \quad \text{n=0,2,4,...} \tag{1.22}$$

$$\int_0^1 x^n g_2(x, Q^2) dx = \frac{1}{2}\frac{n}{n+1}(d_n - a_n), \quad \text{n=2,4,...} \tag{1.23}$$

where the a_n and d_n refer to the twist-2 and twist-3 matrix elements, respectively. Notice that with measurements of g_1, a direct extraction of the twist-2 matrix elements are possible. However, with the addition of a g_2 measurement, we can directly extract the twist-3 matrix elements:

$$d_n = 2\int_0^1 x^n \left[g_1(x, Q^2) + \frac{n+1}{n}g_2(x, Q^2)\right] dx, \quad \text{n=2,4,...} \tag{1.24}$$

This allows for one of the first direct measurements of twist-3, which can also be exactly calculated under QCD and OPE. Twist-2, being the lowest order

interaction, can be related to the quark distribution functions, while twist-3 is really looking at the interference from quark-gluon interactions.

Lattice QCD and QCD Sum Rule Calculations for d_2

There are two methods that are usually used to provide calculations of the OPE matrix elements, Lattice QCD and QCD sum rules. Both of these methods use the fundamental operators from quantum field theory to provide the basis for the calculations.

The current methodology for QCD sum rules was developed by Shifman et al. [13]. The QCD sum rules make use of the general dispersion relations which give the polarization operators in terms of the observable cross sections. Then, those same operators can be expanded using the OPE as described above. Equating the two expressions of the same operator results in a QCD sum rule which is expressed on one side by observable cross sections and on the other side by an infinite power series in $1/Q^2$. It should be noted that the form of such sum rules is not unique. The QCD operators can be expressed in terms of different field currents and various methods can be used to evaluate the infinte power series. Two such QCD sum rule calculations were made of the d_2 matrix element. The first [14] starts from the basic three quark current operator introduced by Ioffe [15]. They arrived at a surprising difference between the proton and neutron results for d_2 and, in addition, the proton results had an opposite sign to that suggested by bag model predictions. As a result, a second QCD sum rule calculation was performed by Stein et al. [16]

using a different operator expression in which, in addition to the three quark fields, the gluon field is included explicitly. The results from this second QCD sum rule calculation are in relative agreement with the previous QCD sum rule result. These results are compared to the experimental data in addition to the bag model and lattice QCD results in Table 5.3.

Lattice QCD offers another method of dealing with the intractability of the small scale properties of the QCD operators over the large distance scales of a nucleon. Rather than using the OPE to expand the operator into a sum of local operators, lattice QCD performs numerical calculations of the fundamental QCD operators at discrete points [17]. By numerically integrating a lattice of these points that spans the entire space and time of the nucleon interaction, a physical process can be calculated. As might be suspected, this process can be very computationally cumbersome. The precision of the results is largely a function of the lattice spacing (the distance between individual points in the lattice). As a result, lattice QCD calculations of d_2 are still in their preliminary stages. As of this paper, only one such calculation exists [18]. This work used a lattice of $131,072$ points (16^3 space points $\times 32$ time points) to span the nucleon. The calculation was performed for Wilson fermions in the quenched approximation, where internal quark loops are neglected. In addition, gluonic operators were also neglected. The results from this lattice calculation are compared with the other previously mentioned results in Table 5.3. It should also be mentioned that the lattice calculation is merely a tool with which to calculate a particular set of operators. Different lattice formulations

of the same field theory can be calculated, as with the QCD sum rules mentioned above.

1.3.4   Additional QCD Analysis

The Wandzura-Wilczek Relation

In a complete description of g_2, all terms, twist-2 and above, must be understood. There have been several analyses which look at different parts of g_2 and its higher twist dependence. One of the commonly cited results is from an analysis by Wandzura and Wilczek [19]. Their work used certain model assumptions to predict that all higher twist terms beyond twist-2 could be neglected. They were then able to construct a relationship between g_2 and g_1:

$$g_2^{WW}(x, Q^2) = -g_1(x, Q^2) + \int_x^1 \frac{g_1(y, Q^2)}{y} dy. \qquad (1.25)$$

It is perhaps useful to realize that this relation can also be derived from the OPE relations above (Eqs. 1.22 and 1.23) with the assumption that all twist-3 elements are zero ($d_n = 0$ for all n).

More recent analyses (cf. [4]) have pointed out that the models used by Wandzura and Wilczek are not very reliable, giving nonsensical results for the other structure functions $F_{1,2}(x)$ and $g_1(x)$. As a result, their neglect of the twist-3 terms is probably dangerous. However, the Wandzura-Wilczek relation is still a useful prediction of the twist-2 part of $g_2(x)$ and is used quite frequently to look for deviations in the experimental data which might suggest higher twist effects.

The Burkhardt-Cottingham Sum Rule

If we return to Eq. 1.23, we notice that the moments of g_2 are defined only for $n = 2$ and greater. The first moment of g_2 ($n = 0$) has no definition in the OPE. An analysis by Burkhardt and Cottingham [20] makes a prediction for this moment:

$$\int_0^1 g_2(x, Q^2)dx = 0. \tag{1.26}$$

They derived this relation by considering the asymptotic behavior of a certain virtual Compton amplitude that is proportional to g_2. This prediction rests largely on the assumption that this asymptotic behavior is governed by Regge poles. However, a later analysis by Heimann [21] shows that there should also be contributions from multi-pomeron and pomeron-Regge cuts that would invalidate the original assumptions. These couplings are very sensitive and could even imply that $g_2(x)$ would have a very singular behavior at low-x:

$$g_2(x) \overset{x \to 0}{\propto} \frac{1}{x^2}. \tag{1.27}$$

Thus, the integral in Eq. 1.26 might not even converge. Experimentally, it will be very difficult to test the validity of these calculations since it is difficult to measure down to low enough values of x to see this behavior. Also, the singular behavior might be very Q^2 dependent and it is not clear at what values one might expect to see it.

A Complete Description of g_2

More recent analyses have been performed using an advanced light-cone parton model [22, 23], as well as a more complete OPE analysis [6]. These calculations have been shown to be complete up to and including twist-3. For now, the higher order twist terms are expected to have a small contribution due to the high Q^2 of the current experimental measurements. These analyses suggest that there are three components contributing to g_2: the leading twist-2 part $(g_2^{WW}(x, Q^2))$ described by the Wandzura-Wilczek relation (Eq. 1.25), another twist-2 part coming from the quark transverse polarization distribution $h_T(x, Q^2)$, and a twist-3 part coming from quark-gluon correlations $\xi(x, Q^2)$:

$$g_2(x, Q^2) = g_2^{WW}(x, Q^2) - \int_x^1 \frac{\partial}{\partial y}\left(\frac{m_q}{M}h_T(y, Q^2) + \xi(y, Q^2)\right)\frac{dy}{y}. \qquad (1.28)$$

Here, m_q refers to the quark mass and M refers to the mass scale (either the mass of the nucleon or λ_{QCD}).

This separation is quite useful from an experimental point of view, since the leading twist-2 term can be calculated from known measurements of $g_1(x, Q^2)$. As a result, any measurement of $g_2(x, Q^2)$ can look for additional effects by the extraction of $\overline{g_2}(x, Q^2)$:

$$\overline{g_2}(x, Q^2) \equiv g_2(x, Q^2) - g_2^{WW}(x, Q^2). \qquad (1.29)$$

Very little is known about the twist-2 transverse quark polarization distribution h_T, but it is suggested that the multiplicative m_q/M term may reduce its effect, thus allowing it to be neglected. If that is true, then a non-zero measurement of

$\overline{g_2}(x, Q^2)$ would be the first direct measurement of higher twist effects as a function

of x and Q^2.

1.3.5 A_2 Positivity Limit

In addition to the g_2 predictions discussed above, there is a positivity con-

straint on A_2 (defined in Eq. 1.16) which can also be tested by experimental mea-

surement.

The definition of A_2 involved the virtual photon absorption cross sections

$\sigma^{TL}_{1/2}$ and σ^T. In the case of virtual forward Compton scattering, these cross sections

can be related to the case in which an incoming transversely polarized photon flips

its spin and becomes a longitudinally polarized outgoing photon ($\sigma^{TL}_{1/2}$) or the case in

which the incoming and outgoing photon are both transversely polarized (σ^T). We

can then write these cross sections, and A_2, in terms of longitudinal and transverse

amplitudes ($|A_L\rangle$ and $|A_T\rangle$):

$$A_2 \equiv \frac{\sigma^{TL}_{1/2}}{\sigma^T} = \frac{|\langle A_L | A_T \rangle|^2}{|\langle A_T | A_T \rangle|^2} \; e^{i\phi}, \qquad (1.30)$$

where the $e^{i\phi}$ represents the phase difference between the cross sections. Using the

Schwartz inequality relation, we can put an upper bound on the magnitude of A_2

$$|A_2| \leq \frac{|\langle A_L | A_L \rangle| \cdot |\langle A_T | A_T \rangle|}{|\langle A_T | A_T \rangle|^2} = \frac{|\langle A_L | A_L \rangle|}{|\langle A_T | A_T \rangle|}. \qquad (1.31)$$

The right side of Eq. 1.31 can be recognized as the square root of the quantity

$R(x, Q^2)$ (defined in Eq. 1.10). Since $R(x, Q^2)$ has been measured at many different

kinematics, a measurement of $A_2(x, Q^2)$ allows a very simple experimental test of

the positivity constraint

$$\left| A_2(x, Q^2) \right| \leq \sqrt{R(x, Q^2)}. \qquad (1.32)$$

CHAPTER 2

EXPERIMENTAL DESIGN

The E154 experiment was designed to provided high precision data for the measurement of $g_1(x, Q^2)$ on the neutron. The experiment was performed at the Stanford Linear Accelerator Center (SLAC) using polarized electrons on a polarized ^{3}He target. Typically electron polarizations of 82% and ^{3}He polarizations of 30-50% were achieved. With a beam energy of 50 GeV, this produced a measurement of $g_1^n(x, Q^2)$ in the kinematic range $0.014 \leq x \leq 0.7$ and $1.0 \text{ GeV}^2 \leq Q^2 \leq 17 \text{ GeV}^2$.

2.1 Apparatus

2.1.1 The Beam

The linear accelerator (linac) at SLAC was used to provide a high energy, long pulse beam for E154. Recent upgrades in the A-line transport allowed the full 50 GeV beam produced in the linac to be used in End Station A (ESA). A special klystron tuning setup was developed for E154 that allowed the accelerator to deliver pulses of $\sim 3 \times 10^{10}$ electrons with a pulse length of 250 ns and an energy spread of less than 1%. The pulses were delivered at a rate of 120 Hz.

The beam conditions were monitored and recorded pulse by pulse in ESA. The beam energy was monitored, as in previous end station experiments, by the

use of a flip coil mounted in an identical magnet set in series with the A-line bend string. With the upgraded high energy transport line [24], this flip coil measurement had to be re-calibrated. This was accomplished by using the Møller polarimeter measurements (see Sec. 2.1.4) over a range of energy from 46 - 49 GeV. Since the beam is polarized and the A-line goes through a known 24.5° bend, the polarization will go through a predictable number of precessions. The Møller measurements were sensitive enough to fit the precession data (see Fig. 2.1) and allow a calibration of the flip coil [25].
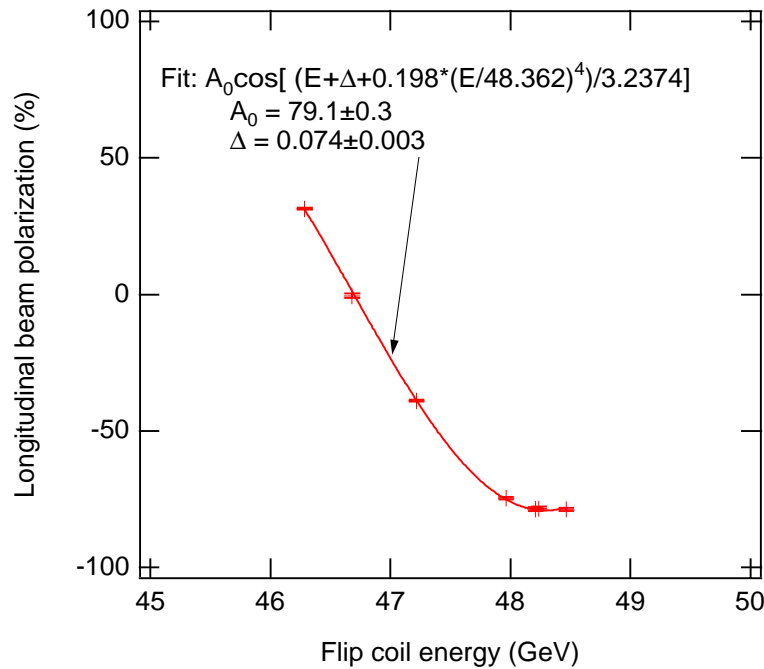
Figure 2.1: Results of the Møller energy scan measurement. The Møller beam polarization data were plotted with respect to the beam energy as calculated from a nominal calibration of the flip coil magnet. These data were fitted to the expected energy dependence shown, with the polarization magnitude A_0 and an energy offset Δ as fit parameters. The shown values were used for the final calibration of the flip coil magnet.

The beam current was monitored with two toroids located at the entrance to the end station. The beam position was monitored with several beam position

monitors in the transport line to aid the operations staff and automatic feedback systems in establishing a stable beam into the end station. To insure proper beam position and angle at the target, a traveling wave monitor was used directly up stream of the target and horizontal and vertical wire arrays were placed a few meters downstream of the target. In addition, two so-called "spill monitors" were used to look for rapid changes in beam conditions. Each spill monitor consisted of a scintillating paddle placed about half a meter from the beamline, connected to a photo-multiplier tube. The signal was monitored in real-time on an oscilloscope, and the integrated signal for each pulse was recorded to tape. The "bad spill" monitor was located upstream of the target, right at the entrance to the end station. Particles detected in the "bad spill" monitor indicated beam loss upstream in the transport line that might suggest poor beam conditions at the target. The "good spill" monitor was located a few meters from the target. Scattering rate from the target could therefore be monitored to see if the beam was missing the target (little or no signal) or if it was hitting some thicker part of the target apparatus (abnormally large signal).

2.1.2   The Target

This experiment was made possible by the development of polarized gaseous ^{3}He targets. The E154 target configuration was originally used in E142. Improvements were made for E154 that allow higher polarization of the ^{3}He and lower dilution from the glass end windows. The target design and performance are cov-

ered in great detail in Refs. [26, 27, 28, 29]. A simple overview will be presented here.

Using ^{3}He to Study the Neutron

In the past, neutron structure functions have been extracted by using targets rich in hydrogen and deuterium. Then making the naive assumption that deuterium is a proton plus a neutron, the neutron's structure can be inferred by subtracting the proton structure function from that of the deuteron. However, the difficulty of extracting a neutron signal from the rather large proton effects make this method less than ideal for the accurate measurement of spin structure functions.

The ^{3}He target is intended to supply a more direct measurement of the neutron's spin properties. The naive model of the ^{3}He nucleus is shown in Fig. 2.2. In the dominant S-state wave-function, the spins of the 2 protons are anti-aligned. Thus any spin-dependent effects from one proton would be canceled by the other proton. Any measured spin-dependent effects from the ^{3}He nucleus would then correspond to effects from the neutron only.

In reality, the ^{3}He nucleus is more complicated than this naive approach. The ground state wave-function contains contributions from the S$'$ and D-state wave-functions in which the polarizations of the two protons are aligned and the neutron polarization is anti-aligned with that of the ^{3}He nucleus. Plane Wave Impulse Approximation (PWIA) calculations have been performed [30] indicating that the measured spin structure function from ^{3}He can be adequately represented as a
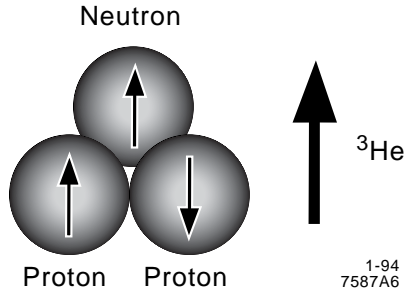
Figure 2.2: S-state configuration of the ^{3}He nucleus. A polarized ^{3}He nucleus is dominated by the S-state wave-function in which the individual nucleons are aligned as shown. Notice that with the two proton spins anti-aligned, any spin dependent contribution from this wave-function is strictly the result of the neutron polarization.

combination of proton and neutron spin structure functions weighted by appropriate polarization coefficients, given by

$$g_1^{^3\text{He}} = 2P_p g_1^p + P_n g_1^n \tag{2.1}$$

where the polarization coefficients were calculated to be $P_p = -0.027 \pm 0.004$ and $P_n = 0.87 \pm 0.02$.

Currently, there is additional activity in the field [31]; some theorists are predicting that the extraction of the neutron spin structure function from a ^{3}He nucleus is more complicated [32]. These predictions, while interesting and well worth attention in the future, are not applied to this work.

Target Construction

The E154 target consists of two glass chambers (see Fig. 2.3). The upper chamber (pumping cell) with a volume of 70-80 cm^3 is filled with ^{3}He and a small amount of Rb metal. It is held inside a plastic oven which maintains a temperature of 170-200° C necessary to create a Rb vapor density of $\sim 10^{14}$ atoms/cm^3. The
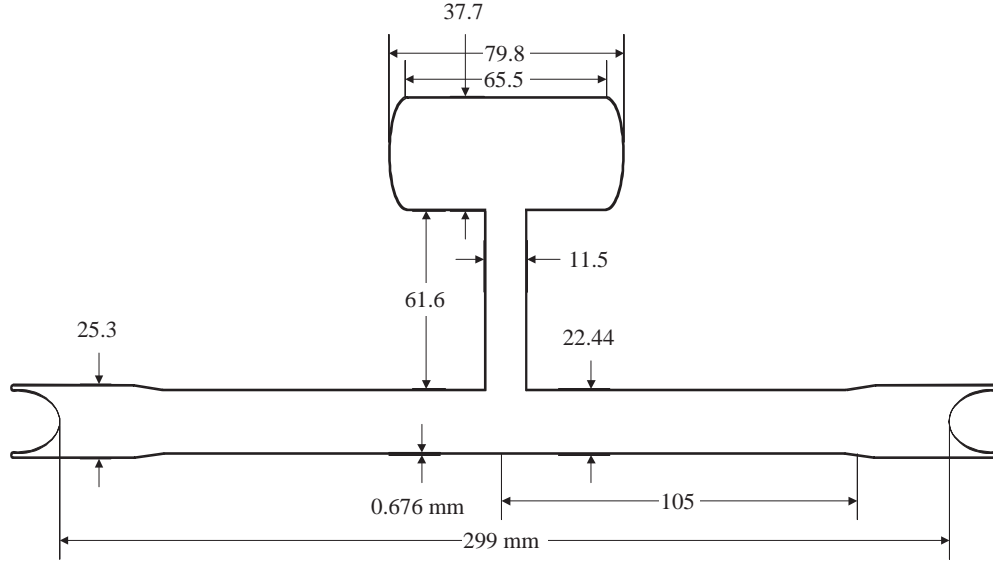
Figure 2.3: Dimensions (mm) of the E154 target cell "Picard".

pumping cell was continuously illuminated with ∼80 Watts of circularly polarized laser light to maintain the Rb polarization. The laser light was produced by three 20-Watt diode lasers and four Argon-Ion pumped Ti:Sapphire lasers [28].

The lower chamber (target cell) was connected to the pumping cell by a 6 cm long transfer tube. The ^{3}He atoms in the pumping cell could diffuse through the transfer tube down to the target cell, while the temperature gradient between the heated pumping cell ($\sim 180°C$) and the unheated target cell ($\sim 65°C$) was enough to restrict the Rb vapor to the upper cell only. The target cell was a 30 cm long cylinder with a radius of ~ 2.5 cm. The end-caps, which were concave hemispheres with a thickness of $\sim 50\mu$m, were specially designed to reduce the amount of glass that could interact with the beam. This cell was centered on the beam line with

cooling jets of ^{4}He directed on the end-caps to reduce the effects of beam heating. A complete schematic of the target apparatus is shown in Fig. 2.4.

Polarization of the Targets

In order to extract the spin properties of the neutron, we first have to achieve a polarized ^{3}He nucleus. The method used for this target was spin exchange through collision with optically pumped Rubidium vapor. As described above, the Rb vapor was maintained in the pumping cell at a temperature sufficient to create a vapor density of $\sim 10^{14}$ atoms/cm^3. Circularly polarized laser light at 794.7 nm forces the electrons of the Rb atoms to make a D1 $(5S_{\frac{1}{2}} - 5P_{\frac{1}{2}})$ transition. Collisions between the atomic electrons of the Rb and the ^{3}He nucleus causes spin exchange through a hyperfine interaction.

The polarization was maintained by two Helmholtz coils that could provide a uniform magnetic field with magnitude between 8 - 19 Gauss. The main source of depolarization came from ^{3}He - ^{3}He and ^{3}He - glass collisions. Well constructed cells usually had a relaxation time constant of 40 - 70 hours for depolarization [28, 29]. With 80 Watts of laser power, a steady state ^{3}He polarization of 30 - 50% could be achieved. This polarization was measured through a NMR-AFP technique with a water signal calibration [28]. The AFP (Adiabatic Fast Passage) measurements were checked with an alternative EPR (Electron Paramagnetic Resonance) measurement [29]. The two methods agreed to within 5%. The NMR polarization measurements for the entire run are shown in Fig. 2.5.

E-154 Target Schematic
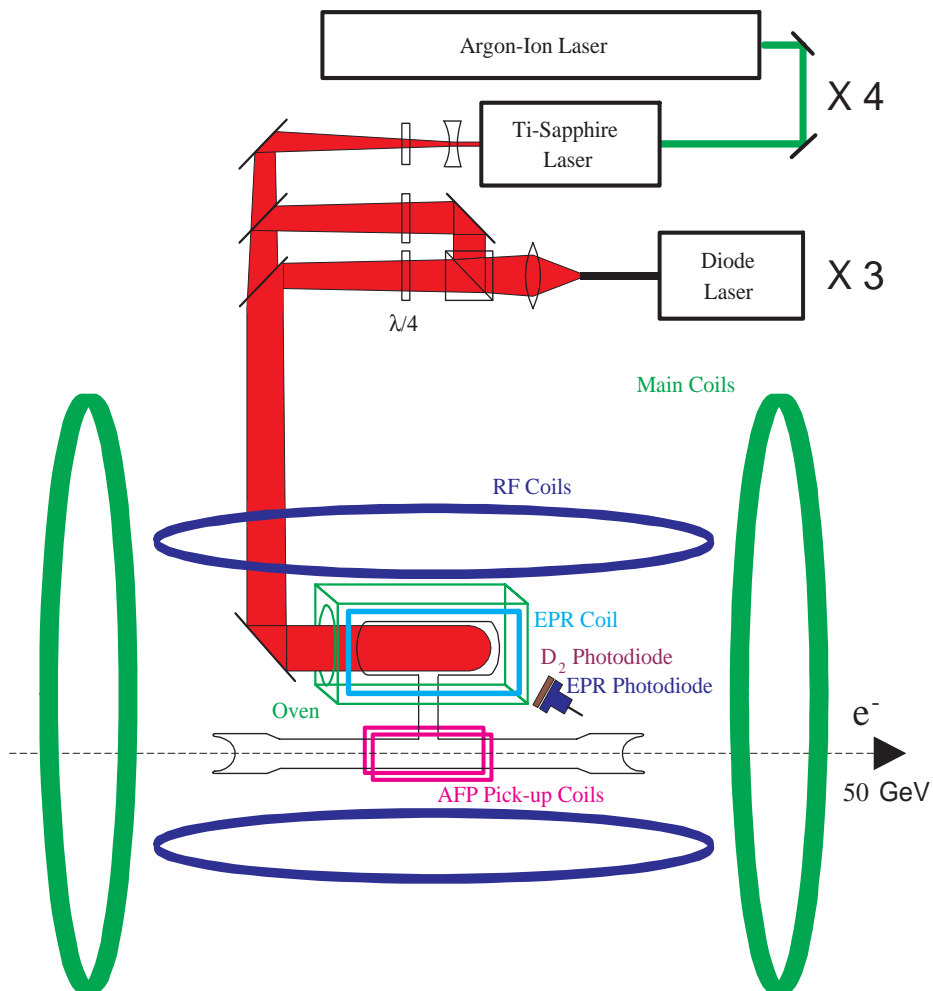
Figure 2.4: Schematic of the E154 polarized target apparatus. The position of the ^{3}He target cell is shown relative to the beamline. Notice that the upper cell of the target is maintained in the oven where the polarized light from the lasers are used to maintain the polarization. The unlabeled outer coils are the Helmholtz coils used to maintain a magnetic orientation for the polarized ^{3}He nuclei.

E154 He^3 Polarization History
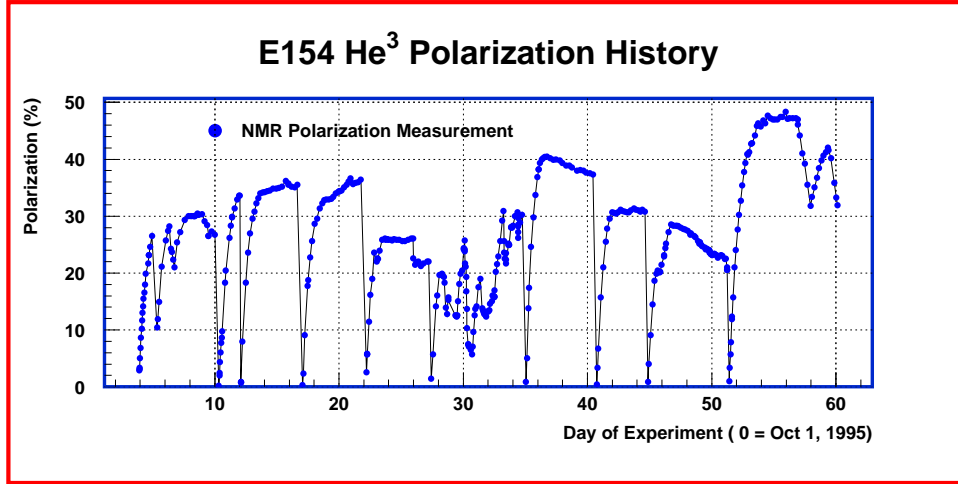
Figure 2.5: Results of ^{3}He polarization measurements during E154. The data shown are the result of NMR measurements made during the experiment. The frequent 0% measurements followed by a rapid rise in polarization correspond to the installation and polarization of a new target. A total of nine targets were used in E154.

2.1.3 The Spectrometers

The spectrometers for E154 were set up to optimize the kinematic coverage for the 50 GeV electron beam, while minimizing the backgrounds from other sources. Two single-arm spectrometers were used at central scattering angles of 2.75° and 5.5°. Both spectrometers used a so-called "S-bend" configuration of two bending magnets with opposite polarity. This configuration, combined with appropriate collimation, restricts the ability of neutral or off-energy particles to enter the detector system. The only way they can enter the spectrometer is by going through two separate bounces (scattering processes) off of the magnets or collimators. The 2.75° spectrometer also included a quadrupole magnet to defocus the horizontal distribution of particles, making the data rate more uniform across the detectors.

Inside of each spectrometer, the detector packages were comprised of similar components. Two gas Cerenkov counters were used for particle identification. Two

sets of finely segmented hodoscopes were used to provide position and angle measurement. Each spectrometer had an identical shower counter made of 200 lead-glass blocks arranged in a 10 X 20 array to provide total electron energy information, as well as additional particle identification and position information. A schematic of the spectrometer setup is provided in Fig. 2.6.
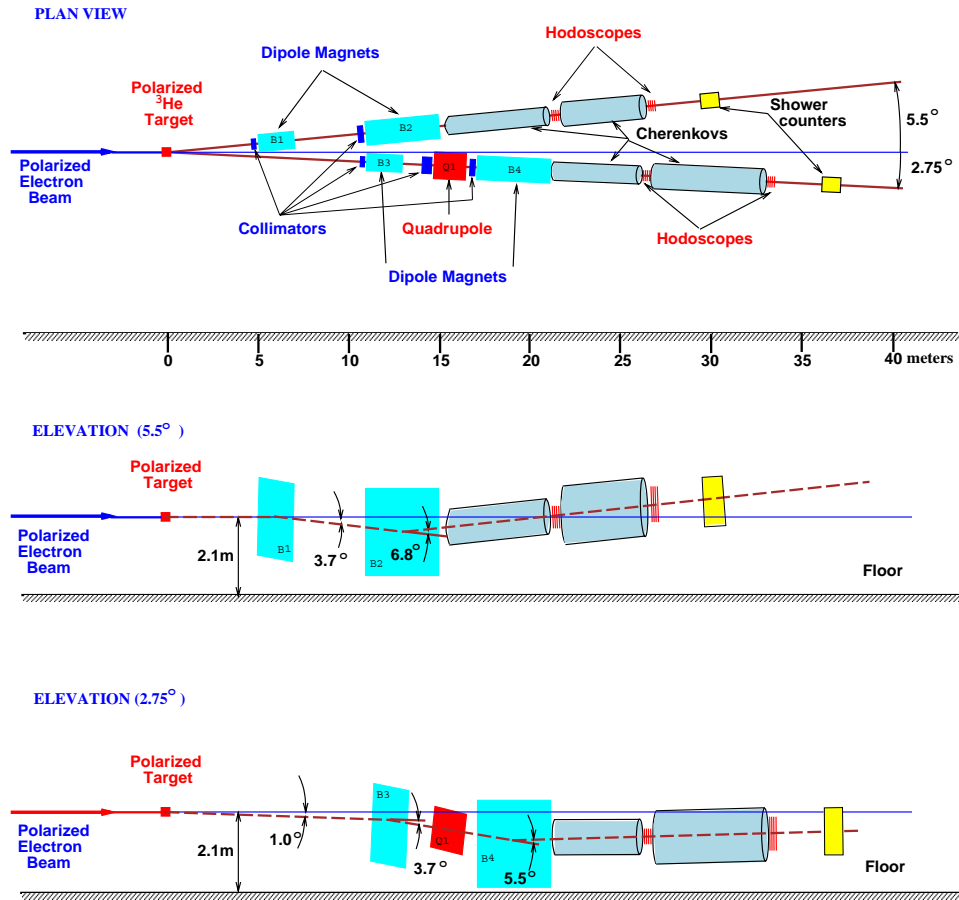
Figure 2.6: A schematic of the E154 spectrometer layout. The upper "plan view" shows the layout of the two spectrometers at their respective scattering angles relative to the beamline. In addition, the lower two "elevation" schematics show the placement of the detectors and the central trajectory of the electrons through the "S-bend" magnet configuration for each spectrometer.

<u>Cerenkov Counters</u>

Experimentally discovered by P.A. Cerenkov in 1934, and later explained by I.M. Frank and I.E. Tamm, Cerenkov radiation has become a ubiquitous tool for high-energy physics detectors. Cerenkov radiation is the result of a charged particle traveling through a medium with a velocity (v) faster than the phase velocity of light in that material,

$$v > \frac{c}{n} \tag{2.2}$$

where, n is the index of refraction for the medium and c is the speed of light in a vacuum.

For a given material, Eq. 2.2 indicates that there will be a threshold velocity below which Cerenkov radiation will not occur. This threshold velocity translates to a momentum threshold which is dependent on the mass of the particular particle. This is the basis of the so called threshold Cerenkov counter used in E154.

Pions were the primary background in the spectrometers for E154. Two Cerenkov tanks were used in each spectrometer to discriminate electrons from the heaver pions. The tanks were filled with nitrogen (N_2) at sub-atmospheric pressure to create a velocity threshold that would be below the velocity of all electrons entering the spectrometer, but above that of most of the heavier pions. The dimensions and pion thresholds of each tank are shown in Table 2.1.

Each Cerenkov detector consisted of an aluminum cylinder with thin aluminum end windows. At the downstream end a spherical mirror was located such

Tank	Length (m)	Press. (psia.)	Pion Threshold (GeV)
2C1	5.6	1.4	19
2C2	6.5	1.4	19
5C1	5.8	2.0	16
5C2	4.3	2.0	16

Table 2.1: Parameters of the E154 Cerenkov counters. Tanks 2C1 and 2C2 were located in the 2.75° spectrometer while 5C1 and 5C2 were located in the 5.5° spectrometer. The tanks were filled with sub-atmospheric nitrogen (N_2) at the pressures listed to create the listed momentum threshold for pions.

that it would focus the Cerenkov radiation onto a photo-multiplier tube mounted on the side of the tank. The anode signal from each photo-tube was digitized in a Struck DL515 FADC (Fast Analog to Digital Converter) module. By interleaving 4 channels of the FADC's, a timing resolution of 1 ns was achieved. This allowed clear pulse separation with a dead time of less than 5 ns, even at the high instantaneous rates of E154. This can be seen in Fig. 2.7(a) where a typical Cerenkov signal is shown. Also shown is the distribution of the number of Cerenkov signals recorded per spill. With a peak at about 2 or 3, it is easy to recognize that the pulse separation is more than sufficient. The Cerenkov efficiency for the detection of electrons was found to be $\sim 95\%$ for each detector using a cut of >25 FADC counts as described in Sec. 3.1.4.

Scintillating Hodoscopes

High energy particles passing through a scintillating material excite the atoms in that material. In returning to their ground state, these atoms emit photons of
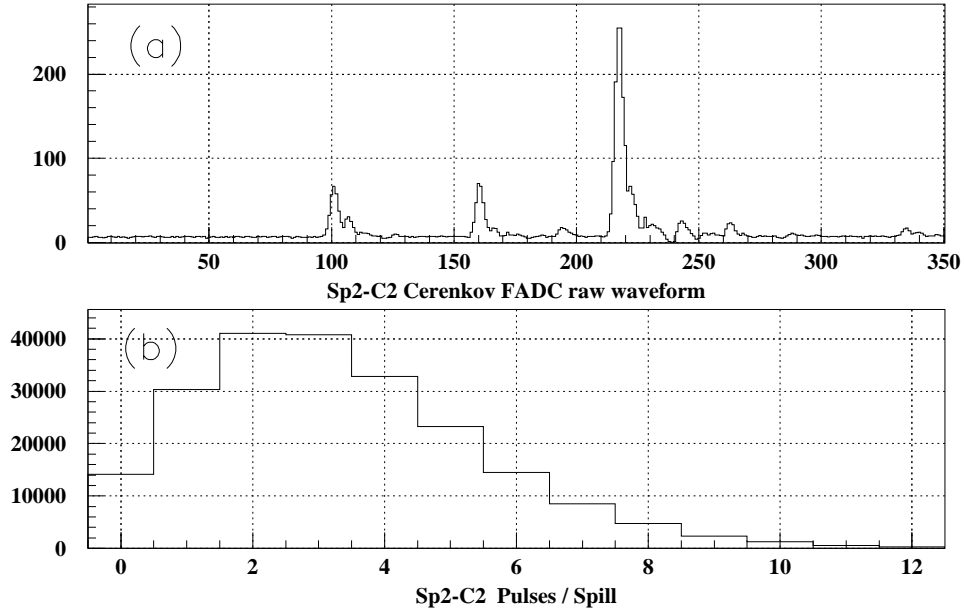
Figure 2.7: Typical Cerenkov output signals. (a) shows a typical raw Cerenkov signal (nsec) taken from the data. (b) shows the distribution of the number of Cerenkov signals recorded per beam spill.

light. Long, thin fingers of the scintillating material Bicron BC404 were used in the hodoscopes for E154. The material is transparent, allowing the light to pass down the length of the finger. Each finger was wrapped first with an aluminized material and then with black tape to reduce the probability of light escaping or being contaminated from external sources. Hamamatsu R4014 photo-multiplier tubes attached to each finger were used to collect these emitted photons.

Multiple parallel fingers were assembled into each plane of hodoscopes. Many of the fingers were placed with an overlap of approximately one-third of their width to improve position resolution. Each group of hodoscopes was made of at least 4 planes. Individual planes were grouped in pairs oriented at angles relative to each other. For example, a Y plane would be oriented with the fingers all horizontal

to provide position information in the vertical direction. This would be paired with an X plane, with all the fingers oriented at 90° (vertically) to provide position information in the horizontal direction. Some planes were also oriented at angles of ±15° and ±45°. Since some of these planes were reused from the previous E142/E143 experiments and others were newly constructed for E154, the dimensions and setup of each plane were not consistent. The individual characteristics of each plane are listed in Table 2.2.

Name	Angle (°)	Channels	Finger Width (mm)	Finger Overlap (mm)	Location
2H1U	+15	44	15	5	2.75° front
2H2V	-15	44	15	5	2.75° front
2H3X	90	64	13	1	2.75° front
2H4Y	0	72	13	1	2.75° front
2H5Y	0	31	30	10	2.75° front
2H6X	90	34	20	7	2.75° front
2H7X	90	90	13	1	2.75° back
2H8Y	0	90	13	1	2.75° back
2H9Y	0	55	30	10	2.75° back
2H10X	90	27	30	10	2.75° back
5H1U	-45	25	45	15	5.5° front
5H2X	90	23	30	10	5.5° front
5H3Y	0	36	30	10	5.5° front
5H4V	+45	25	45	15	5.5° front
5H5U	-45	21	75	25	5.5° back
5H6X	90	27	30	10	5.5° back
5H7Y	0	55	30	10	5.5° back
5H8V	+45	21	75	25	5.5° back

Table 2.2: Hodoscope parameters for each plane in E154. For each hodoscope plane, the size, number, and overlap of the fingers in the plane are listed. Also their angle relative to the horizontal is shown. In addition, the planes are grouped by their position in the spectrometers.

The signals from the photo-tubes were sent through a discriminator and a

multi-hit TDC (Time to Digital Converter) to record the time of each hit. The 5.5° hodoscopes used LeCroy 4413 discriminators and LeCroy 2277 TDC's. In the 2.75° spectrometer, the higher event rate required use of the newer LeCroy 3412 discriminators and LeCroy 3377 TDC's for their reduced dead time of 11 nsec as opposed to 25 nsec for the 2277's [33].

The planes of hodoscopes were placed in two locations in each spectrometer. The front group was placed between the two Cerenkov tanks while the back group was placed directly behind the second Cerenkov detector. This gave a separation of about 5 or 6 meters along the path of the electrons. With the fine segmentation of the hodoscopes, this separation was sufficient to give angular resolution of $\sim$0.4 mrad and position resolution of $\sim$5 mm as measured at the location of the shower counter [64].

<u>Shower Counters</u>

The lead-glass shower counters used in E154 were the same detectors developed for the previous experiments E142 and E143. Each consisted of 200 blocks arranged in a 20-row by 10-column array. The individual blocks were 6.2 cm square by 75 cm long and composed of F2 lead glass [34].

Lead glass is a transparent glass composed of lead oxide (PbO 55%) and silicon dioxide (SiO_2 45%), which acts as a Cerenkov radiator. Charged particles traveling at high velocity in the material will tend to initiate an electro-magnetic shower through bremsstrahlung radiation and $e^+ \ e^-$ pair-production. The F2 lead

glass has an index of refraction of $n = 1.62$ so most of the particles in the shower will radiate Cerenkov light. Each block was attached to a 2-inch Amperex XP2212PC photo-multiplier to collect the Cerenkov light. The number of secondary particles is directly proportional to the incident energy of the particle; therefore, the Cerenkov signal can be calibrated to give an accurate measure of the incident particle's energy. Also, since the initial probability for bremsstrahlung radiation from a particle of mass M is inversely proportional to M^2, an electron is almost six orders of magnitude more likely to initiate an electro-magnetic shower than a pion or other hadron of the same incident energy. The dominant hadronic interaction is usually initiated by the strong nuclear reaction between the incident hadron and the nuclei of the material, such as $\pi^- + p \rightarrow \pi_0 + n \rightarrow 2\gamma + n$. In such a reaction, the outgoing photons will initiate electro-magnetic showers whose Cerenkov light will also be detected. As a result, an incident electron has a high probability ($> 99\%$) of electro-magnetically interacting early in the material and depositing all of its energy. Incident hadrons will deposit less than 10% of their energy electro-magnetically, and the nuclear interaction, with its lower total cross section, is more likely to occur deep within the material such that all of the hadron's energy may not be recorded. This difference in energy deposition allows additional information for the discrimination between electrons and pions (or other hadrons) in the spectrometers.

The signal from the photo-multipliers was run through a passive signal splitter and recorded in both an ADC and TDC system. The ADC's were LeCroy 2282 modules gated to record the signal integrated over the entire beam pulse. The

TDC's were set up with time over threshold discriminators from LeCroy (4413 and 3412) and LeCroy multi-hit TDC's (2277 and 3377). For 64 of the blocks in the 2.75° spectrometer that were expected to have the highest event rates, the TDC signal for each block was passed through an active splitter and fed to 3 separate levels of discriminators and TDC's. The time information at different discriminator levels allowed accurate measurement of energy sharing among multiple pulses in the ADC.

2.1.4 The Beam Polarimeter

A single-arm Møller polarimeter system [35] consisting of a polarized foil target and a single magnetic spectrometer was used to measure the polarization of the beam. Møller scattering is discussed in more detail in other papers [35, 36]. Therefore, its application for a beam polarization measurement will only be briefly described here.

Møller scattering refers to elastic electron-electron scattering [36]. The spin dependent cross section for this process is given by:

$$\frac{d\sigma}{d\Omega} = \left(\frac{d\sigma_0}{d\Omega}\right)\left[1 + \sum_{i,j} P_B^i A_{ij} P_T^j\right] \tag{2.3}$$

where P_B^i and P_T^j refer to the components of the beam and target polarizations, respectively. The axes are defined such that the z axis is along the beam direction and the y axis is vertical. The quantity $d\sigma_0/d\Omega$ refers to the unpolarized cross section and A_{ij} are the asymmetry terms due to the polarization of the beam and target electrons.

Møller scattering is very well understood, both experimentally and theoretically in QED. Therefore, the unpolarized cross section and the asymmetry terms are well known. With that and a known target polarization, a very precise measurement of the beam polarization can be accomplished. For longitudinally polarized electrons, the only asymmetry term that contributes is the A_{zz} term, which is only a function of the center of mass scattering angle θ_{CM}. At its maximum ($\theta_{CM} = 90°$), $A_{zz} = -7/9$. With an unpolarized cross section of 0.179 b/sr, typical target foil polarizations of 0.08, and expected beam polarization of ~ 0.8, the expected asymmetry would be roughly 0.05, which is measurable to within $\sim 2\%$ relative.

The E154 Møller polarimeter was placed upstream of the ^{3}He target apparatus. The entire setup (shown in Fig. 2.8) consisted of a separate target apparatus, a mask to define the acceptance, a magnet for momentum analysis of the scattered electrons, and a detector package to measure the scattering rate. The target apparatus consisted of six iron-cobalt foils with thicknesses ranging from 20μm - 154μm placed at a 20.7° angle to the beam. The foils were magnetized in a 100 G field provided by a set of Helmholtz coils. The detector package used five silicon detectors in a lead lined detector hut (shown in Fig. 2.9). The four lower detectors were mounted in a fixed location and had a coarse segmentation (~ 8.69 mm) in the vertical direction. The upper detector, with a finer segmentation (~ 2.18 mm), was mounted on a remotely controlled X-Y stage that could be positioned anywhere within the Møller acceptance. The signal from the detectors was integrated in ADCs, and an asymmetry was measured proportional to the beam polarization.
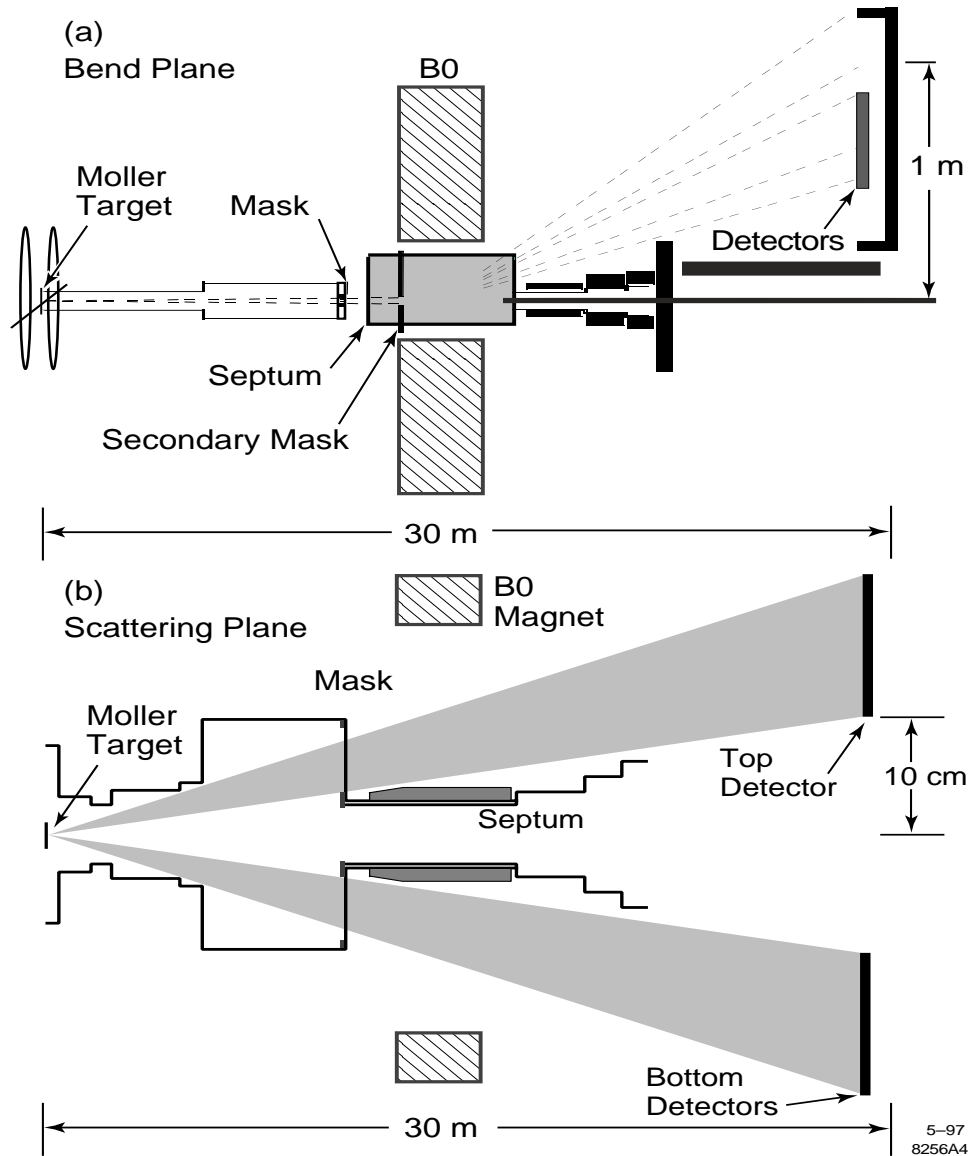
Figure 2.8: Top and side views of the E154 Møller Polarimeter. Each plot shows the Møller target and the septum and B0 bend magnets used to deflect the Møller electrons onto the detectors. In addition, a mask (shown) was placed at the entrance to the B0 bend magnet to help reduce backgrounds in the Møller detectors. The detector package is shown in Fig. 2.9.
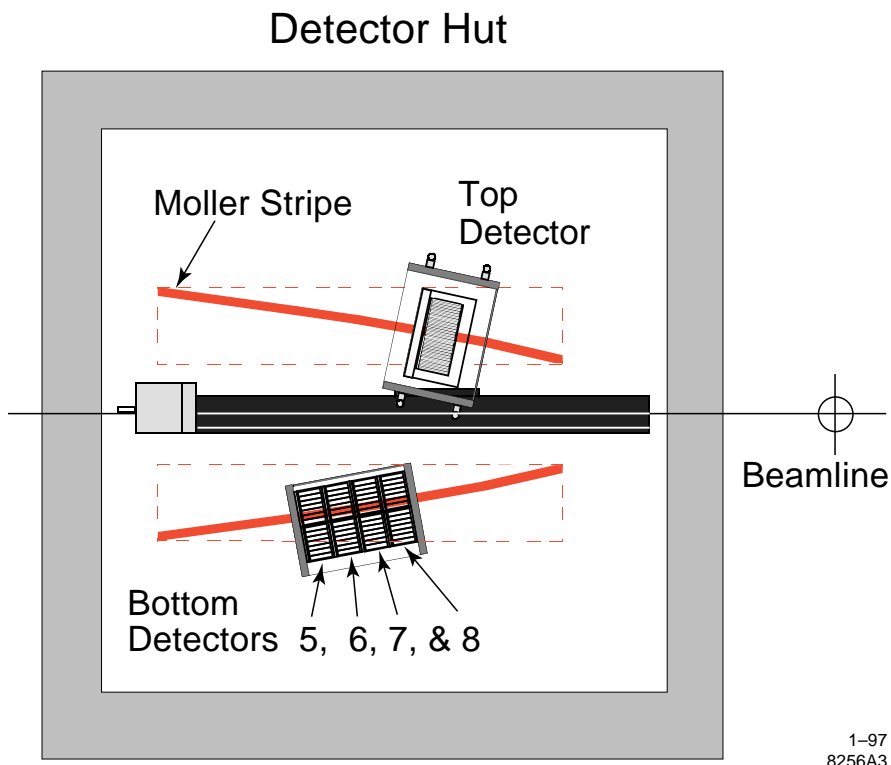
Detector Hut

Figure 2.9: The E154 Møller detector package. The detectors were placed inside a lead hut. The four lower detectors were mounted in a fixed location and had a coarse segmentation (∼8.69 mm) in the vertical direction. The upper detector, with a finer segmentation (∼2.18 mm) was mounted on a remotely controlled X-Y stage that could be positioned anywhere within the Møller acceptance. Also shown is the expected location of Møller electrons in the detector hut (labeled Moller Stripe).

2.1.5   Data Acquisition

The increased data rates, resulting from the shorter beam pulse (∼200 ns compared to ∼1.5 μs for previous long pulse experiments) and higher energy beam (50 GeV compared to 28 GeV for previous fixed target experiments), required a complete redesign of the data acquisition system from that used for E142/E143. The individual electronic systems used for each detector system have been described above. All of the discriminators, TDCs, and ADCs, were part of the already existing

CAMAC system from previous experiments. To improve the readout and processing speed, a new DAQ system [37] was designed that was distributed over a number of VME crates, using a reflective memory system. In addition, the detector CAMAC electronics system was located inside one of the detector huts to reduce cable length and signal degradation. The digitized data from the CAMAC systems was readout through a VME Subsystem Bus extension (VSB) which would not interfere with other VME activities. In addition to the CAMAC data, the Cerenkov FADCs operated in the VME system itself. A reflective memory network was responsible for the inter-VME communication, synchronization, and data sharing. Communication with non-VME components used either Ethernet or FDDI networks.

A block diagram of the VME based DAQ system is shown in Fig. 2.10. The DAQ system contains three VME crates. All real-time components of the DAQ were located in two of the VME crates: the remote VME crate, located in the detector hut with the rest of the detector electronics, and the local VME crate, located in the ESA Counting House. The third, or Unix VME crate, was also located in the Counting House, and contained UNIX processors and interfaces to the data storage systems.

The overall run control of the experiment was performed on a VAX 4000.200 station located in the Counting House. In addition, data logging was performed through the SLAC Computer Services (SCS) Silo system with a remote data server and an FDDI link. The remote data server process, operating on an SCS IBM RISC6000 workstation, stored the data from each run on disc. At the completion
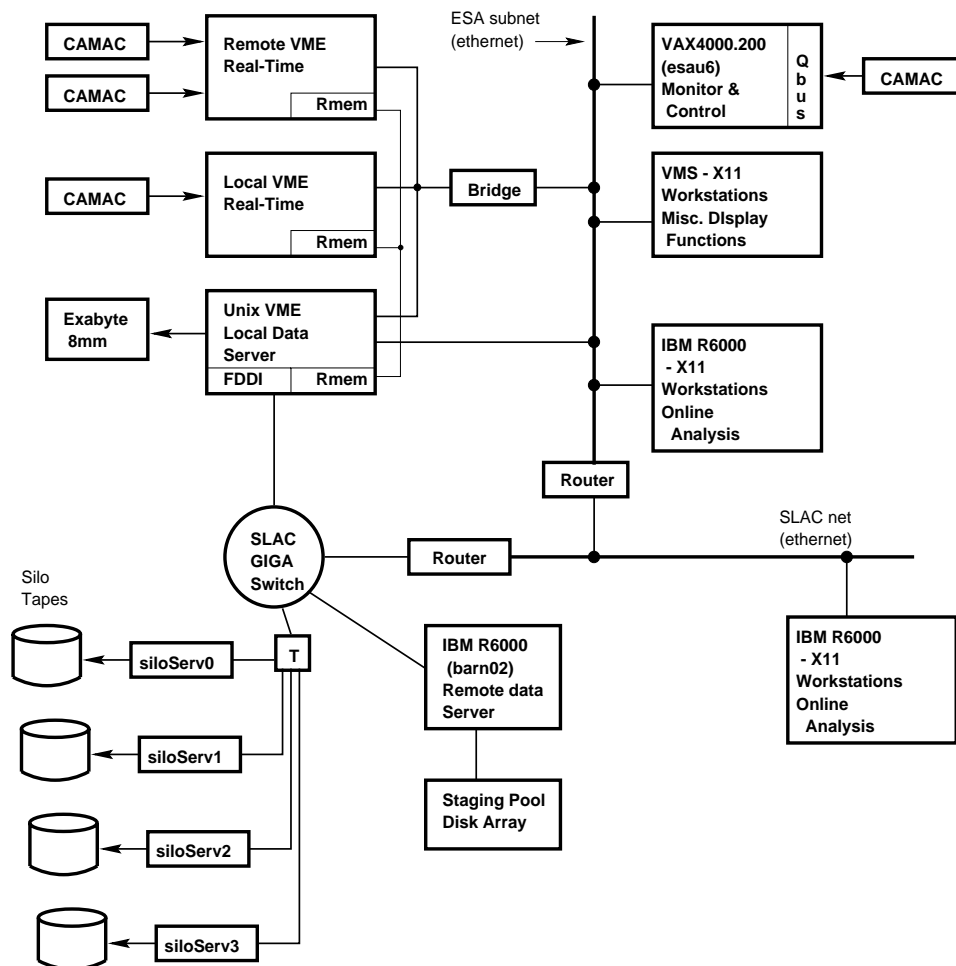
Figure 2.10: Block diagram of the ESA VME based DAQ hardware components. All real-time components of the DAQ were located in the remote VME crate, located in the detector hut with the rest of the detector electronics, and the local VME crate, located in the ESA Counting House. The Unix VME crate, was also located in the Counting House, and contained UNIX processors and interfaces to the data storage systems. Also shown are the connections to VAX workstations used for run control and various monitoring functions, to IBM R6000 workstations for online analysis and to the Slac Computer System for data storage and offline analysis.

of a run, the data were staged out to the silo system for permanent tape storage.

2.2   Run Plan

The goal of experiment E154 was to measure $g_1(x, Q^2)$ of the neutron. There-

fore, as mentioned in Sec. 1.1, the primary measurement required was the parallel

asymmetry $A_\parallel$. However, a high precision measurement of g_1^n requires additional

measurements of other quantities. From the definition (Eq. 1.6) we can see that a

measurement of the transverse asymmetry $A_\perp$ is also necessary for a precise calcu-

lation of g_1.

In addition, the actual measured asymmetries require corrections for target

and polarization effects, as well as correct elimination of background contamination

to achieve the necessary pure electron asymmetries. The uncorrected or raw asym-

metries constructed from the data $(A_{\parallel,\perp}^{raw})$ were corrected for target dilution (f),

target polarization (P_t), and beam polarization (P_B) to construct the un-subtracted

asymmetries $A_{\parallel,\perp}^{unsub}$:

$$A_{\parallel,\perp}^{unsub} = \frac{1}{fP_BP_t}A_{\parallel,\perp}^{raw}. \tag{2.4}$$

The measured asymmetries $(A_{\parallel,\perp}^{meas})$ were then extracted by correcting for the un-

polarized background processes with a background dilution factor α_{back} and the

polarized backgrounds with background asymmetries $A_{\parallel,\perp}^{back}$:

$$A_{\parallel,\perp}^{meas} = \frac{1}{1 - \alpha_{back}} \left[A_{\parallel,\perp}^{unsub} - \alpha_{back}A_{\parallel,\perp}^{back} \right]. \tag{2.5}$$

The details of the background corrections will be discussed in Sec. 3.3. For

this discussion it is sufficient to point out that the two primary backgrounds in E154 came from pions or other negatively charged hadrons entering our detectors, which were measured during normal running conditions, and electrons from pair-symmetric processes, which required an additional experimental setup for measurement. In addition, both the target dilution factor and beam polarization used in Eq. 2.4 required separate experimental setups for measurement.

The following sections will discuss the methods used to estimate the optimal time allotments for each of these additional experimental measurement in order to minimize the overall uncertainty on g_1.

2.2.1   Transverse Polarization

From the definition (Eq. 1.6) we can see that the uncertainty on our knowledge of $A_\perp$ will propagate to our total uncertainty on g_1. In many previous experiments, measurements of $A_\perp$ were neglected. Instead, g_1 was re-written as a function of $A_\parallel$ and A_2. Then, the positivity constraint (See Sec. 1.3.5) was used as a bound on the possible uncertainty in A_2. However, with the intended statistical accuracy of $A_\parallel$ for this experiment, the error contributed from the positivity constraint would dominate the error on our measurement of g_1^n for $x < 0.3$, despite the reduced effect of $A_\perp$ or A_2 due to the kinematic factors.

To measure $A_\perp$, we need to measure an asymmetry with the target transversely polarized. For this experiment, we could not optically pump the target polarization in transverse mode. To obtain transverse polarization, the target was

first brought to maximum polarization in the longitudinal mode. Then, with the lasers turned off, the magnetic field from the Helmholtz coils was rotated by 90° to re-orient the polarization. The oven was turned off to reduce the de-polarization rate due to random collisions of the target nuclei, and the target was brought to thermal equilibrium before data could be taken.

Under these conditions, the target would slowly de-polarize from ^{3}He - ^{3}He or ^{3}He - glass collisions with a relaxation constant $(\tau_R) \sim 40 - 70$ hours. If we assume that we only allow the target polarization to fall to 75% of its maximum polarization before re-polarizing, then the average polarization of the target in transverse mode will be $\sim$87% of that for the longitudinal mode. With this information, we can then calculate the optimal running time to spend on transverse mode to minimize the error on g_1 .

Using Eq. 1.6, we can see that the error on g_1 (δg_1) is

$$(\delta g_1)^2 = \left(\frac{F_1}{D'}\right)^2 \left[(\delta A_\parallel)^2 + \tan^2\left(\frac{\theta}{2}\right)(\delta A_\perp)^2\right]. \tag{2.6}$$

Neglecting background contamination, which should be independent of target polarization direction, we can recognize from Eqs. 2.4 and 2.5 that the individual physics asymmetries $A_\parallel$ and $A_\perp$ have errors associated with the raw experimental asymmetries:

$$(\delta A_{\parallel,\perp}^{meas})^2 = \left(\frac{1}{fP_BP_t}\right)^2 (\delta A_{\parallel,\perp}^{raw})^2. \tag{2.7}$$

For the perpendicular case, the target polarization is $0.87P_t$, as mentioned above. The measured asymmetry errors $(\delta A_{\parallel,\perp}^{meas.})$ are simple statistical errors based on the

total number of counts $(N_{\parallel,\perp})$ recorded for that measurement. We can then write:

$$(\delta A_{\parallel,\perp}^{meas})^2 = \left(\frac{1}{fP_BP_t}\right)^2 \frac{1}{N_{\parallel,\perp}},$$

$$(\delta g_1)^2 = \left(\frac{F_1}{D'}\right)^2 \left(\frac{1}{fP_BP_t}\right)^2 \left[\frac{1}{N_\parallel} + \tan^2\left(\frac{\theta}{2}\right)\frac{1}{(0.87)^2 N_\perp}\right]. \qquad (2.8)$$

Assuming consistent beam conditions, the number of counts recorded is directly related to the running time spent $(N_{\parallel,\perp} \propto t_{\parallel,\perp})$. Therefore, grouping all the factors out front into K, we can re-write Eq. 2.8:

$$(\delta g_1)^2 = K^2 \left[\frac{1}{t_\parallel} + \tan^2\left(\frac{\theta}{2}\right)\frac{1}{(0.87)^2 t_\perp}\right]. \qquad (2.9)$$

To optimize the time spent in perpendicular mode $(t_\perp)$ for a given amount of total running time $(t_{total} = t_\parallel + t_\perp)$, we solve for the minimum of Eq. 2.9.

$$0 \equiv \frac{\partial(\delta g_1)^2}{\partial t_\perp} = K^2 \left[\frac{1}{(t_{total} - t_\perp)^2} - \tan^2\left(\frac{\theta}{2}\right)\frac{1}{(0.87 t_\perp)^2}\right],$$

$$\boxed{\frac{t_\perp}{t_\parallel} = \left(\frac{1}{.87}\right)\tan\left(\frac{\theta}{2}\right)} \qquad (2.10)$$

The solution for this is not unique, since there are two spectrometers in the experiment $(\theta = 2.75°, 5.5°)$:

$$\frac{t_\perp}{t_\parallel}(2.75°) = 0.028,$$

$$\frac{t_\perp}{t_\parallel}(5.5°) = 0.055. \qquad (2.11)$$

2.2.2 Positron Contamination

The phrase "positron contamination" refers to non-DIS background processes of pair-symmetric particle production. The products of these processes are electron-

positron pairs. The electrons from such a process can be detected by our spectrometers and are indistinguishable from the nominal DIS electrons. To measure this background, we reversed the polarity of the magnets in our spectrometers. The spectrometers then selected positrons, which primarily result from these pair-symmetric background processes. Corrections were then made for the effect of this background in the data analysis. (See Sec. 3.3 for more details of the subtraction process). Two forms of correction were applied. The positron dilution factor (f^+), which corrected for the additional number of electrons measured due to the positron contamination, was computed from the measured positron rate (r_e^+) and the DIS electron rate (r_e^-), (please note, with this notation and neglecting pion or other background contamination, the raw measured electron rate is $r_{e^-} + r_{e^+}$):

$$f^+ = \frac{r_{e^+}}{r_{e^-} + r_{e^+}}. \tag{2.12}$$

In addition, any possible asymmetry in the pair-symmetric processes (A^{e^+}) was measured while the spectrometers were reversed. Both corrections were applied as in Eq. 2.5 giving

$$A_{\parallel,\perp}^{meas} = \frac{1}{1 - f^+} \left[A_{\parallel,\perp}^{unsub} - f^+ A_{\parallel,\perp}^{e^+} \right]. \tag{2.13}$$

Since we expect to record several million events, the error on f^+ will be negligible compared with that of the asymmetries. Therefore, neglecting its contribution, the error due to the measurement of A^{e^+} will be

$$(\delta A_{\parallel,\perp}^{meas})^2 = \left(\frac{1}{1 - f^+} \right)^2 (\delta A_{\parallel,\perp}^{unsub})^2 + \left(\frac{f^+}{1 - f^+} \right)^2 (\delta A_{\parallel,\perp}^{e^+})^2. \tag{2.14}$$

The statistical uncertainties on the measured asymmetries A^{unsub} and A^{e^+} are based on the total number of counts ($\propto \sqrt{1/N}$) recorded in each mode. Since the number of counts recorded is directly related to the rate of production and the time spent, there results

$$N_{e^+} = r_{e^+} t_{e^+} \text{ and } N_{unsub} = (r_{e^-} + r_{e^+}) t_{unsub}.$$

We can then make the following relations:

$$(\delta A^{e^+})^2 \propto \frac{1}{r_{e^+} t_{e^+}} \text{ and } (\delta A^{unsub})^2 \propto \frac{1}{(r_{e^-} + r_{e^+}) t_{unsub}}.$$

Assuming a fixed running time ($t_{unsub} = t_{total} - t_{e^+}$) and equal incoming beam intensities for electron and positron modes, the optimal running time is then calculated:

$$0 \equiv \frac{\partial (\delta A^{meas})^2}{\partial t_{e^+}} = \left(\frac{1}{1 - f^+} \right)^2 \left(\frac{1}{r_{e^-} + r_{e^+}} \right) \left(\frac{1}{t_{unsub}} \right)^2 - \left(\frac{f^+}{1 - f^+} \right)^2 \left(\frac{1}{r_{e^+}} \right) \left(\frac{1}{t_{e^+}} \right)^2,$$

$$\boxed{\frac{t_{e^+}}{t_{unsub}} = \sqrt{f^+}}. \tag{2.15}$$

For an accurate run plan calculation, it is necessary to have an estimation of the value for f^+. A parameterization was created by the author from previous experimental data that provides an acceptable prediction (see Appendix C for full details on the parameterization). The prediction, and the previous data, indicate that f^+ is a function of x. Therefore, there is no optimal solution for the entire kinematic coverage of the experiment. However, since one of the fundamental advantages of this experiment over the previous E142 is the increased kinematic coverage at low values of x, it is desirable to emphasize that range. Unfortunately, that is also where f^+ is large ($\sim 15\%$).

2.2.3   Target Dilution Measurement

The target dilution factor f is the ratio of polarized to unpolarized nucleons in the target. For a pure polarized ^{3}He target with no additional scattering material, $f = 1$. Based on careful measurements of the materials used in the construction of the targets, a model calculation of f can be obtained. Since the target is not uniform in all directions, variations in beam characteristics may cause the incident or scattered electrons to interact with differing thicknesses of materials. To accurately calculate the dilution factor for those electrons measured in the detectors, precise models of the beam characteristics and spectrometer acceptances were required. To cross-check the use of these models, the dilution factor can be directly measured with the beam itself. A special "reference cell" target was constructed that allowed variable pressures of the ^{3}He gas between 0 and 150 psia. At 0 pressure, we measure the electron scattering rate coming directly from the glass end windows and walls of the target. By measuring the rates at different pressures of ^{3}He, we extract the contribution of counts due to the helium.

Ideally, for a reference cell with identical construction to a polarized cell and consistent beam conditions, we could do a careful measurement of the dilution factor at the beginning of the experiment and never need to measure it again. However, possible variations in beam and spectrometer conditions, as well as the necessity of using several different polarized target cells, all with slightly different constructions, require the periodic measurement of the dilution factor which cannot be accurately

predicted. Since the dilution factor only requires the measurement of rates, $\sim 30,000$ events are sufficient to insure an uncertainty of less than 1%. At 120 Hz and ~ 0.3 events/pulse, an individual dilution measurement could be made in less than 30 minutes ($\sim$10 minutes with the cell full and $\sim$15 minutes with the cell empty).

2.2.4 Møller

The Møller system is used to measure the polarization of the incoming beam (see Sec. 2.1.4 for details). An individual Møller measurement only takes about 30 minutes to an hour. At that point the error on the polarization measurement is systematics dominated at about 2%. However, as with the dilution factor measurement above, possible changes in the incoming beam's characteristics may alter the beam's polarization. As a result, it was impossible to predict exactly how much time to use for Møller measurements until we had a feeling for the variability of the beam. Therefore, fairly frequent measurements were expected early in the experiment to attempt to assess the beam's stability followed by a decrease in the frequency of Møller measurements to match the needs of the beam.

2.2.5 Other Systematic Studies

In addition to the runs listed above, there are a few calibrations and systematics studies that can be useful if time is available. One possible study, which was in the original proposal but was not actually performed, would have used a lowered beam energy of 30 GeV. This would have aided in the measurement of Q^2

dependence for the radiative corrections. Also, it would have provided a possible overlap to the previous data from E142 that was taken at a similar beam energy.

One of the very necessary calibrations studies was the determination of the spectrometers' characteristics. Accurate knowledge of the acceptance and central momentum were necessary for measuring the kinematics of recorded events. Two separate calibration runs were used to measure the spectrometers' acceptance. One of these used a so-called sieve slits collimator. This collimator is composed of a thick piece of tungsten placed such that it completely obscures the acceptance of the spectrometer. A few precisely aligned holes were drilled into the tungsten to allow electrons to enter the spectrometers. Then any measured events have very precisely calibrated positions because of the known locations of the holes in the collimator. The known position information can then be compared with the results from the tracking analysis extrapolated back to the location of the collimator.

The other acceptance measurement required the lowering of the incoming beam energy to ∼8 GeV. At that energy, elastic scattering dominates the measured events. As a result, the elastic peak, which is extremely well known from previous experiments, could be measured. Comparison of our measurement to the previous worlds' data gave a very good calibration of the behavior of our detectors.

2.2.6   Run Plan Summary

The previous sections provide an explanation of the various factors that enter into a run plan design before an experiment is run. However, during an actual

experiment, outside forces such as hardware failures or laboratory scheduling can have a profound impact on run scheduling. During E154, in addition to the measurements discussed above, a 5-minute measurement of the ^{3}He target polarization was performed every 4 - 6 hours. Table 2.3 shows the actual time spent for each of the different running modes for E154. The hours have been normalized to the E154 proposal of 10^{11} electrons/pulse, 120 pulses/second, and an 80% polarized target. With the exception of the Møller and reference cell runs, times are listed for both spectrometers individually since the 2.75° spectrometer had a variable acceptance which was used to alter the relative data rates between the two spectrometers.

| Experimental | Normalized Hours of Data | |
Mode	2.75° Spec.	5.5° Spec.
$A_\parallel^{raw}$	300	208
$A_\perp^{raw}$	31	8.5
$A_\parallel^{e^+}$	42	10
$A_\perp^{e^+}$	0	0
Reference Cell	61	
Møller	18	

Table 2.3: Final running times for E154. The times shown are the actual hours of data taken during E154 for each experimental setup. The hours are normalized to an incoming beam of 10^{11} electrons/pulse and 120 pulses/second. In addition, the asymmetries are further normalized to an 80% polarized ^{3}He target, an 80% polarized electron beam, and spectrometer acceptances from the E154 proposal.

CHAPTER 3

DATA ANALYSIS

The data analysis proceeded in three stages: (1) the run-by-run analysis; (2) the combining of runs for which data were taken under the same conditions (parallel, perpendicular, positrons); and (3) the applications of corrections and subtractions to create actual electron asymmetries from the measured counts. An individual run represents about 20 - 30 minutes of data. In addition, special runs with empty and full dummy cells were conducted about every 8 hours to track systematic drifts.

3.1 Individual Run Analysis

3.1.1 Beam

The beam analysis was used mainly to eliminate data taken during sub-standard conditions. Severe excursions in the beam's position at the target, current, or spatial distribution could have a significant impact on the measured asymmetry. Since an off-center beam will go through a longer path length of the glass in the target cell and yet still travel the same length of ^{3}He , variations in the beam position or size primarily result in a change in the dilution factor for the target. A severe current variation, on the other hand, most likely indicates large amounts of beam loss upstream, which have the potential for allowing secondary particles to enter

54

the end station and strike the target. This would result in our detectors recording events with unknown incident beam characteristics.

Studies were done to evaluate the sensitivity of the asymmetry measurement to the beam characteristics [38]. In all cases, a very large excursion was necessary before any effect could be perceived. As a result, very loose analysis cuts were placed on the beam parameters that would eliminate only the most extreme of conditions. Table 3.1 shows the cuts used for this analysis.

Beam Parameter	Min. Cut	Max. Cut	Typical Range
Good Spill (adc counts)	5.0	2000.0	600 - 1200
Bad Spill (adc counts)	0.0	2000.0	300 - 1000
Toroids (adc counts)	1.0	-	1600 - 1800
X-position (mm)	0.0	4.0	2.4 - 2.9
X-width (mm)	0.5	3.0	1.3 - 1.5
Y-position (mm)	-4.0	0.0	-2.0 - -2.7
Y-width (mm)	0.3	3.0	0.7 - 1.0

Table 3.1: Typical values for the beam cuts used in the E154 analysis. The adc cuts were determined from data while the beam X and Y positions were determined empirically to match the center of the target. The position cuts were used to insure that the beam would not hit the edge of the target cell.

In addition, left-right asymmetries in beam charge and position at the target were studied to minimize any systematic bias on the measured asymmetry [39]. It was found that beam dependent bias to the measured asymmetry does not exceed 5×10^{-5} with the following beam and position asymmetry restrictions:

$$
\begin{aligned}
|A_{charge}| \equiv \left| \frac{(q_L - q_R)}{(q_L + q_R)} \right| &< 5 \times 10^{-4}, \\
|A_{X-pos}| \equiv |\langle X_L \rangle - \langle X_R \rangle| &\leq 0.004 \text{ mm}, \\
|A_{Y-pos}| \equiv |\langle Y_L \rangle - \langle Y_R \rangle| &\leq 0.005 \text{ mm}.
\end{aligned}
\tag{3.1}
$$

Here L and R refer to left- and right-handed beam conditions respectively; q refers to incoming beam charge, and $\langle X \rangle$ and $\langle Y \rangle$ are the average X and Y positions at the wire array. Out of a total of about 2500 runs, 34 runs were eliminated from the analysis sample for not satisfying these beam asymmetry conditions.

3.1.2   Lead Glass Calorimeter Analysis

In each spectrometer, the calorimeter acted as the main anchor point of the entire analysis. Hits in each block were defined by an ADC value greater than the pedestal by at least 4 counts. The TDC information was then used to split the energy between multiple hits in the same block and to associate a time with the individual hits.

Once all blocks were checked, and each hit had a corresponding energy and time, a method of cluster association was implemented. For this analysis, the clusters were found using a cellular automaton [40] approach. A much more detailed explanation of the cluster-finding technique is located in reference [40] so only a short summary is presented. The algorithm uses the following steps to define a cluster:

1. Find the peak blocks, defined as those blocks with more energy than any of their eight nearest neighbors.

2. Associate the eight nearest neighboring blocks with each peak block to form a cluster. Any block which neighbors two peak blocks is associated with the peak nearest in time. If timing information is insufficient to distinguish between the

peaks, then the block is associated with the cluster of the higher energy peak block.

3. Examine the sixteen next nearest neighbors of each peak block. If any of these sixteen blocks have non-zero energy and are not already associated with a cluster, then they are assigned to the cluster of the peak block.

All available information about each cluster is then processed by a neural network. The multi-level neural network was originally designed for E142 [40] and has been further studied and improved during E143 and in preparation for E154. It used the energy and spatial distribution of the cluster to determine whether it was most likely the result of an incident electron or hadron. The neural network, which was trained on a pure pion sample, returned a single value between +1 (definitely an electron) and -1 (definitely a hadron) based on its confidence. Fig. 3.1 shows a typical distribution of the neural network response for real data.

Upon completion of the clustering analysis, each cluster has four identifying characteristics:

- Total energy of the cluster,

- Time of the cluster,

- Location of the cluster, calculated as an average of the locations of the blocks involved in the cluster, weighted by the energy in the block,

- Neural Network value for electron - pion identification.
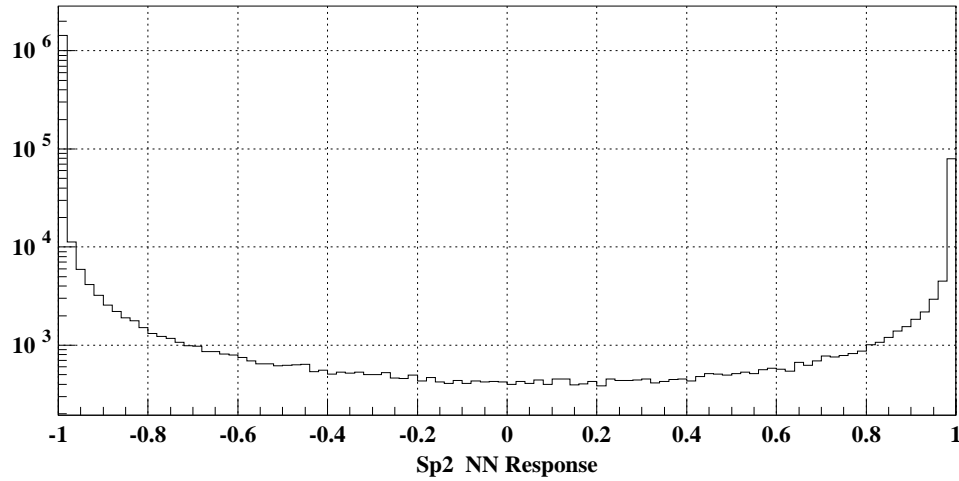
Figure 3.1: Typical response of the neural network for all tracks (Note the log scale). This plot shows actual data from one run during E154. The neural network, which was trained on a pure pion sample, returns a single value between +1 (definitely an electron) and -1 (definitely a hadron) based on its confidence. Based on efficiency studies, the optimal electron definition includes a neural network ≥ -0.98.

3.1.3   Tracking

The tracking algorithm used information from the calorimeter, Cerenkov and hodoscope systems. All tracks are required to have a minimum number of hits in the hodoscopes. For the 2.75° spectrometer, four out of the six front hodoscope planes and three out of the four rear hodoscope planes are required to record a hit for the track to be valid. Similarly for the 5.5° spectrometer, three out of four hodoscope planes are required for both the front and back planes. There are four classifications of tracks that can be identified based on the detector systems that can be associated with the track:

Class 1 -   A shower cluster, at least one Cerenkov hit, and at least the minimum number of hodoscope hits

Class 2 -   A shower cluster and at least the minimum number of hodoscope hits.

No associated Cerenkov hit can be found

Class 3 - At least one Cerenkov hit and at least the minimum number of hodoscope hits. No shower cluster can be associated with this track

Class 4 - Hodoscope hits only

(Note, track class is exclusive.)

Tracks of class 1 and 2 are the normal candidates for electrons and pions, respectively. Classes 3 and 4 are used mainly for calibration purposes and will not be discussed here.

The tracking code starts by iterating over all available clusters from the calorimeter analysis. For each cluster, it looks for Cerenkov hits in either tank that are within a time window defined to be three times the timing resolution. The timing resolution is normally about 1 ns. Next, the hodoscope hits are evaluated with both timing and angle and position constraints to determine which ones could be associated with the cluster (and Cerenkov hits if available).

The kinematic cuts used to select hodoscope hits are based on the fact that the position of the hits in the calorimeter are well correlated with the momentum direction of the particle. Therefore, looking upstream from the cluster in the calorimeter, there exists only a limited window in the hodoscopes from which a particle from the target could have emerged. The code checks this area for possible hodoscope hits. Once all possible hodoscope hits have been identified, then a chi-squared test is applied. All possible combinations of hodoscope hits are attempted

in a linear fit with the cluster position in the shower cluster. The track with the best chi-squared is selected. Those hodoscope hits used for that track are eliminated from all further analysis, and the tracking code moves on to the next cluster.

Once a track has been constructed, the position and angle of the track can be used to determine the momentum and scattering angle of the particle. Using the measured magnetic fields of the two dipole magnets in each spectrometer, and the quadrupole magnet in the 2.75° spectrometer, a Monte-Carlo simulation was run to create transport matrix elements from the target to the calorimeter in each spectrometer. From these, reverse matrix elements were constructed that could return the momentum of the particle based on position and angle at the shower counter.

Each track now has four identifying characteristics:

- Track Class,

- Time of the track,

- Momentum of the track,

- Physics angle of the track from the target, calculated using the known angles of the spectrometer and the X-Y position and angle for the track.

Also, each track has pointers to the associated cluster and Cerenkov hits, if they exist.

3.1.4   Particle Definitions

For the event selection, we want to create an electron definition that will achieve the smallest total error after all backgrounds have been subtracted. Since the major background contamination is due to pions or other hadrons, most of the cuts were applied to improve our ability to identify or eliminate pion contamination. All cuts have been studied to insure that they do not impose a non-physical asymmetry on the data. In addition to the electron definition, a pion definition was also selected. The pion definition allows the measurement of a pion asymmetry, which can be used to eliminate the effect from pion dilution in the electron sample. There are 7 cuts applied to the data.

<u>Track Class</u>

The first selection criteria is the track class. Since the Cerenkov tank is set up to provide the first order electron/pion differentiation, a class 1 track is assumed to be the basis for an electron definition, while a class 2 track is the basis for a pion definition.

<u>Cerenkov Hits</u>

The class 1 track is defined to contain at least one Cerenkov hit in time with the associated cluster and hodoscope hits. Due to scintillation properties of the gas in the Cerenkov detectors, there is a small probability that pions could scintillate and be detected. Raising the minimum signal in the Cerenkov tank can improve

the rejection of pions. Also, requiring both Cerenkov tanks to fire in coincidence greatly reduces the contamination. Therefore, an electron candidate was required to have both Cerenkov tanks record a signal with a peak hight greater than 25 flash ADC counts. The 25 count threshold, which corresponds to approximately 1.7 photoelectrons, was chosen to optimize the pion rejection without eliminating too many of the electrons (see Fig. 3.2).
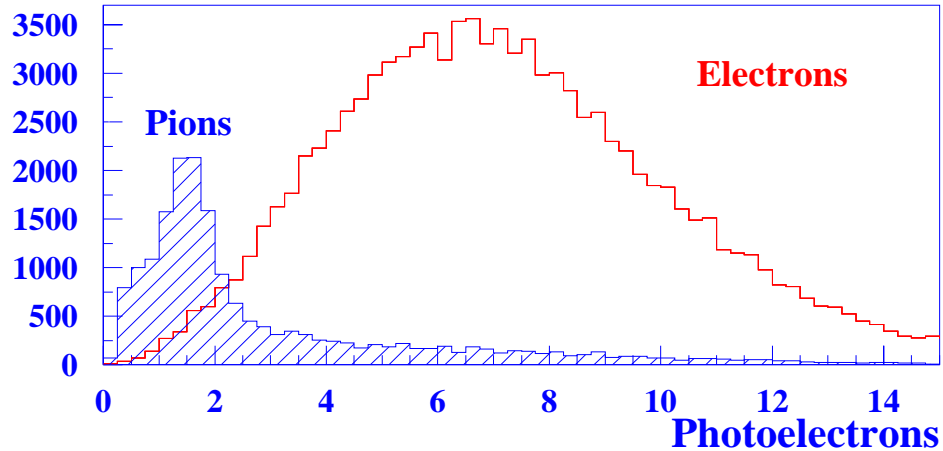
Figure 3.2: Typical Cerenkov response in photoelectrons. The electron and pion samples were selected by using all particle definition cuts excluding the Cerenkov detectors. The compete electron definition requires a peak Cerenkov signal of greater than 25 FADC counts which corresponds to ~1.7 photoelectrons.

Energy vs. Momentum

As discussed in Section 2.1.3 the shower counter can also be used to distinguish between electron and pions. The electrons have a greater than 99% probability to deposit all of their energy into the calorimeter through an electro-magnetic shower. The pions, on the other hand, are much less likely to deposit all of their energy. Pions that only interact through electro-magnetic processes will likely deposit

less than 1% of their total energy, while the energy deposition from initial nuclear reactions, between the pions and the nuclei of the material, will have a broader distribution. A simplistic distinction between electrons and pions can be constructed by comparing the measured momentum of a track (p) to the energy of the associated cluster (E). In the case of an electron the ratio of these should be very close to one ($E/p \approx 1$), while a pion will most likely be less. A typical E/p spectrum is shown in Fig. 3.3 with an obvious electron peak at $E/p \approx 1$. The peak at $E/p \approx 0.1$ corresponds to the pions or other hadrons that interact only electro-magnetically, while the broad continuum between the peaks is most likely hadrons that initially interacted through nuclear processes. Since the rates in E154 were higher than in
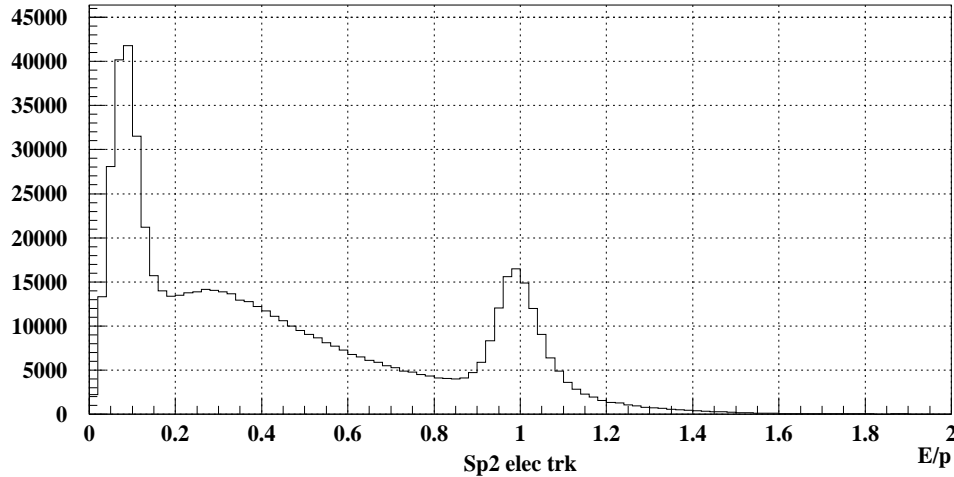
Figure 3.3: A typical E/p spectrum for all candidate tracks (Class 1 and 2) in the 2.75° spectrometer. The enhancement at an E/p value of 1 corresponds to the real electron sample. The peak at $E/p \approx 0.1$ corresponds to the pions or other hadrons that interact only through Cerenkov radiation but do not initiate an electro-magnetic shower, while events in the broad continuum between the peaks are hadrons that initially interacted through nuclear processes.

the previous experiments, there also exists an increased possibility for two clusters to overlap in such a way that one cluster would get too much energy associated with

it. Therefore, we also employ a maximum cut for the E/p. The values used for this analysis are $0.8 < E/p < 1.2$.

Neural Network

As described in Section 3.1.2, a neural network was also employed as a completely independent method of differentiating between electrons and pions in the calorimeter only. The typical neural network response is shown in Fig. 3.1, where a neural network response of -1 refers to a definite pion and a response of +1 refers to a definite electron. Based on Monte Carlo studies, a threshold cut of -0.98 was determined to provide the best efficiency for pion rejection without significant loss of electron statistics. Anything below -0.98 was labeled a pion and anything above was labeled an electron.

Kinematics and Confidence Cuts

As a final safety factor, certain cuts were used to ensure that the events were more likely to be good electrons. First, since clusters in the calorimeter can often spread over many blocks, a cluster near the edge of the calorimeter could have some of its energy leak out the side and not be recorded. For that reason, all clusters that had the peak energy in an edge block were eliminated from our sample. Second, certain physics constraints could be placed on the kinematics of the events to insure that it was valid given the incoming beam characteristics. The kinematic constraints

are:

$$0.01 < x < 0.8$$

$$1.0 < Q^2 < 25$$

$$W^2 > 6.0$$

Summary

Electron Definition:

1. Class 1 track.

2. Both Cerenkov detectors must have a hit in time with the track.

3. Both Cerenkov hits must have a peak amplitude in the FADC > 25 counts.

4. 0.8 <E/p< 1.2

5. Neural Network > -0.98

6. Cluster not peaked on an edge block

7. $0.01 < x < 0.8$; $1.0 < Q^2 < 25$; $W^2 > 6$

Pion Definition:

1. Class 2 track

2. 0 <E/p< 0.2

3. Neural Network < -0.98

4. Cluster not peaked on an edge block

5. $0.01 < x < 0.8$

3.2   Combining Runs

For each spill, the above cuts were applied. A separate tally of electron and pion events was recorded for each run. Each event was binned according to the polarization of the incoming electron and the value of x calculated from the track kinematics of the outgoing electron. The events tallied in each run were combined to form an asymmetry based on the polarization of the incoming electron and normalized to the incoming charge, giving

$$A^{raw} = \frac{\frac{N_L}{q_L} - \frac{N_R}{q_R}}{\frac{N_L}{q_L} + \frac{N_R}{q_R}}. \tag{3.2}$$

Here $N_{L(R)}$ refer to the number of events recorded with the incoming beam in the left (right) helicity state, and $q_{L(R)}$ refers to the total incoming beam charge for that helicity state. Each x-bin was then corrected for the electroweak asymmetry (A_{EW}) arising from the additional weak coupling to left handed electrons only [41], giving

$$A_{EW} \approx -10^{-4}Q^2(0.77\,[1 + 0.44R_s(x)] + 0.11Y), \tag{3.3}$$

where

$$Y = \frac{1 - (1 - y)^2}{1 + (1 - y)^2 - y^2\frac{R(x,Q^2)}{1+R(x,Q^2)}}, \tag{3.4}$$

and the factor

$$R_s(x) = \frac{2s(x)}{u(x) + d(x)}, \tag{3.5}$$

calculated from the up (u), down (d) and strange (s) quark distributions, is small for these kinematics, but not well known. For this analysis, we used:

$$R_s(x) = 0.5 \text{ for } x < 0.2 \text{ ,}$$

$$R_s(x) = 0 \text{ for } x > 0.2 \text{ .}$$

A weighted average of A^{raw} was then constructed for each set of runs done under the same running conditions (parallel, perpendicular, positrons), where the individual runs were weighted by the beam polarization (P_b) and target polarization (P_t) for that run, the dilution factor for that target (f), and the statistical error for that run (δA), giving

$$A^{unsub} = \frac{\displaystyle\sum_{runs} P_b P_t f \left(A^{raw} - P_b A_{EW}\right) \left(\frac{1}{\delta A}\right)^2}{\displaystyle\sum_{runs} \left(\frac{P_b P_t f}{\delta A}\right)^2} . \tag{3.6}$$

3.3   Background Subtractions

At this point, we have achieved an asymmetry from the polarized ^{3}He in the target. Target dilution effects from the glass and other external material have been corrected. The polarizations of the target and the incoming beam have also been accounted for. This asymmetry still contains background contaminations, as discussed in Section 2.2. The two major backgrounds that we have to deal with are positrons (actually electrons produced through pair-symmetric processes) and pions. For each x-bin, the effects from these backgrounds will be subtracted out to produce the measured asymmetries in the following manner:

$$A_{\parallel,\perp}^{meas} = \frac{1}{\alpha_{e^-}} \left[A_{\parallel,\perp}^{unsub} - R^+ \left(A_{\parallel,\perp}^{e^+} - \alpha_{\pi^+} A_{\parallel,\perp}^{\pi^+} \right) - \alpha_{\pi^-} A_{\parallel,\perp}^{\pi^-} \right] . \tag{3.7}$$

Here $A_{\parallel,\perp}^{meas}$ refers to the pure electron asymmetry we want to measure, A^{e^+} refers to the measurable positron asymmetry, A^{π^+} and A^{π^-} refer to the pion asymmetries. The other four parameters are background dilution factors defined as follows:

$$
\begin{aligned}
\alpha_{e^-} &= \frac{r_{e^-}}{r_{e^-} + r_{e^+} + r_{\pi^-}}, \\
\alpha_{\pi^-} &= \frac{r_{\pi^-}}{r_{e^-} + r_{e^+} + r_{\pi^-}}, \\
R^+ &= \frac{r_{e^+} + r_{\pi^+}}{r_{e^-} + r_{e^+} + r_{\pi^-}}, \\
\alpha_{\pi^+} &= \frac{r_{\pi^+}}{r_{e^+} + r_{\pi^+}}.
\end{aligned}
$$

Note that r_{e^+} refers to rate of positrons or electrons produced through pair-symmetric processes since their production is identical, while r_{e^-} refers to the rate from strictly DIS electron processes.

3.3.1   Background Asymmetries

It is fairly simple to achieve the additional background asymmetry measurements from the data that is available. As discussed in Section 3.1.4, we have a definition for pion events that we can analyze identically to the electron analysis discussed above. This will then give us a measured pion asymmetry (A^{π^-}). The positron asymmetry is measured in a special set of runs with the spectrometers' polarity reversed (see Sec. 2.2.2 or Appendix C for more details). Those runs are analyzed with the same electron and pion definitions as for electron data to create the positron asymmetry (A^{e^+}) and the positive pion asymmetry (A^{π^+}). The measured asymmetries are shown in Fig. 3.4. Notice that the two parallel pion
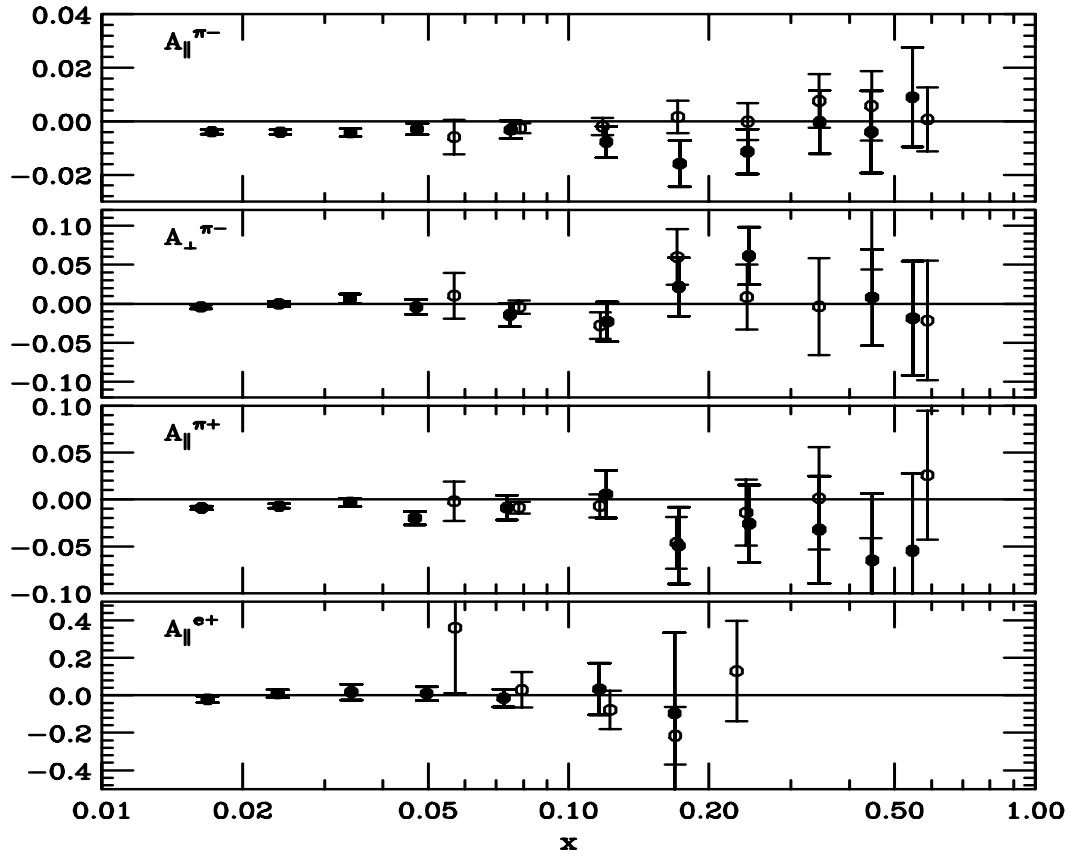
Figure 3.4: The measured background asymmetries. The plots are labeled either $A_\parallel^{\pi^-}$, $A_\perp^{\pi^-}$, $A_\parallel^{\pi^+}$ or $A_\parallel^{e^+}$. In each plot, ● refers to the 2.75° spectrometer, ○ refers to the 5.5° spectrometer. No perpendicular data was recorded in positron mode. Notice that the two parallel pion asymmetries are non-zero at low x.

asymmetries ($A_\parallel^{\pi^-}$ and $A_\parallel^{\pi^+}$) show a distinct difference from zero. The positron asymmetry ($A_\parallel^{e^+}$), however, is quite consistent with zero; therefore, this analysis used $A_\parallel^{e^+} = 0$ for all x. No data were recorded for transverse target polarization with the reversed spectrometer polarities (positron mode). As a result, it was not possible to extract a measurement of $A_\perp^{e^+}$ or $A_\perp^{\pi^+}$. For this analysis both of these asymmetries were assumed to be zero.

3.3.2   Background Dilution

The dilution parameters are slightly more difficult. R^+ is simply the ratio of total counts, normalized to incident charge, recorded in positron mode versus electron mode. Appendix C discusses the method for this in more detail. Notice that the f^+ parameter using in Sec. 2.2.2 is equivalent to R^+ if pion or other hadron backgrounds are neglected. Also, the e^+/e^- ratio calculated by the parameterization in Appendix C and plotted in Fig. C.4 can be related to the R^+ parameter simply by:

$$e^+/e^- = \frac{R^+}{1 + R^+}. \tag{3.8}$$

The method for acquiring the pion dilution parameters depends on measuring the wings of the E/p spectrum. In Fig. 3.5 one can see the typical E/p spectra for a positron run and an electron run after all electron definition cuts, except the E/p cut, have been applied. Both spectra show a Gaussian structure above a background. The signal-to-background structure is easier to see on the positron spectrum due to the significantly lower positron production rate. By fitting the E/p spectrum with
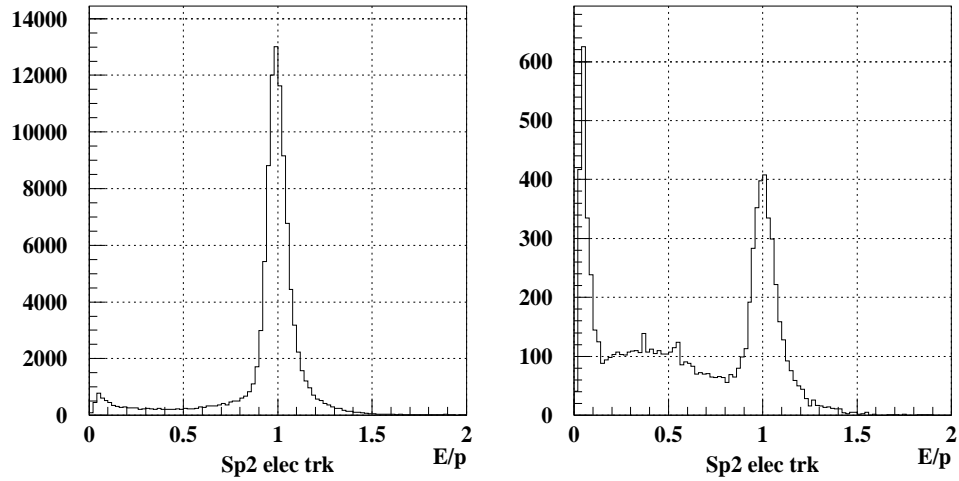
Figure 3.5: Electron E/p spectra with background. Shown are E/p spectra for all candidate events and all x that satisfy the full electron definition as defined in Sec. 3.1.4 without the E/p cut. The left plot shows a typical spectrum from a normal electron run. The right plot shows a spectrum from a positron run. Notice that the background signal is much larger relative to the signal in the positron configuration.

a Gaussian plus background, we can determine the contamination within the region of $0.8 < E/p < 1.2$ that would satisfy the full electron definition. Fig 3.6 shows an example of the fit applied for a positron spectrum. From such a fit, the parameters α_{π^+} or α_{π^-} are the ratios of the integral of the background function to the total integral within the region $(0.8 < E/p < 1.2)$.

Once we have these parameters, we can construct α_{e^-} with the relation:

$$\alpha_{e^-} = 1 - \alpha_{\pi^-} - R^+(1 - \alpha_{\pi^+}) \tag{3.9}$$

These background dilution factors are plotted in Fig. 3.7.
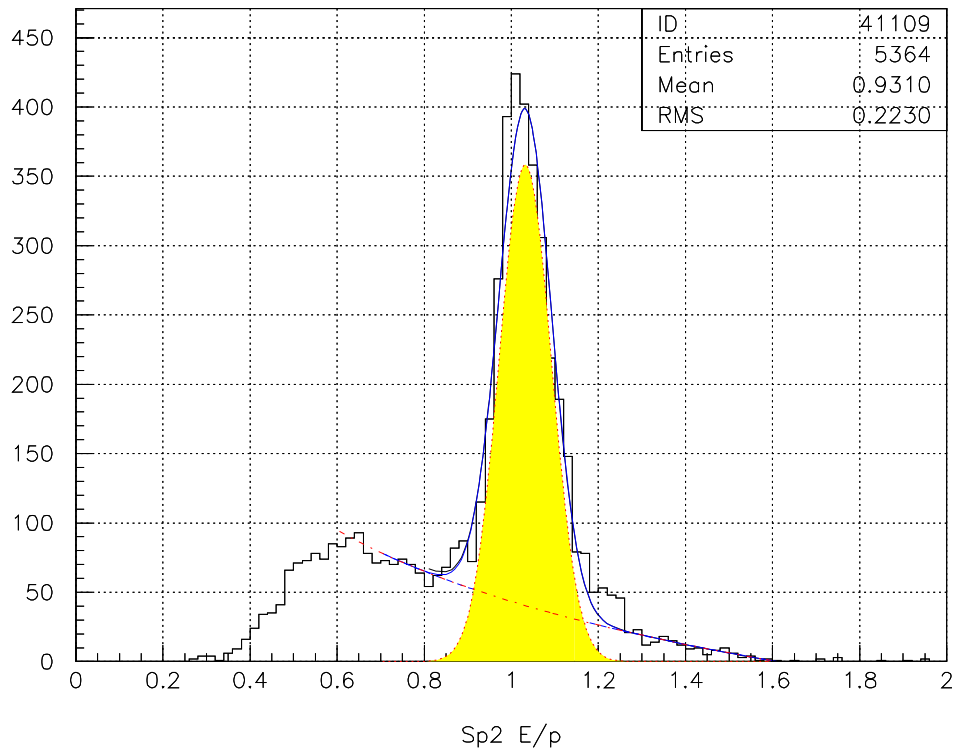
Figure 3.6: A Fit to backgrounds in the E/p spectrum. The E/p spectrum for a positron run is shown. Also shown is a Gaussian fit to the E/p peak and a polynomial fit to the background. The fit was then used to calculate the background dilution under the electron peak.
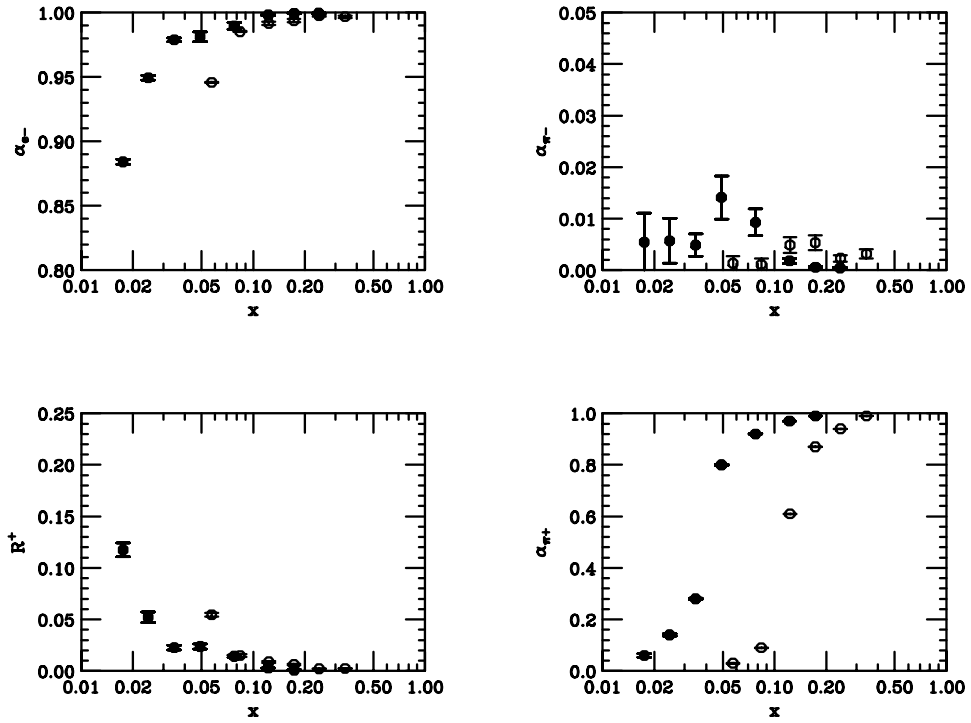
Figure 3.7: The measured background dilutions. The four background dilution factors (labeled $\alpha_{e^-}, \alpha_{\pi^-}, R^+, \alpha_{\pi^+}$) used in Eq. 3.7 are shown with statistical errors only. In all plots, • refers to the 2.75° spectrometer and ○ refers to the 5.5° spectrometer.

CHAPTER 4

RADIATIVE CORRECTIONS

In E154 our goal was to measure asymmetries of the spin-dependent single photon exchange (Born) cross sections ($A_{\parallel,\perp}$, or for simplicity of notation A_{Born})(refer to Section 1.1). Instead, the measured asymmetries ($A_{\parallel,\perp}^{meas}$) created in chapter 3 contain many other physics processes beyond Born scattering. The radiative corrections account for the contributions from these other physics processes. In general, radiative corrections are classified into two categories: those effects that occur within the nuclear field of the scattering nucleon (Internal) and those effects that arise from the presence of other nuclei (External). In this experiment, because of the target geometry, the external radiative corrections are strongly dominated by bremsstrahlung radiation energy losses as the outgoing electrons traverse additional target material.

4.1   Internal Corrections

The internal radiative corrections account for what would have been measured if there were no external radiation. Assuming 100% polarization for both the ^{3}He target and the beam, and no unpolarized nucleons (i.e., dilution factor $= 1$), we define $\sigma^{\uparrow\uparrow}$ or $\sigma^{\downarrow\uparrow}$ as the total cross sections for the spin of the target nuclei and the incoming electron aligned or anti-aligned, respectively. These spin-dependent cross

sections can also be expressed in terms of polarized and unpolarized components as

$$\sigma^{\uparrow\uparrow} = \sigma^u - \sigma^p \quad ; \quad \sigma^{\downarrow\uparrow} = \sigma^u + \sigma^p, \tag{4.1}$$

where

$$\sigma^u \;\; = \;\; \text{unpolarized component},$$

$$\sigma^p \;\; = \;\; \text{polarized component}.$$

It follows that the longitudinal asymmetry defined in Eq. 1.5 can be written in terms of these cross sections

$$A_\parallel = \frac{\sigma^{\downarrow\uparrow} - \sigma^{\uparrow\uparrow}}{\sigma^{\downarrow\uparrow} + \sigma^{\uparrow\uparrow}} = \frac{\sigma^p}{\sigma^u}. \tag{4.2}$$

The internally radiated cross sections contain contributions from higher-order photon exchange processes including electron vertex and lepton and hadron vacuum polarization processes. In addition, cross sections from other processes contribute because of bremsstrahlung energy losses before and after scattering (see Fig. 4.1 for relative contributions from these processes). The internally radiated asymmetry is written as

$$A_{int} = \frac{\sigma^p_{int}}{\sigma^u_{int}} = \frac{\sigma^p_{Born}(1 + \delta_v) + \sigma^p_{el} + \sigma^p_{q} + \sigma^p_{in}}{\sigma^u_{Born}(1 + \delta_v) + \sigma^u_{el} + \sigma^u_{q} + \sigma^u_{in}}, \tag{4.3}$$

where

$$\delta_v \;\; = \;\; \text{vertex and vacuum polarization corrections},$$

$$\sigma_{el} \quad = \quad \text{elastic cross section contribution,}$$

$$\sigma_{q} \quad = \quad \text{quasi-elastic cross section contribution,}$$

$$\sigma_{in} \quad = \quad \text{inelastic cross section contribution from other kinematics.}$$
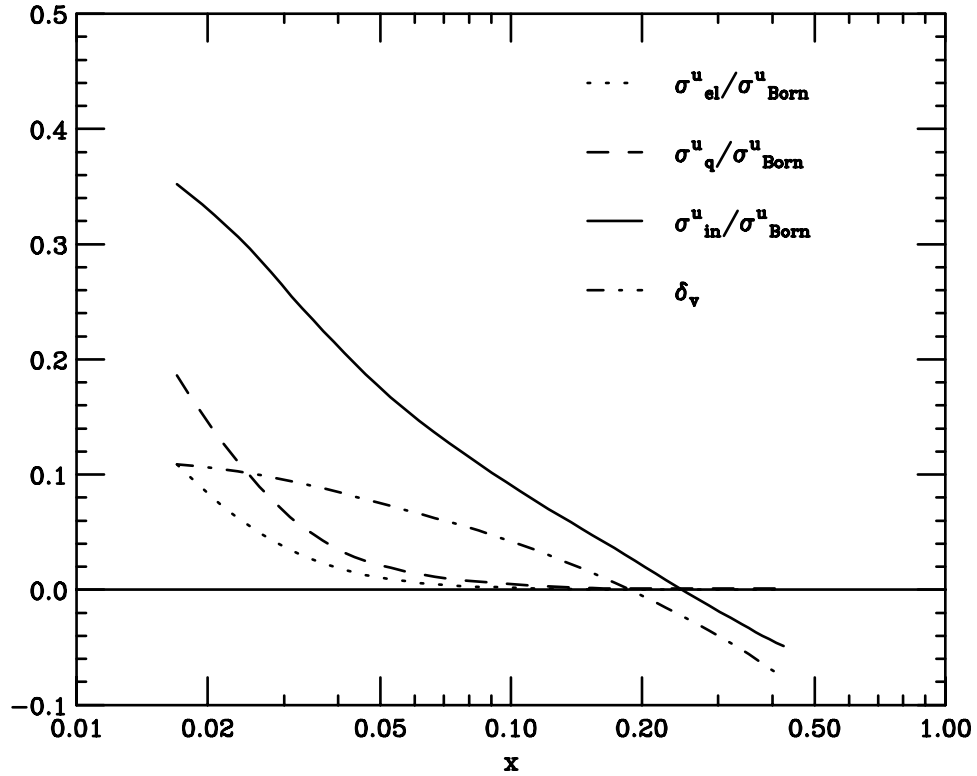
Figure 4.1: Component contributions to the internal radiative corrections. Each internal radiative processes (See Eq. 4.3) is normalized to the unpolarized Born cross section.

We define the additive internal radiative correction (ΔA_{int}^{RC}) to be the difference between this internally radiated asymmetry and the Born asymmetry:

$$\Delta A_{int}^{RC} = A_{Born} - A_{int}. \tag{4.4}$$

The code which has been used to calculate these additive radiative corrections (RCSLACPOL) was developed at SLAC by L. Stuart based on the paper by

Kukhto and Shumeiko [42, 43]. There also exists a similar code used at CERN called POLRAD[42, 44]. These codes use input models of Born cross sections to calculate the radiated cross sections used in Eq. 4.3. Using the same input models, the two codes were thoroughly cross checked and found to be consistent for each contributing piece to the radiative correction. The internal results of each code are compared in Fig. 4.2 and their difference is found to be negligible relative to the systematic uncertainty on the radiative corrections. Also shown on this plot are the internal results of RCSLACPOL run with the energy peaking approximation. In this approximation, it is assumed that the scattering electron can emit a bremsstrahlung photon before or after scattering, but not both. This assumption is reasonable since the probability for emitting a photon of significant energy both before and after scattering is known to be less than 1%. The peaking approximation allows for a significant increase in the speed of the code, typically running 20 times faster than POLRAD, which runs about 10 times faster than RCSLACPOL in exact mode. This increase in speed allows for far more thorough checking of systematic effects due to the input model choices (see Section 4.4). The final results were computed with the internal part of RCSLACPOL in exact mode, and the agreement between these different methods is very good. All of these codes require the best input models for nuclear electric and magnetic form factors, deep inelastic polarized and unpolarized structure functions, resonance region form factors, and ^{3}He nuclear models. A list of the input models used for the E154 calculation and error determination is contained in Appendix A.
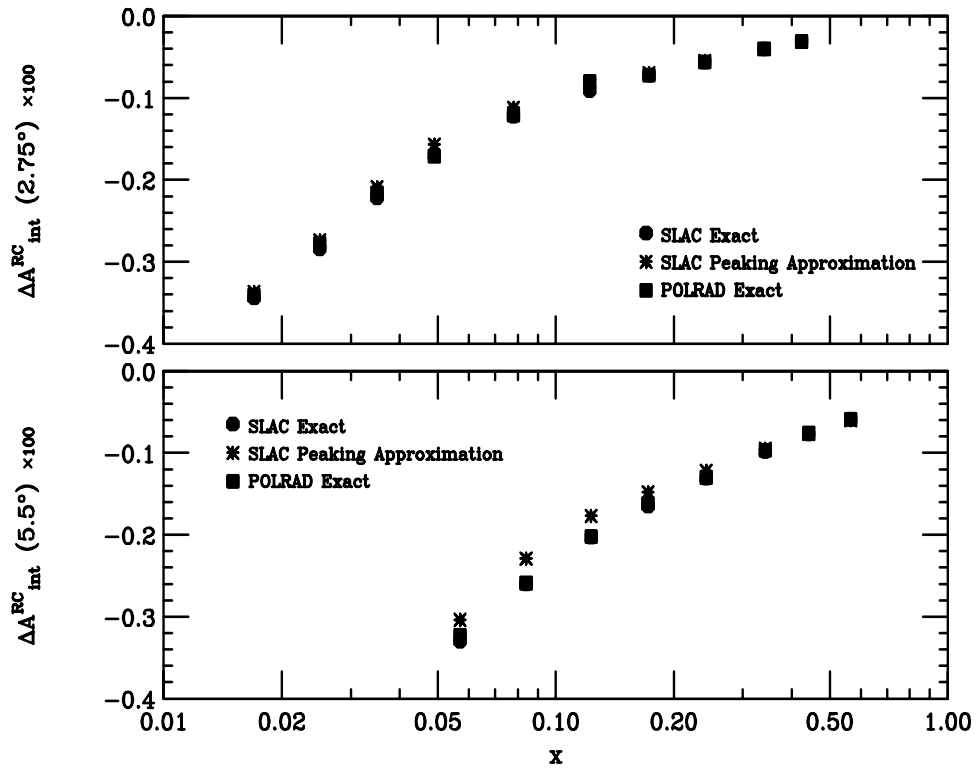
Figure 4.2: Comparison of additive internal radiative correction codes using the same input models. For the purpose of comparison, the systematic uncertainty on these radiative corrections at the lowest x point is greater than ± 0.1 (scaled by 100).

<u>4.2   External Corrections</u>

In this experiment the radiative corrections are dominated by the internal processes because of the small path length of the ^{3}He target. In the low-x bins where the corrections have the largest effect on the data, the external processes have less than a 5% effect relative to the overall correction (see Fig. 4.3). The external corrections account for the energy losses due to bremsstrahlung radiation as the electrons pass into and out of the target. In E154, the very thin end windows mean that there is a very small energy loss as the electrons enter the target. For the outgoing electrons, however, a significant fraction of them traverse some portion of the sidewalls of the target at a small angle.

2.75° Spectrometer			5.5° Spectrometer		
z (cm.)	t_{before}	t_{after}	z (cm.)	t_{before}	t_{after}
0 - 3	.00054	.14631	0 - 14	.00062	.07416
3 - 8	.00060	.19431	14 - 18	.00075	.09616
8 - 10	.00065	.04434	18 - 20	.00081	.04416
10 - 30	.00082	.00067	20 - 30	.00090	.00059

Table 4.1: Target model used in the radiative corrections. t_{before} and t_{after} refer to the average thickness of ^{3}He and glass, in radiation lengths, traversed by the detected electrons before and after the primary scattering process, respectively. z refers to the longitudinal position, along the beam line, of the primary scatter inside the target, measured from the front end window.

The target model used (see Table 4.1) was generated by R. Welsh and T. Smith [28], who took direct measurements of one of the target cells (Picard) and entered those values into a GEANT simulation. They found that the target could be adequately modeled using 4 target sections. Each section was represented by the average thicknesses of material, in radiation lengths, traversed by the electrons

before and after the scattering process (t_{before} and t_{after} respectively) based on the longitudinal position (z) along the beam line of the primary scatter inside the target. The radiative corrections are averaged over the target assuming that the counts from ^{3}He are evenly distributed along its length.
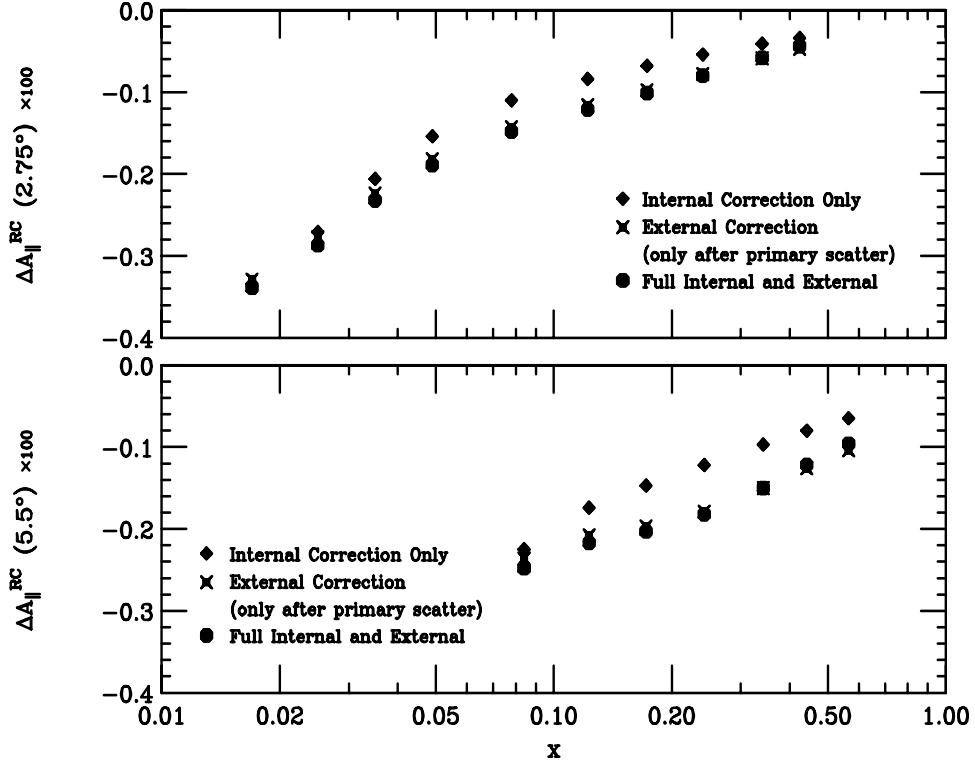
Figure 4.3: Comparison of internal and external radiative corrections to $A_{\parallel}$. Shown are the internal radiative corrections, internal corrections plus external corrections only for material after the initial scatter (i.e., front window thickness neglected), and the full internal and external corrections.

We let $I_b(E, E', t)$ be the probability that an electron of energy E will have an energy E' due to bremsstrahlung energy loss after traversing t radiation lengths of material [73, 61]. Then, the fully radiated cross sections are expressed as convolutions of the internally radiated cross sections (σ^p_{int} and σ^u_{int} from Eq. 4.3) with the

bremsstrahlung energy loss probabilities for traversing material before (t_{before}) and

after (t_{after}) the primary scatter [73, 61]:

$$\sigma_{rad}^{p(u)}(E_s, E_p) = \int_{E_s^{min}}^{E_s} \int_{E_p}^{E_p^{max}} I_{b(E_s,E_s',t_{before})} \, P_{d(E_s,E_s')} \, \sigma_{int}^{p(u)}(E_s',E_p') \, I_{b(E_p',E_p,t_{after})} \, dE_p' dE_s'.$$

$$(4.5)$$

Here, E_s and E_p are the incident and detected electron energies, and E_s^{min} and

E_p^{max} are the kinematic boundaries defined by elastic scattering. $P_d(E_s, E_s')$ is the

electron depolarization correction [62] due to the radiation of a photon of energy

$E_\gamma = E_s - E_s'$. Note, P_d only affects the polarization dependent case (σ_{rad}^p). These

fully radiated cross sections, along with the Born cross sections, form the additive

radiative correction:

$$\Delta A^{RC} = A_{Born} - A_{rad} = \frac{\sigma_{Born}^p}{\sigma_{Born}^u} - \frac{\sigma_{rad}^p}{\sigma_{rad}^u}. \qquad (4.6)$$

Since A_{Born} is unknown, we have to create an input model for the radiative

corrections. The best model we have is a fit to the measured data from E154. The

validity of this model can be tested by comparing the calculated radiated asymmetry

with the experimentally measured asymmetry (A^{meas}). Then, from Eq. 4.6, we

would expect

$$A_{Born} = A^{meas} + \Delta A^{RC}. \qquad (4.7)$$

If the input model for A_{Born} is not equal to the radiatively corrected data ($A^{meas} +$

ΔA^{RC}), then we make a new fit to the corrected data and use it as a new input model for A_{Born}. This procedure is then iterated until convergence between the input model and the corrected data is achieved . Convergence is defined to be a less than 1% difference, for each fit parameter, between the input model and the fit to the corrected data. Convergence usually requires between three and five iterations, depending on the number of parameters used in the fit.

4.3   Statistical Errors in Radiative Corrections

The additive radiative correction defined in Eq. 4.6 and used in Eq. 4.7 adequately corrects the asymmetry for polarized and unpolarized radiative processes. However, this method is not adequate for the correct propagation of statistical errors. The statistical uncertainty on the asymmetry measurement is directly related to the number of counts recorded. Referring to Eq. 4.2, we see that the the total number of counts is governed by the unpolarized cross section σ^u. Therefore the statistical uncertainty on the radiated asymmetry that we measure A^{meas} is directly related to the radiated unpolarized cross section σ^u_{rad}. To assign a statistical uncertainty to our measurement of A_{Born}, we need to extract σ^u_{Born}. To do this we define a radiative dilution factor (f_{rc})

$$f_{rc} = \frac{\sigma^u_{rad} - \sigma^u_{tail}}{\sigma^u_{rad}}, \tag{4.8}$$

where σ^u_{tail} refers to the additional unpolarized radiated events beyond σ^u_{Born}. If we consider the internal radiative corrections only, we can see from Eq. 4.3 that we could express $\sigma^u_{tail} = \delta_v \sigma^u_{Born} + \sigma^u_{el} + \sigma^u_q + \sigma^u_{in}$. Using Eq. 4.8, we can re-write Eq. 4.6

such that

$$A_{Born} = \frac{A_{rad}}{f_{rc}} + \delta A_{rc} \qquad (4.9)$$

where the previously calculated ΔA^{RC} can be related to δA_{rc} as

$$\Delta A^{RC} = \left(\frac{1}{f_{rc}} - 1 \right) A_{rad} + \delta A_{rc}. \qquad (4.10)$$

Substituting the measured asymmetry A^{meas} for A_{rad} in Eq. 4.9, we see that the statistical uncertainty on A^{meas} will be appropriately scaled to yield an error for A_{Born}.

It should be noted that the definition of σ^u_{tail} used in Eq. 4.8 is non-trivial. The unpolarized tail will definitely contain all elastic and quasi-elastic counts. In addition, unpolarized deep inelastic events radiating down from higher values of x must also be included. A strict definition of the unpolarized DIS tail would require that, for a given x-bin, all DIS counts radiating down from outside of that bin must be considered part of the tail and subtracted off. However, it can be argued that this strict definition of the DIS tail may not be necessary. It is known that most of the radiated background counts are coming from closely neighboring bins. Since the cross section varies smoothly from bin-to-bin and the variation is not large, to a first approximation, the number of events lost from a given bin to the lower adjacent bin is equivalent to the number of events gained from the upper adjacent bin. To remove these background counts would be wasteful because they are still good DIS events. Not removing these background counts is comparable to shifting the bin slightly higher in x.

Studies were done to determine the affect that different definitions of the unpolarized DIS tail would have on the radiative dilution factor f_{rc}. The DIS tail was defined to include all unpolarized DIS counts originating from a value of x greater than some cutoff. The affect on f_{rc} was then studied by using various cutoff values ranging from the upper edge of the x-bin under evaluation to the upper edge of the highest x bin in the measured region (see Table 4.2). The final choice of cutoff

2.75° Spectrometer					5.5° Spectrometer				
x	A	B	C	D	x	A	B	C	D
.017	2.077	1.856	1.686	1.188	–	–	–	–	–
.025	1.766	1.650	1.500	1.109	–	–	–	–	–
.035	1.680	1.501	1.334	1.067	–	–	–	–	–
.049	1.497	1.344	1.216	1.040	.057	1.961	1.464	1.319	1.065
.078	1.351	1.251	1.154	1.024	.084	1.461	1.314	1.202	1.033
.122	1.305	1.217	1.113	1.019	.123	1.325	1.232	1.123	1.015
.173	1.296	1.168	1.068	1.020	.172	1.302	1.164	1.066	1.008
.240	1.168	1.106	1.049	1.026	.242	1.170	1.101	1.039	1.005
.340	1.144	1.107	1.048	1.048	.342	1.151	1.085	1.022	1.006
.424	1.102	1.102	1.102	1.102	.442	1.128	1.049	1.009	1.009
–	–	–	–	–	.565	1.028	1.028	1.028	1.028

Table 4.2: A study of the radiative dilution factor $(1/f_{rc})$ for different cutoffs. For a n-th x-bin, the cutoffs are defined as follows: A - the upper edge of the same bin; B - the average x value of the next bin $(n + 1)$; C - the average x value of the $(n + 2)$-th bin; D - the upper edge of the highest x-bin. The final results used Cutoff C.

was somewhat arbitrary. Motivated by the smoothness arguments discussed above and agreement with an alternative unfolding method [63], it was chosen to place the cutoff for the n-th x bin at the average x value of the $(n + 2)$-th bin or the upper edge of the highest x bin, whichever was lower.

4.4   Systematic Errors in Radiative Corrections

The systematic error should adequately describe our lack of knowledge of the true physics processes, i.e., our uncertainty in the input models. Appendix A lists the 7 major sections of input models, and the models that were considered reasonable for each section. To construct the error for a given section, the radiative corrections code was run under nominal conditions and then with each of the listed models substituted for the nominal. The largest deviation at each x-bin was then found for each section of models, and assigned to be the systematic error. The errors from each section of models were treated as independent and added in quadrature to create the overall systematic error.

In addition to the sections of models listed in appendix A, the thicknesses in the target model were varied by $\pm 5\%$ to account for the different targets actually used in E154, and certain parameters of the code, like integration parameters, were varied to insure no major dependence. Each of these was considered as a separate section, and its maximum deviation was also added in quadrature for the final result.

In order to estimate the error on the integral of g_1 in the measured region, it was necessary to account for any point-to-point correlations in the radiative corrections systematic errors. This was done by determining an integral error due to the radiative correction for each variation of the models. In other words, for each model substitution mentioned above, radiative correction values for both $A_\parallel$ and $A_\perp$ were obtained. These were then combined with the correct kinematic factors to create an

effective radiative correction for g_1. Assuming g_1/F_1 independent of Q^2, the data from the two spectrometers were combined and the data evolved to $Q^2 = 5$. This was then integrated over the measured region. The difference of this integral from the nominal configuration was then computed. As before, the maximum deviation of the integral for each model category was assigned to be the error on the integral for that section. These errors were then added in quadrature to create the total radiative corrections error for the measured integral.

4.5   Radiative Corrections Summary

The final values of the radiative corrections are given in tables 4.3, 4.4 and B.6. To obtain the final results for the central values listed, the internal portion of RCSLACPOL was run in exact mode. The systematic errors were constructed by the procedure listed above, using RCSLACPOL with the energy peaking approximation.

When viewed relative to the actual $A_\parallel$ and $A_\perp$ data (see Fig. 4.4), the systematic errors on the radiative corrections are consistently less than the statistical errors on the data. At worst, on the lowest x-point, the radiative correction systematic error is less than one third of the magnitude of the statistical error on the data. For the perpendicular data ($A_\perp$), the lack of statistics far outweighs any effect of the systematic error contributions from the radiative corrections.

The individual model component contributions to these systematic errors are listed in Tables B.2-B.5. For the parallel radiative corrections errors, our lack

x-bin	$1/f_{rc}$	$\Delta A_\parallel^{RC}$	Sys Error	$\Delta A_\perp^{RC}$	Sys. Error
0.017	1.686	-.341	0.132	0.024	0.151
0.025	1.500	-.285	0.088	0.014	0.118
0.035	1.334	-.233	0.055	0.004	0.089
0.049	1.216	-.192	0.034	-.004	0.101
0.078	1.154	-.151	0.021	-.009	0.111
0.122	1.113	-.122	0.042	-.008	0.197
0.173	1.068	-.099	0.058	-.004	0.220
0.240	1.049	-.081	0.062	0.002	0.181
0.340	1.048	-.061	0.048	0.008	0.074
0.424	1.102	-.051	0.034	0.012	0.024

Table 4.3: Radiative corrections and errors for the 2.75° spectrometer. All values are in units of 10^{-2}. The radiative dilution factor f_{rc} (see Sec. 4.3) was the same for both $A_\parallel$ and $A_\perp$. Notice that the additive correction and systematic errors are implemented as in Eq. 4.7.

x-bin	$1/f_{rc}$	$\Delta A_\parallel^{RC}$	Sys Error	$\Delta A_\perp^{RC}$	Sys. Error
0.057	1.319	-.290	0.093	0.018	0.065
0.084	1.202	-.251	0.050	0.001	0.108
0.123	1.123	-.227	0.078	-.007	0.236
0.172	1.066	-.210	0.109	-.006	0.315
0.242	1.039	-.185	0.122	0.001	0.312
0.342	1.022	-.152	0.106	0.011	0.168
0.442	1.009	-.123	0.095	0.019	0.053
0.565	1.028	-.102	0.116	0.025	0.323

Table 4.4: Radiative corrections and errors for the 5.5° spectrometer. All values are in units of 10^{-2}. The radiative dilution factor f_{rc} (see Sec. 4.3) was the same for both $A_\parallel$ and $A_\perp$. Notice that the additive correction and systematic errors are implemented as in Eq. 4.7.
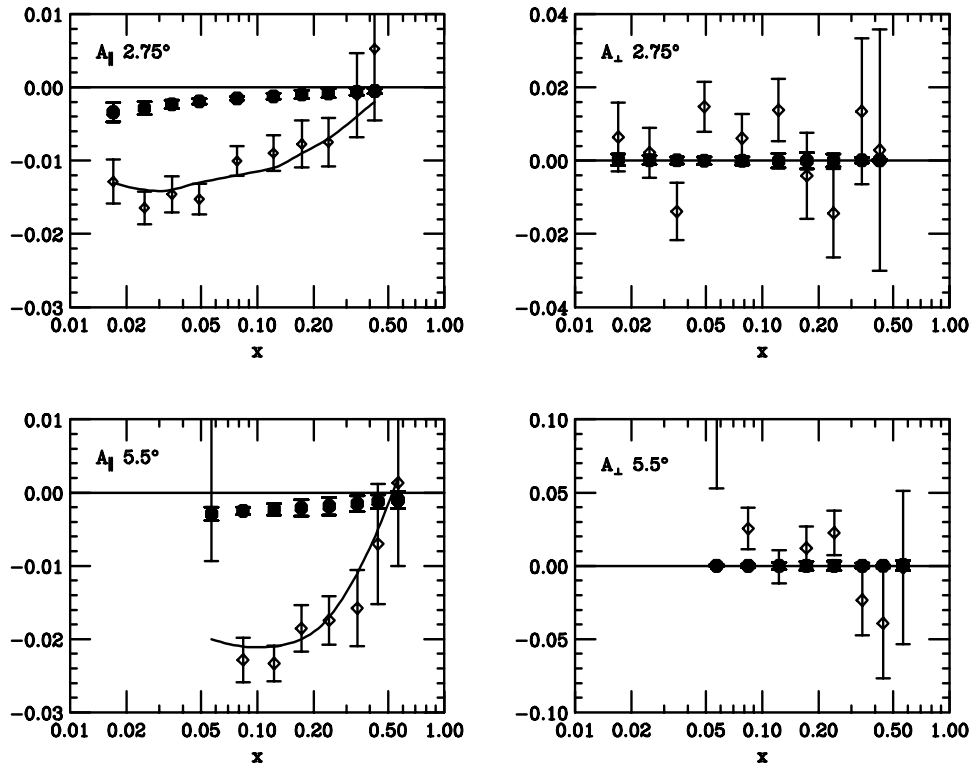
Figure 4.4: Comparison of $A_\parallel$ and $A_\perp$ data to the applied additive radiative corrections. On each plot, $\diamond$ refers to the corrected data (errors shown are statistical only) while $\bullet$ refers to the additive radiative correction that was applied (the radiative correction errors shown are systematic). For the $A_\parallel$ data, the line shows the Born model used in the radiative correction calculation. For the $A_\perp$ data, the Born model is indistinguishable from zero.

of knowledge of the behavior of A_1 near $x = 1$ means that the error due to the distribution of A_1 models is consistently one of the largest components, becoming dominant at low-x where the error due to A_1 contributes a factor of three more than any other component.

Since one of the big concerns in this experiment is the data at low x values, many tests were done to see if any of these components of the radiative corrections could have a significant effect on the shape of the data. We feel confident that the errors presented adequately describe any such possible effects.

The systematic error contributions to the measured integral are presented in Table B.6. While the A_1 models are still the largest component of the error, both the DIS unpolarized structure functions and the g_2 uncertainty contributions have comparable magnitudes. This is partially due to the fact that most of the integral comes from the higher x regions, where the errors from these two components are comparable with A_1. In addition, the errors due to A_1 are highly correlated point-to-point so a particular model may add significantly to the integral at low-x, but then subtract from the integral at high-x. Therefore the overall effect on the integral is much smaller than it would be if this were not done correctly. The final systematic error on the measured integral of g_1 due to the radiative corrections was found to be ± 0.001292. Overall, the total error to the integral would be almost a factor of two larger if these point-to-point correlations were not correctly taken into account.

CHAPTER 5

RESULTS

5.1   Measured Asymmetries

For E154, two separate analyses were performed. The one based at SLAC proceeded as described above. In addition, an alternative analysis was performed at California Institute of Technology (CIT) as a cross check. The CIT analysis involved a completely separate clustering algorithm for the shower counter and some slightly different tracking code. The two analyses agreed within statistical errors. All results from E154 presented either in this dissertation or in publications are based on an average of the asymmetry results from the two analyses. In addition, the averaged asymmetries were used to make the input models for the radiative corrections calculations presented in the previous chapter.

Statistical errors were created using simple counting statistics for the measured asymmetries. These were then propagated through the equations listed in Chapter 3 and Section 4.3.

In addition to the systematic error study discussed in section 4.4, similar studies were performed on contributions to systematic errors from the other major components of the experiment. Since the error on the g_2 measurement is dominated by the statistical error, a detailed examination of the systematic errors is not

presented in this work. A full analysis of the systematic errors from E154 can be found in references [64, 65]. For this dissertation, the individual contributions to the systematic errors on g_2 are listed in table B.1.

x bin	$\langle x \rangle$	$\langle Q^2 \rangle$	$A_\parallel$	$\delta A_\parallel$ stat	$\delta A_\parallel$ sys	$A_\perp$	$\delta A_\perp$ stat	$\delta A_\perp$ sys
2.75° spectrometer								
0.014 - 0.02	0.017	1.21	-0.0133	0.0041	0.0036	0.0058	0.0126	0.0018
0.02 - 0.03	0.025	1.59	-0.0169	0.0030	0.0025	0.0000	0.0094	0.0013
0.03 - 0.04	0.035	2.05	-0.0154	0.0031	0.0018	-0.0163	0.0100	0.0018
0.04 - 0.06	0.049	2.57	-0.0143	0.0025	0.0012	0.0144	0.0080	0.0015
0.06 - 0.10	0.078	3.32	-0.0103	0.0023	0.0009	0.0072	0.0075	0.0013
0.10 - 0.15	0.122	4.09	-0.0085	0.0027	0.0007	0.0120	0.0095	0.0022
0.15 - 0.20	0.173	4.63	-0.0089	0.0034	0.0008	-0.0014	0.0125	0.0022
0.20 - 0.30	0.241	5.09	-0.0080	0.0034	0.0007	-0.0121	0.0127	0.0021
0.30 - 0.40	0.340	5.51	-0.0022	0.0060	0.0005	0.0247	0.0210	0.0035
0.40 - 0.50	0.423	5.82	0.0044	0.0137	0.0007	0.0036	0.0443	0.0007
5.5° spectrometer								
0.04 - 0.06	0.057	4.03	0.0120	0.0260	0.0027	0.1582	0.1219	0.0146
0.06 - 0.10	0.084	5.47	-0.0224	0.0035	0.0022	0.0274	0.0165	0.0025
0.10 - 0.15	0.123	7.23	-0.0226	0.0027	0.0018	0.0023	0.0126	0.0025
0.15 - 0.20	0.172	8.94	-0.0168	0.0034	0.0013	0.0082	0.0157	0.0033
0.20 - 0.30	0.242	10.71	-0.0168	0.0034	0.0013	0.0182	0.0158	0.0035
0.30 - 0.40	0.342	12.55	-0.0123	0.0053	0.0019	-0.0171	0.0246	0.0024
0.40 - 0.50	0.442	13.83	-0.0102	0.0084	0.0012	-0.0245	0.0383	0.0020
0.50 - 0.70	0.564	15.00	0.0003	0.0119	0.0008	-0.0024	0.0548	0.0034

Table 5.1: Final Asymmetry results for ^{3}He . These are the measured asymmetries on ^{3}He from E154 with all corrections applied (See Secs. 3.2,3.3).

5.2   Physics Results

The corrected asymmetries listed above were combined to produce values for $g_2^n(x, Q^2)$ and $A_2^n(x, Q^2)$, using the equations developed in Secs. 1.1 and 1.2 and the method discussed in Sec. 2.1.2 to extract the neutron from ^{3}He . The values are listed in Table 5.2.

$\langle x \rangle$	$\langle Q^2 \rangle$	g_2^n	δg_2^n stat	δg_2^n sys	A_2^n	δA_2^n stat	δA_2^n sys
2.75° spectrometer
0.017	1.21	7.167	15.312	2.169	0.033	0.074	0.010
0.025	1.59	0.154	7.232	0.980	-0.002	0.056	0.007
0.035	2.05	-7.870	4.890	0.958	-0.106	0.064	0.013
0.049	2.57	4.605	2.504	0.543	0.099	0.056	0.012
0.078	3.32	1.318	1.331	0.245	0.058	0.065	0.012
0.122	4.09	1.223	0.953	0.237	0.127	0.106	0.026
0.173	4.63	-0.080	0.810	0.145	-0.033	0.179	0.033
0.241	5.09	-0.486	0.515	0.105	-0.251	0.241	0.049
0.340	5.51	0.541	0.466	0.145	0.635	0.550	0.126
0.423	5.82	0.040	0.580	0.018	0.162	1.414	0.040
5.5° spectrometer
0.057	4.03	41.007	31.640	4.458	0.945	0.727	0.103
0.084	5.47	4.077	2.403	0.434	0.161	0.099	0.018
0.123	7.23	0.231	1.003	0.196	0.009	0.080	0.016
0.172	8.94	0.398	0.723	0.153	0.052	0.112	0.024
0.242	10.71	0.477	0.407	0.098	0.145	0.136	0.031
0.342	12.55	-0.216	0.311	0.039	-0.205	0.273	0.032
0.442	13.83	-0.155	0.239	0.030	-0.360	0.532	0.047
0.564	15.00	-0.008	0.132	0.009	-0.036	0.953	0.058

Table 5.2: Final neutron results for g_2 and A_2. The asymmetry data from Table 5.1 were used to compute g_2 and A_2 for ^{3}He (see Eqs. 1.7,1.16). Then the neutron results (shown) were extracted as in Sec. 2.1.2.

5.2.1 A_2 Results

The results for $A_2^n(x, Q^2)$ are plotted in Fig. 5.1. Also shown are the bound-aries of the positivity constraint (defined in Sec. 1.3.5) calculated for the kinematics of each spectrometer. It can be seen that the positivity constraint is easily satisfied. In fact, the measurement shows that $A_2^n(x, Q^2)$ is consistent with zero.
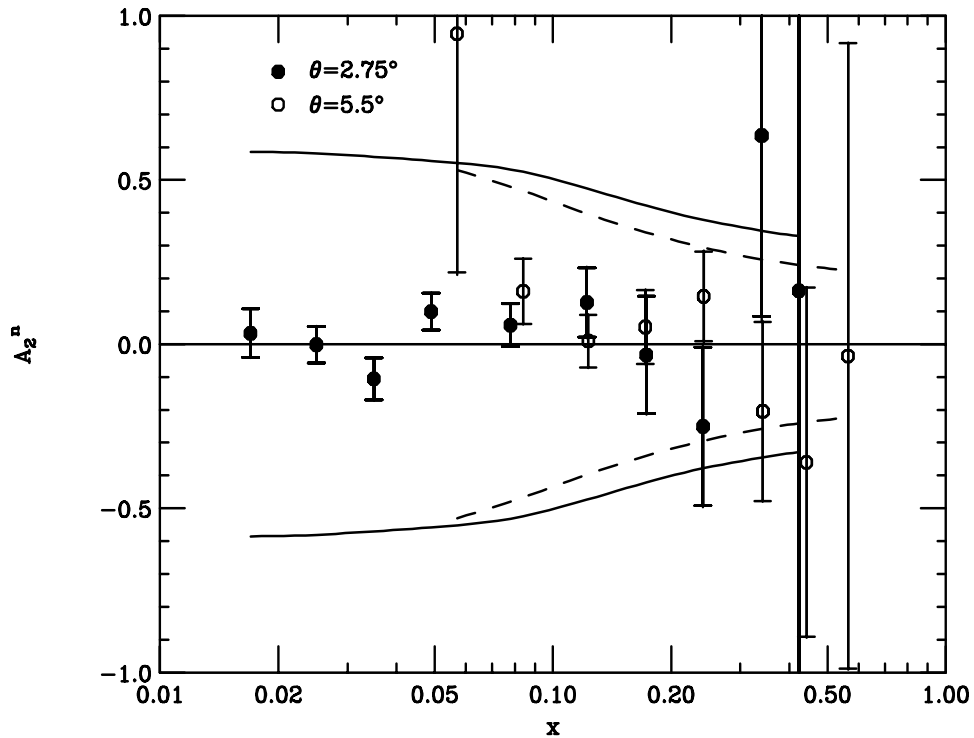
Figure 5.1: The results for A_2^n from E154. The data are plotted for both spectrometers with combined statistical and systematic errors. The overall errors are dominated by the statistical which correspond to the tick marks plotted on the error bars. The data are compared to the predicted positivity constraint $|A_2| \leq \sqrt{R}$ for the kinematics of the 2.75° spectrometer (solid line) and 5.5° spectrometer (dashed line).

5.2.2 g_2 Results

The results for $xg_2^n(x, Q^2)$ are shown in Fig. 5.2. Plot (a) shows the results for each spectrometer individually. No significant Q^2-dependence was seen in the measured data, so the data from the two spectrometers were averaged, assuming no

Q^2 evolution, for a combined result shown in plot (b). Also shown on these plots are the twist-2 predictions for xg_2^{WW} calculated at the kinematics of the averaged data. To calculate g_2^{WW}, a fit to the measured g_1^n data was used assuming that g_1/F_1 was independent of Q^2. The E154 data are consistent with the calculation of g_2^{WW} with a χ^2 in the measured range of 17.6 for 11 degrees of freedom.
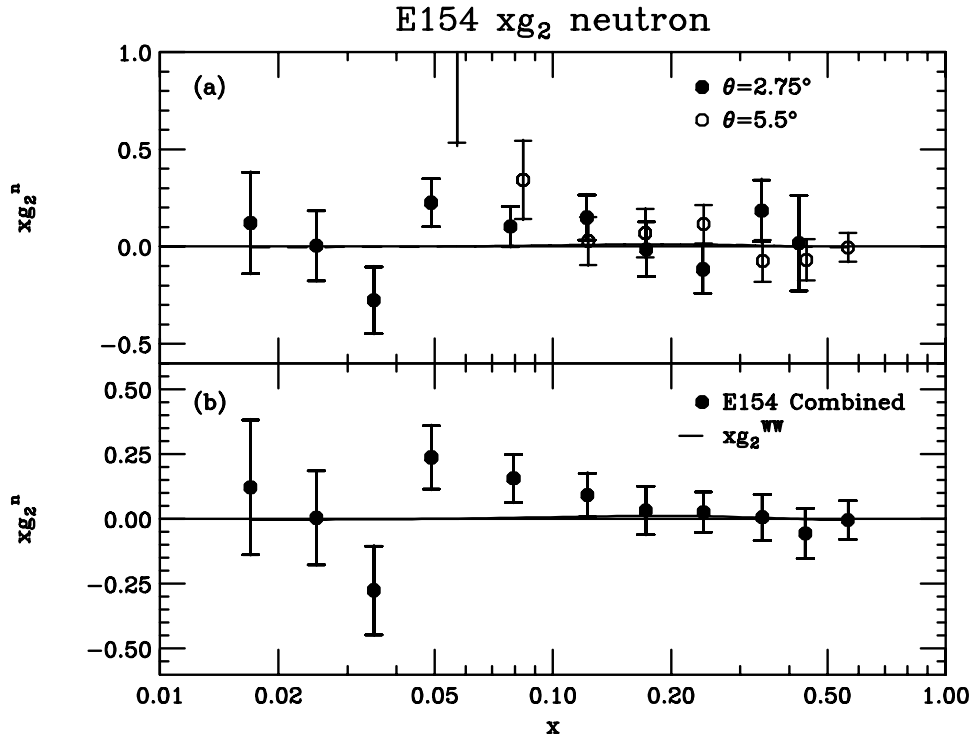
Figure 5.2: The xg_2 results from E154. (a) shows the data for each spectrometer. (b) shows the data when the spectrometer data have been averaged. Also shown on each plot is the calculated twist-2 function xg_2^{WW} which is very close to zero on this scale. The errors are plotted in the same manner as Fig. 5.1

However, the data do not rule out the possibility of large twist-3 contributions. In Fig. 5.3, we show data for $\overline{g_2}(x, Q^2) = g_2(x, Q^2) - g_2^{WW}(x, Q^2)$. While these data are consistent with zero, there is also a possible hint of structure in the middle x region.

All of the xg_2^n data from the three SLAC experiments (E142, E143, and E154)
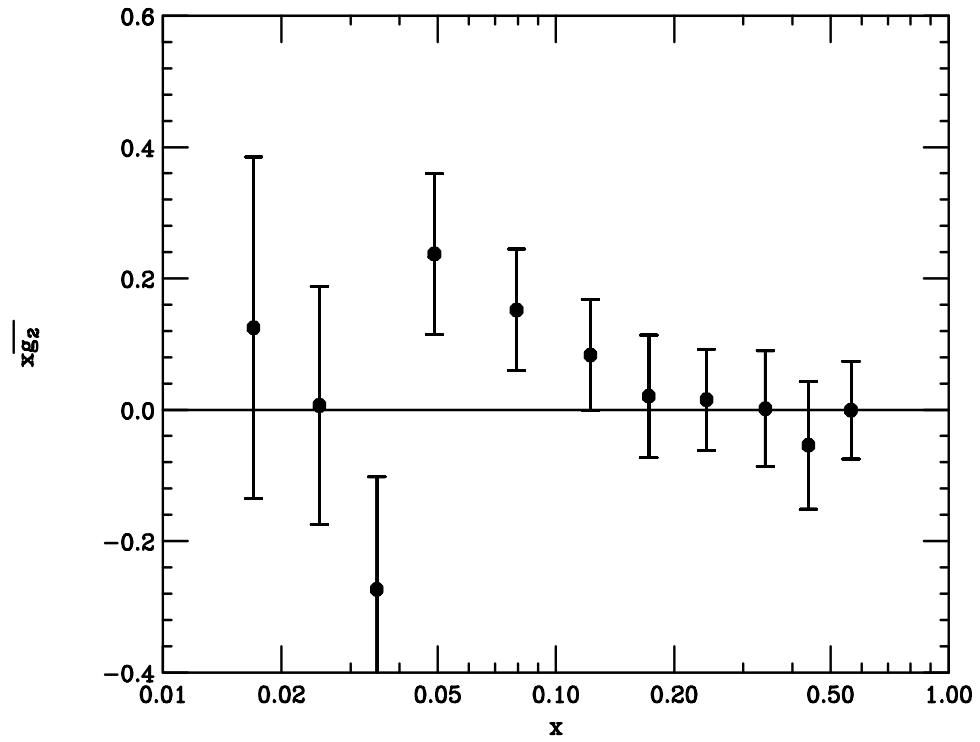
Figure 5.3: Values of $\overline{g_2}$ from E154 for 2.75° and 5.5° averaged together. The data are consistent with no twist-3 contribution, however values as large as 0.2 are allowed in the mid-x range. Errors shown are statistical only.

are shown in Fig. 5.4. For each experiment, the data from the two spectrometers
were averaged. All data sets are consistent with each other and with zero.
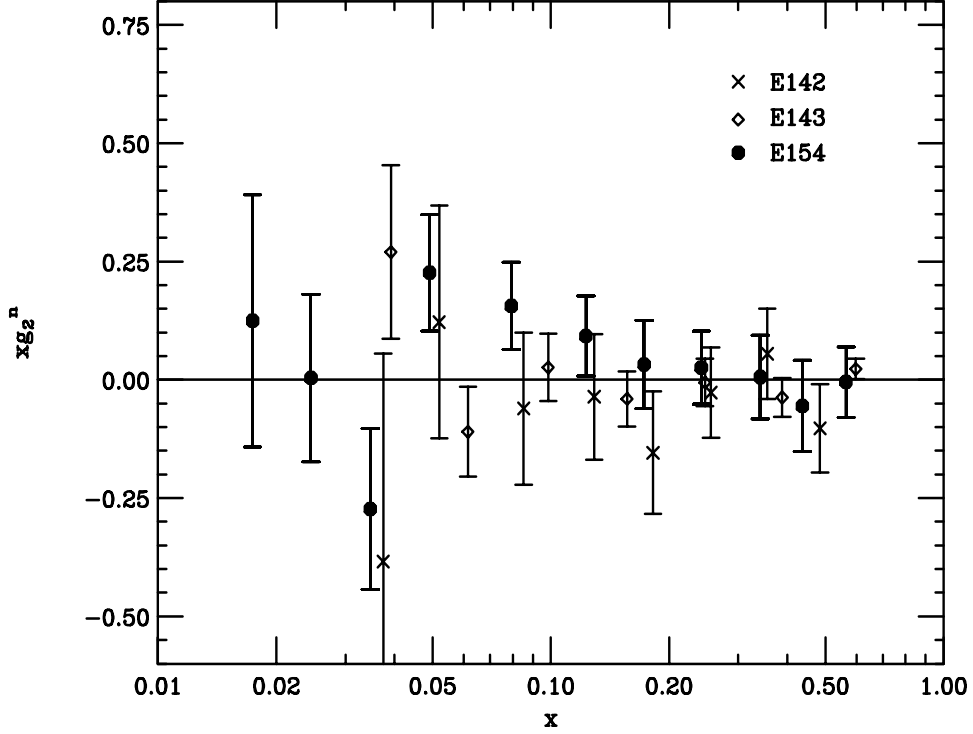
Figure 5.4: Total SLAC data for xg_2^n. Data for xg_2^n from E142, E143, and E154 are all
plotted together. For each experiment the two spectrometers were averaged assuming no
Q^2 dependence. All data sets are consistent with each other and with zero.

We can also compare the integral of g_2 over the measured region with the
Burkhardt-Cottingham prediction (Eq 1.26). As mentioned in Sec 1.3.4, our lack of
knowledge on the extrapolation of g_2 to $x = 0$ prevents us from offering a complete
test of the Burkhardt-Cottingham Sum Rule. To extrapolate to $x = 1$ we assumed
$g_2 \propto (1 - x)^3$, which is consistent with the twist-2 prediction that $g_2^{WW} \approx -g_1$ at
high x. Then, integrating the data at the measured kinematics, we find that

$$\int_{0.014}^{1} g_2^n(x)dx = 0.19 \pm 0.17(stat) \pm 0.02(syst). \tag{5.1}$$

at an average experimental Q^2 of 3.6 $(\text{GeV/c})^2$. The errors include the uncertainty from the high x extrapolation which did not contribute significantly to the integral.

5.2.3 d_2 Results

In addition to the preceding analysis, we can look for further evidence of twist-3 contributions by constructing the matrix elements described in Sec. 1.3.3. Specifically, the best one to test against existing theoretical predictions is the first twist-3 matrix element d_2 as defined in Eq. 1.24. This requires integrating the second moment of g_1^n and g_2^n over the range from $0 \leq x \leq 1$. Unfortunately the measurement does not cover the entire range of x. It is expected that this will not adversely affect the measurement of these moments since the contribution from low x will be reduced by x^2 and the behavior of g_1 and g_2 at high x are both expected to fall as $(1-x)^3$. In addition it is argued [67] that the integrand of Eq. 1.24 is strictly twist-3 and will therefore have a $(1-x)^2$ behavior. Using the $(1-x)^2$ function, normalized to the high x data, to extrapolate the high x contribution and neglecting the low x contribution, we can integrate Eq. 1.24 at the measured kinematics to present a value for d_2^n from E154 with an average Q^2 of 3.6 $(\text{GeV/c})^2$:

$$d_2^n = -0.004 \pm 0.038(stat) \pm 0.005(syst). \tag{5.2}$$

In addition to the data from E154, a value for d_2^n can also be extracted from the previous SLAC experiments E143 and E142. Since these measurements are all statistically limited, it is useful to examine a combined average for all SLAC data. Table 5.3 shows the value for d_2^n using all the SLAC data. In addition, many theo-

	$d_2^n \times 10^2$	Q^2 (GeV/c)^2
E154 result	-0.4 ± 3.8	3.6
SLAC Average	-1.0 ± 1.5	3.0
Bag Model [10]	0.253	5.0
Bag Model [8]	0.03	5.0
QCD Sum Rule [16]	-3 ± 1	1.0
QCD Sum Rule [14]	-2.7 ± 1.2	1.0
Lattice QCD [18]	-0.39 ± 0.27	4.0

Table 5.3: Comparison of experimental and theoretical results for the twist-3 matrix element d_2^n. The theoretical predictions are discussed in more length in Secs. 1.3.2 and 1.3.3.

retical predictions are shown. With the current experimental precision, we cannot rule out any of the theoretical models, but it is interesting to note that the QCD sum rules appear to have the worst agreement with the data.

CHAPTER 6

CONCLUSIONS

In this dissertation, the conceptual basis of the transverse structure function g_2 has been presented and its interpretation under QCD. It has been demonstrated that measurements of this quantity can yield significant insight into our understanding of QCD, one of the foundations of our current understanding of the universe. In addition, this dissertation has presented the results of a new measurement of $A_2^n(x, Q^2)$ and $g_2^n(x, Q^2)$ in the kinematic range $0.14 \leq x \leq 0.7$ and $1.0 \leq Q^2 \leq 17.0$ $(\text{GeV/c})^2$. These data have been compared with the current best theoretical predictions.

The A_2^n data are clearly smaller than the $\sqrt{R}$ positivity limit, thus offering a better constraint for future experiments. The data for g_2^n are generally consistent with the twist-2 g_2^{WW} prediction and with zero. However, significant twist-3 contributions are not ruled out. In addition, the theoretically calculable quantity d_2^n has been extracted from these data. It is consistent with all theoretical predictions.

In general, the data are not sufficient to distinguish between different theoretical models. There are two significant conclusions that can be drawn from these data. First, the data show that for the neutron, A_2, g_2, and d_2 all fall within expected ranges. Second, the measured data have demonstrated that current experimental

capabilities are adequate for extracting useful tests of QCD. A future experiment has already been proposed and approved to run at SLAC for a dedicated measurement of $g_2(x, Q^2)$ on proton and deuteron targets [66]. This experiment will finally gain sufficient statistical precision to distinguish the theoretical predictions for d_2 at the two or three sigma level. In addition, the statistical precision will be sufficient to resolve g_2^{WW} from zero at about five or six sigma.

With the addition of this next experiment, scheduled to run in the spring of 1999, the statistical precision will finally allow experimental data to test some very fundamental predictions of QCD.

APPENDIX A

INPUT MODELS FOR RADIATIVE CORRECTIONS

The radiative corrections depend heavily on the choice of input models. Therefore the errors on the radiative corrections reflect the quality of the input models used. In order to minimize the systematic errors for E154, models were carefully evaluated based on their consistency with existing data and current theoretical constraints where data was not available. The following list contains those models chosen for this calculation. In each section, the first model listed is considered the nominal configuration.

1. **Proton and neutron elastic form factors**

   (for calculating σ_q^p and σ_q^u, see Eq. 4.3)

   There exist many different models for the electric and magnetic form factors of the proton and neutron. L. Stuart and J. Fellbaum have carefully chosen a set of five models which are representative of the worlds data. These are then combined using (for unpolarized) $^3\text{He} = 2p + n$ or (for polarized) $^3\text{He} = n$ and multiplied by the Pauli suppression factor (see below) to get the quasi-elastic form factors.

   (a) G_M^p and G_M^n calculated with the dipole form factor model:

(μ_p and μ_n are the proton and neutron magnetic moments, respectively)

$$\frac{G_M^p(Q^2)}{\mu_p} = \frac{G_M^n(Q^2)}{\mu_n} = \frac{1}{(1 + Q^2/(.71)^2)^2},$$

G_E^p described by Gari and Krümpelmann [45],

$G_E^n = 0.0;$

(b) G_M^p and G_E^n taken from fit 8.2 of Höhler [46],

   G_E^p taken from IJL 5 parameter fit [48],

   G_M^n from Korner and Kuroda [47] ;

(c) G_M^p and G_E^p taken from fit 5.3 of Höhler [46],

   G_E^n taken from fit 8.2 of Höhler [46],

   G_M^n from a fit to NE11 data [49] ;

(d) G_M^p, G_M^n and G_E^p taken from Gari and Krümpelmann [45],

   G_E^n described by Galster [50];

(e) G_M^p calculated with the dipole model,

   G_E^p taken from IJL 5 parameter fit [48],

   G_M^n and G_E^n from Blatnik and Zovko's [51].

2. **Pauli Suppression models for quasi-elastic scattering**

(for calculating σ_q^p and σ_q^u, see Eq. 4.3)

(a) Tsai [73],

(b) Stein [52],

(c) DeForest and Walecka [53],

(d) Van Orden [54],

(e) No Pauli suppression.

3. ^{3}**He Elastic Form Factor**

(for calculating σ_{el}^p and σ_{el}^u, see Eq. 4.3)

At low Q^2, elastic and magnetic form factors are computed by a fit to data from McCarthy, et al. [58]. At high Q^2, the charge form factor is computed from a parameterization by Arnold, et al. [59]. This parameterization calculates a measured combination of the charge and magnetic form factors. Since the magnetic form factor is small, it is assumed reasonable to extrapolate the low Q^2 fit into the high Q^2 region.

4. **Deep inelastic and resonance region unpolarized structure functions**

(For calculating σ_{in}^u, see Eq. 4.3)

The spin independent deep inelastic structure functions are evaluated as

$$F_2^n = 2F_2^D - F_2^p,$$

$$F_2^{^3He} = 2F_2^D + F_2^p,$$

where F_2^D is per nucleon and $F_2^{^3He}$ is the total nuclear structure function.

(a) Inelastic

    i. F2NMC [1] and R1990 [2],

ii. F2GLOB [55] and R1990 [2];

(b) Resonance Region

    i. Bodek parameterization [56],

    ii. H2MODEL: Proton global resonance data fit by L. Stuart [57],

    iii. Extrapolated deep-inelastic structure function (F2GLOB).

5. **Deep inelastic longitudinal polarized structure functions**

(for calculating σ_{in}^{p}, see Eq. 4.3)

g_1^n is calculated from fits to A_1^n data from E154 and a model for g_2^n (see Sec. 6). This method is preferred because fits to the g_1 data were frequently found to violate physical constraints in the unmeasured regions. Fits to the A_1 data are much more robust. All fits were iterated until they converged. The nominal "best fit" used a form $A_1^n(x, Q^2) = C_0 x^\alpha (1 + C_1 x + C_2 x^2)(1 + \frac{C_{ht}}{Q^2})$ where C_2 was constrained such that $A_1(x = 1, Q^2 = \infty) \equiv 1$.

(a) $A_1^n(x, Q^2) = -0.126 x^{0.168}(1 + 3.05x - 12.0x^2)(1 - \frac{0.15}{Q^2})$,

    $\chi^2_{/d.f.} = 0.29$;

(b) Variations of the constraint and the functional form of the x dependence of the fit were iterated on the data to characterize possible model dependence.

    i. $A_1^n(x, Q^2) = -0.160 x^{0.234}(1 + 1.83x - 8.45x^2)(1 - \frac{0.16}{Q^2})$,

        $\chi^2_{/d.f.} = 0.33$,

    ii. $A_1^n(x, Q^2) = -0.243 x^{0.407}(1 + 4.38x - 25.8x^2 + 16.3x^3)(1 - \frac{0.18}{Q^2})$,

$$\chi^2_{/d.f.} = 0.97 \ ;$$

(c) Variation of the possible Q^2 dependence of the A_1 fits.

     i. $A_1^n(x, Q^2) = -0.112x^{0.146}(1 + 4.27x - 14.2x^2)(1 - \frac{0.32}{Q^2})$,

     ii. $A_1^n(x, Q^2) = -0.118x^{0.154}(1 + 3.89x - 13.4x^2)$.

6. **Deep inelastic transverse polarized structure functions**

   (for calculating σ_{in}^p, see Eq. 4.3)

   (a) $g_2 = g_2^{WW}$ [19],

   (b) $g_2 = 0$,

   (c) g_2 fit to E154 data,

   (d) $g_2 = g_2^{WW}$ + fit to $\bar{g}_2$ from E154 data ,

   (e) $A_2 = 0$,

   (f) $A_\perp = 0$.

7. **Resonance region polarized structure functions**

   (for calculating σ_{in}^p, see Eq. 4.3)

   $g_1^{^3He}$ is calculated using the proton and neutron structure functions as

   $$g_1^{^3He} = 0.87g_1^n - (2)(0.027)g_1^p,$$

   where 0.87 and 0.027 are the neutron and proton polarizations, respectively.

   (a) Resonance A_1 model written by L. Stuart and tuned to agree with E143 resonance data [60].

(b) Extrapolation of the DIS A_1 model through the resonance region.

APPENDIX B

SYSTEMATIC ERRORS BREAKDOWN

This appendix contains the complete breakdowns of systematic error studies done for E154. The systematic error contributions of each component to g_2^n are presented first. Then Tables B.2-B.5 show the complete breakdown of systematic uncertainties in the radiative corrections as applied to the physics asymmetries $A_{\parallel}$ and $A_{\perp}$.

Overall Systematic Errors on g_2											
Syst.						$\langle x \rangle$					
Comp.	.0174	.0245	.0347	.0491	.0795	.1230	.1730	.2420	.3420	.4400	.5640
P_b	.1610	.0509	.2510	.1270	.0585	.0190	.0036	.0098	.0095	.0016	.0002
P_t	.4770	.1510	.7440	.3750	.1730	.0562	.0107	.0292	.0280	.0049	.0007
f	.3600	.0832	.2480	.1590	.0651	.0288	.0042	.0109	.0286	.0035	.0013
F_2	.1700	.0388	.2310	.1200	.0546	.0182	.0040	.0092	.0088	.0014	.0002
R	.1140	.0363	.3150	.2380	.1800	.0921	.0278	.0899	.1180	.0253	.0062
E'	.1200	.0371	.2940	.1980	.0962	.0548	.0103	.0370	.0613	.0065	.0010
P_n	.1500	.0341	.2090	.1110	.0514	.0173	.0037	.0086	.0080	.0013	.0003
P_p	.0053	.0041	.0031	.0022	.0011	.0002	.0003	.0007	.0008	.0006	.0004
g_2^p	.0282	.0198	.0061	.0030	.0011	.0002	.0007	.0005	.0003	.0002	.0002
RC	1.8300	.9030	.4320	.3160	.1870	.1940	.1440	.0780	.0199	.0034	.0079
Rate	.2310	.1630	.1050	.0625	.0248	.0092	.0055	.0031	.0011	.0005	.0000
A_π	.0007	.0005	.0003	.0002	.0001	.0000	.0000	.0000	.0000	.0000	.0000
π/e	.0700	.0284	.0753	.0401	.0164	.0027	.0005	.0000	.0004	.0000	.0000
A_{e^+}	.0195	.0087	.0047	.0016	.0011	.0005	.0002	.0001	.0005	.0000	.0000
e^+/e^-	.0010	.0023	.0021	.0014	.0003	.0000	.0000	.0000	.0001	.0000	.0000
EW	.1190	.0986	.0781	.0623	.0489	.0369	.0269	.0180	.0104	.0059	.0025
Total	1.9700	.9440	1.0800	.6570	.3660	.2420	.1510	.1320	.1460	.0280	.0105

Table B.1: Contributions to the systematic error on g_2^n for every x-bin. Contributions from the following systems are shown: P_b - beam polarization, P_t - target polarization, f - target dilution factor, F_2 and R - unpolarized structure function calculations, E' - energy measurement, P_n and P_p - neutron and proton polarization in ^{3}He , g_2^p - proton structure function to extract neutron result from ^{3}He , RC - radiative corrections, Rate - rate dependence, A_π - pion background asymmetry, π/e - pion background dilution, A_{e^+} - positron background asymmetry, e^+/e^- - positron background dilution, EW - electroweak asymmetry correction.

Radiative Corrections Errors								
x-bin	Elas. Models	Pauli Models	DIS Unpol.	A_1 Models	g_2 Models	Res. Asym.	Target Models	Misc. Param.
0.017	0.009	0.019	0.045	0.122	0.008	0.000	0.000	0.000
0.025	0.008	0.013	0.040	0.086	0.008	0.001	0.001	0.000
0.035	0.006	0.007	0.032	0.053	0.007	0.000	0.001	0.000
0.049	0.004	0.004	0.024	0.024	0.003	0.000	0.002	0.000
0.078	0.002	0.001	0.014	0.012	0.007	0.000	0.002	0.000
0.122	0.001	0.000	0.006	0.035	0.022	0.000	0.001	0.000
0.173	0.001	0.000	0.001	0.045	0.036	0.000	0.001	0.000
0.240	0.001	0.000	0.002	0.042	0.044	0.000	0.001	0.000
0.340	0.001	0.000	0.001	0.033	0.031	0.000	0.000	0.000
0.424	0.002	0.000	0.001	0.025	0.010	0.000	0.001	0.000

Table B.2: Contributions to the radiative correction error on $A_\parallel$ for the 2.75° spectrometer. All values are in units of 10^{-2}. The models used for each component are shown in Appendix A.

Radiative Corrections Errors								
x-bin	Elas. Models	Pauli Models	DIS Unpol.	A_1 Models	g_2 Models	Res. Asym.	Target Models	Misc. Param.
0.057	0.013	0.014	0.049	0.030	0.008	0.000	0.000	0.000
0.084	0.009	0.008	0.033	0.028	0.017	0.001	0.001	0.001
0.123	0.006	0.003	0.019	0.074	0.024	0.000	0.002	0.000
0.172	0.004	0.001	0.006	0.104	0.035	0.000	0.003	0.000
0.242	0.002	0.000	0.006	0.113	0.046	0.000	0.003	0.000
0.342	0.001	0.000	0.006	0.097	0.039	0.000	0.003	0.001
0.442	0.001	0.000	0.001	0.090	0.016	0.000	0.002	0.001
0.565	0.001	0.000	0.004	0.079	0.078	0.000	0.002	0.001

Table B.3: Contributions to the radiative correction error on $A_\parallel$ for the 5.5° spectrometer. All values are in units of 10^{-2}. The models used for each component are shown in Appendix A.

Radiative Corrections Errors								
x-bin	Elas. Models	Pauli Models	DIS Unpol.	A_1 Models	g_2 Models	Res. Asym.	Target Models	Misc. Param.
0.017	0.007	0.000	0.001	0.002	0.151	0.001	0.001	0.000
0.025	0.005	0.000	0.000	0.002	0.118	0.000	0.000	0.000
0.035	0.003	0.000	0.001	0.002	0.089	0.000	0.001	0.000
0.049	0.001	0.000	0.001	0.001	0.101	0.000	0.000	0.000
0.078	0.001	0.000	0.000	0.001	0.111	0.000	0.000	0.000
0.122	0.000	0.000	0.000	0.001	0.197	0.000	0.000	0.000
0.173	0.001	0.000	0.000	0.001	0.220	0.000	0.000	0.000
0.240	0.000	0.000	0.000	0.001	0.181	0.000	0.000	0.000
0.340	0.000	0.000	0.000	0.001	0.074	0.000	0.000	0.000
0.424	0.001	0.000	0.001	0.002	0.024	0.000	0.001	0.000

Table B.4: Contributions to the radiative correction error on $A_\perp$ for the 2.75° spectrometer. All values are in units of 10^{-2}. The models used for each component are shown in Appendix A.

Radiative Corrections Errors								
x-bin	Elas. Models	Pauli Models	DIS Unpol.	A_1 Models	g_2 Models	Res. Asym.	Target Models	Misc. Param.
0.057	0.005	0.001	0.000	0.002	0.065	0.000	0.000	0.000
0.084	0.002	0.000	0.000	0.001	0.108	0.000	0.000	0.000
0.123	0.001	0.000	0.000	0.001	0.236	0.000	0.000	0.000
0.172	0.001	0.001	0.001	0.001	0.315	0.000	0.001	0.001
0.242	0.000	0.000	0.000	0.001	0.312	0.000	0.000	0.000
0.342	0.000	0.000	0.000	0.002	0.168	0.000	0.000	0.000
0.442	0.000	0.000	0.000	0.002	0.053	0.000	0.000	0.000
0.565	0.000	0.000	0.001	0.002	0.323	0.000	0.001	0.000

Table B.5: Contributions to the radiative correction error on $A_\perp$ for the 5.5° spectrometer. All values are in units of 10^{-2}. The models used for each component are shown in Appendix A.

Elas. Models	Pauli Models	DIS Unpol.	A_1 Models	g_2 Models	Res. Asym.	Target Models	Misc. Param.	Total
0.172	0.180	0.629	0.722	0.520	0.006	0.066	0.009	1.292

Table B.6: Contributions to the integral error on g_1 in the measured region. All values are in units of 10^{-3}. The models used for each component are shown in Appendix A.

APPENDIX C

PARAMETERIZATION OF PAIR-SYMMETRIC CONTAMINATION

OF DIS AT SLAC KINEMATICS

C.1   Introduction

In inclusive deep inelastic scattering (DIS), experimenters are often challenged by the high rates of background processes. These background effects often obscure the underlying physics that is being measured. Motivated by the desire for higher precision, experiments have had to incorporate into their running plans an independent measurement of these background processes. However, since running time is limited, accurate estimates of the background rates are needed to optimize the use of beam time for the acquisition of the physics goals.

At SLAC, electrons are used for fixed target experiments. The detector systems are designed to distinguish non-electron background particles (π^-, K^-, etc.) from the intended electron scattering events. However, one of the largest backgrounds we deal with comes from pair-symmetric productions. In creating electron-positron pairs, these processes provide additional electrons that can enter our detector apparatus and be indistinguishable from an outgoing DIS electron. In the past, a numerical parameterization written by A. Bodek [69] has been used to predict the pair-symmetric background rates. This subroutine was based on older SLAC

data. The current SLAC experiments are now operating at higher beam energies and smaller scattering angles than before. As a result, the Bodek parameterization no longer accurately predicts contamination rates for these experiments. The purpose of this section is to document the creation of a new, physically motivated, parameterization that has been tuned to fit the more recent SLAC data from E142 and E143.

<div align="center">C.2   Measurement</div>

While the creation of a parameterization is fine for prediction of these pair-symmetric effects, we need to be able to measure the actual background rates for the experiment. In the SLAC experiments, we make use of the fact that for every background electron that is produced from this pair-symmetric process, there will be a corresponding positron. If we reverse the polarity of the magnets in our spectrometers, then we will only measure positive particles (e^+, π^+, K^+, ...) instead of negative particles (e^-, π^-, K^-, ...). Since the incoming particles are still electrons, we will no longer measure the primary DIS events. Therefore, by measuring the rates of these outgoing positrons, we are effectively measuring the background rate without the signal.

This measured positron cross section will be dependent on the experiment. Spectrometer acceptance, target characteristics, and experimental kinematics will all have an effect. In order to avoid normalization problems, we can create a ratio between the measured positron (background) rate and the measured electron (reg-

ular measurement minus background) rate. This ratio is also known as a dilution factor.
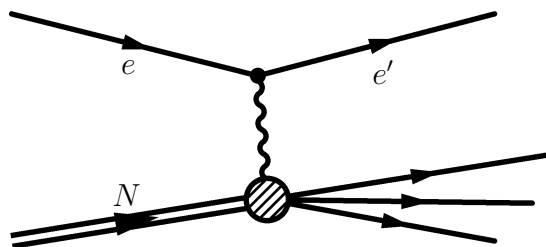
C.3   The Physics

Figure C.1: The standard DIS reaction $eN \longrightarrow e' + X$.

Let us look at some of these non-DIS processes in more detail. The standard DIS interaction that we want to measure can be represented as in Fig. C.1. However, since all we measure are the incoming and outgoing electron energies, an electron from the following interaction would not only be detected by our detectors, but would be impossible to distinguish from the primary electron:

$$eN \longrightarrow \quad \pi^0 \quad + X$$

$$\hookrightarrow \quad \gamma + \gamma$$

$$\hookrightarrow e^+ + e^- \text{ (in conversion material).}$$

In fact, for low outgoing electron energies, the contamination of past measurements due to alternate processes such as this, or the Dalitz decay ($\pi^0 \rightarrow e^+ + e^- + \gamma$), have been as high as 15-20%.

In order to create a parameterization that accurately predicts these backgrounds, we need to understand which processes contribute. There exist several

Monte Carlo simulation programs that can do calculations of known physics effects. One of these simulation programs (PYTHIA [70]) was used by P. Bosted to look at the relative contributions of dominant photo-production processes.

Photo-production concerns the use of a real photon beam. This beam then interacts with a target material to produce electron-positron pairs, pions, kaons, J/Ψ's, etc.. Many of these can decay into final state electrons that will be detected in our spectrometers. For the PYTHIA run shown in Fig. C.2, the incoming photon beam was assumed to have a Bremsstrahlung energy spectrum with a maximum energy of 50 GeV. In low Q^2 ($Q^2 \ll 1\mathrm{GeV}^2$) electron DIS, the virtual photon spectrum is usually approximated by the Bremsstrahlung spectrum equivalent to a $\sim 4\%$ radiator [73]. Therefore, the photo-production processes shown here are a close approximation to what is expected by standard low Q^2 DIS electro-production when the electron goes down the beam pipe. As can be seen in Fig. C.2, the dominant contribution to this non-DIS background comes from the π^0 decay processes described above.

Photo-production processes have been measured previously in experiments at SLAC as well as other labs [71]. As a result, the underlying fundamentals are fairly well understood [72, 73]. First, we know that the photo-production rate must be proportional to some function of the incoming beam energy. The higher the incoming beam energy, the more likelihood that the produced photon will have a sufficiently high energy to produce an energetic electron-positron pair. Second, we know that the pair production rates fall off with increasing transverse momentum,
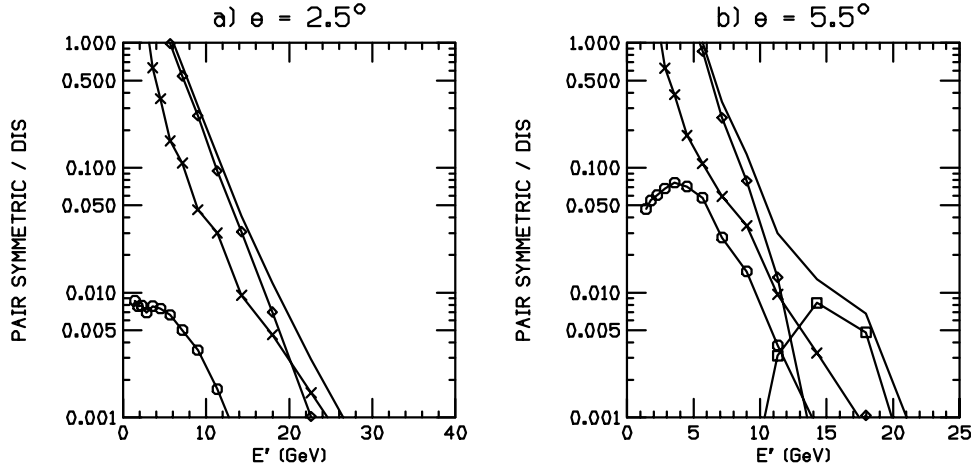
Figure C.2: Results from a PYTHIA run by P. Bosted, showing the various processes contributing to the non-DIS electron background. The ratio of electrons from pair-symmetric processes to Born scattering are plotted versus the outgoing electron energy. Processes shown include: ($\diamond$) π^0 decay; ($\times$) Bethe-Heitler; ($\circ$) Open Charm production; ($\square$) J/Ψ Decay; (—) Sum of all pair-symmetric processes.

since most of the momentum will be in the forward direction. Finally, in contrast to the Dalitz decay mentioned previously, which is independent of target material, pair-production from photons requires some conversion material. As a result we should expect to include parameter for the thickness of the target material most likely to be traversed by the photon in addition to a constant term to account for the Dalitz decays.

C.4   The Parameterization

Monte Carlo simulations, like the one shown above, can be very accurate predictors for experimental data. However, these Monte Carlo simulations rely on models from previous data. The current experiments are operating at energies for which these models are not necessarily accurate. To improve the accuracy of predictions for the current kinematic range, a fast subroutine using a parameterization

in terms of beam energy, angle, and target thickness (POSRATE.F) was created. This parameterization uses a fit to the measured data from E142 and E143. For this discussion we use the following definitions:

$$E_0 = \text{incident electron beam energy in GeV,}$$

$$E' = \text{outgoing electron energy in GeV,}$$

$$\theta = \text{electron scattering angle in degrees,}$$

$$P_T = E' \sin(\theta) \ \text{(transverse momentum of the outgoing electron),}$$

$$R_l = \text{effective radiation lengths traversed after the scatter,}$$

$$\sigma^{e^-} = \text{measured electron cross section,}$$

$$\sigma^{e^+} = \text{measured pair production cross section,}$$

$$\sigma_{DIS}^{e^-} = \sigma^{e^-} - \sigma^{e^+} \ \text{(electron DIS cross section).}$$

Recall that the measured data are used as a ratio of positron to electron cross sections to eliminate normalization effects, while the physics observations mentioned above were related only to the positron production cross section due to electro-production processes. To compare the E142 and E143 data sets in a global fashion, which would still be valid for the E154 kinematics, the measured ratios were normalized to the model for the electron DIS cross section ($\sigma_{model}^{e^-}$) calculated from the subroutines F2NMC [1] and R1990 [2] using

$$\sigma_{norm}^{e^+} = \left(\frac{\sigma^{e^+}}{\sigma_{DIS}^{e^-}}\right)_{meas.} \times \sigma_{model}^{e^-}.$$

Using these data and an exponential fit, the parameterization then has the form:

$$\frac{d\sigma^{e^+}}{d\Omega dE'} = E_0^2 * 10^{(a_0 + (a_1 * R_l) + (a_2 * P_T))} \quad (\text{nb/sr/GeV})$$

where the fit parameters (a_n) were determined to be:

$$a_0 = -0.8908,$$

$$a_1 = 8.809,$$

$$a_2 = -2.856.$$

This fit was determined empirically. The simplest parameter to work with was found to be the positron cross section divided by the square of the incoming beam energy $(\sigma_{norm}^{e^+}/E_0^2)$. Fig. C.3 shows this quantity plotted logarithmically against the transverse momentum (P_T) for both experiments and all targets. As plotted, a simple linear fit can be made to these data.

There are a few points to be noticed. First, the E142 data appears to be a little less consistent with the fit. There are several possible reasons why the E142 data may be more difficult to parameterize. E142 was the very first experiment to use the current spectrometer configuration. As a result the optimization was not
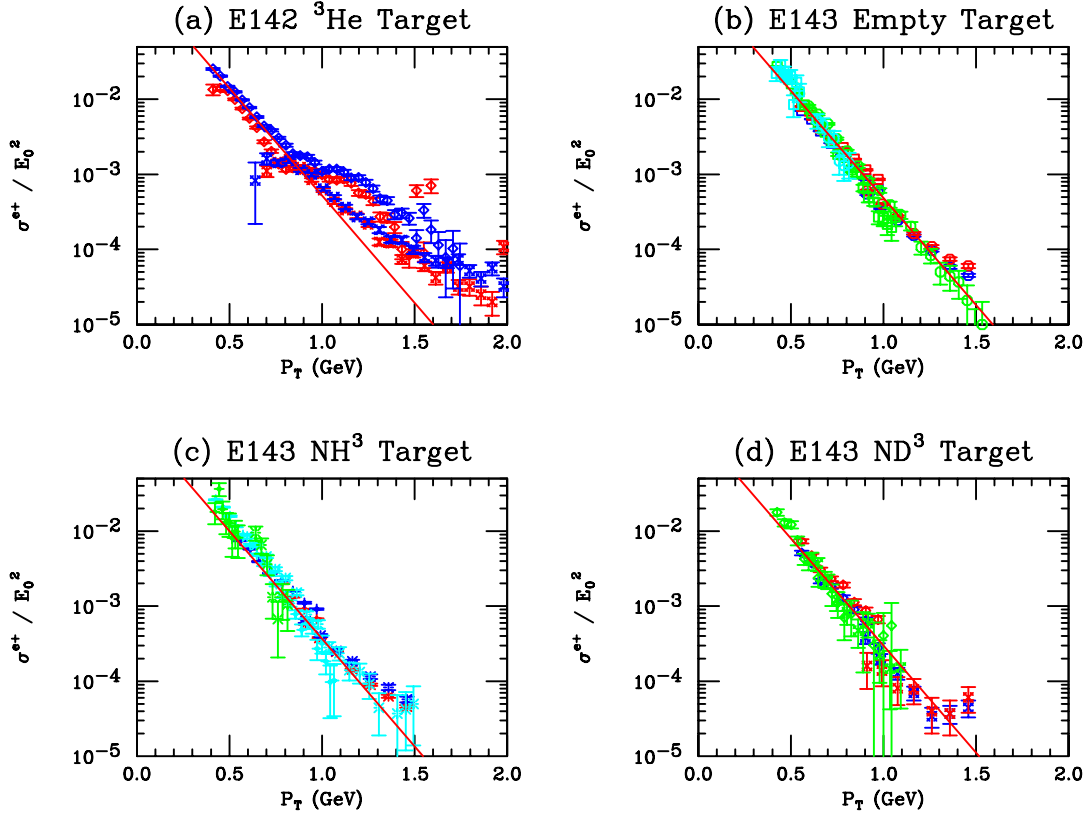
Figure C.3: All of the data used to make the positron fit. Each plot contains all data from both spectrometers (4.5° and 7.0°) and all energies (25 and 22 GeV for E142; 29, 16, and 9 GeV for E143) for the indicated experimental setup. The plotted lines correspond to the parameterization predictions for the appropriate target thicknesses.

as good. In general, less time was spent on the positron data, both experimentally and later during the analysis. Also, the E142 target setup suffered from a design flaw that included the NMR pickup coils in the acceptance of the spectrometers. As a result, the value for R_l is much more complicated than the simple average that was used for this analysis. Also notice that on almost every plot, the data begin to diverge from the linear fit at high P_T. This may correspond to signal contamination in the Cerenkov counters due to high energy pions that look like electrons.

The subroutine requires input of the parameters E_0, E', θ, and R_l. P_T is then calculated and used in the parameterization listed above to get the estimated

positron rate. As above, an estimate of the electron rate is calculated using the subroutines F2NMC [1] and R1990 [2]. The ratio of these two rates is then returned.

C.5   Results

This parameterization was based solely on the measurements from E142 and E143 which achieved maximum beam energies of 29 GeV. It was used to predict the positron contamination for E154 which had an incident beam energy of 48 GeV. In Fig. C.4, the E154 data is plotted relative to the original fit result from the E142 and E143 data. As can be seen the agreement is very good in the lower x regions. The deviations at higher x are consistent with the Cerenkov threshold for pions and decays from J/Ψ's, which dominate for $P_T > 1.5$ GeV.
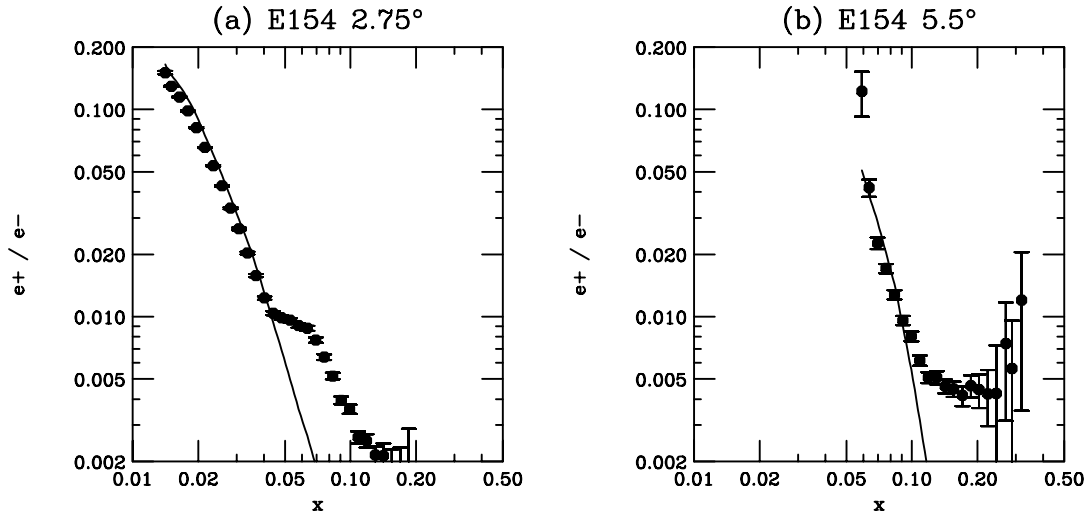

Figure C.4: E154 positron data. The ratio of measured positron rates to measured DIS electron rates (as defined on p. 117) are plotted vs. x. The line corresponds to the prediction from the parameterization assuming a target conversion thickness of $R_l \approx 0.015$ radiation lengths. The ratio plotted can be compared to the dilution parameter R^+ used in Sec. 3.3.2 by using Equation 3.8.

This parameterization worked very well for E154 and was used to help design

the most recent experiment, E155. However, there is still room for improvement. The dependence on the conversion thickness of the target has been implemented in an ad hoc way. Now that we have 4 experiments (E142, E143, E154, and E155) that all used very similar setups, but had different targets, it would offer a very good chance to do a careful study of the target-dependent effects. Overall, the fundamental P_T dependence looks very good in the regions where the signal is not contaminated by pions. For the purpose of experimental run plan design, where predictions on the order of 20% relative accuracy are needed, the parameterization appears to be quite reasonable.

BIBLIOGRAPHY

[1] M. Arneodo et al., Phys. Lett. **B364**, 107 (1995).

[2] L.W. Whitlow, et al., Phys. Lett. **B250**, 193 (1990).

[3] D. Adams, et al., Phys. Rev. **D56**, 5330 (1997).

[4] M.Anselmino, A. Efremov, and E. Leader, Phys. Reports **261**, 1 (1995).

[5] R.L. Jaffe, Phys. Rev. **D11**, 1953 (1975).

[6] R.L. Jaffe and X. Ji, Phys. Rev. **D43**, 724 (1991).

[7] A.W. Schreiber, A.I. Signal, and A.W. Thomas, Phys. Rev. **D44**, 2653 (1991).

[8] M. Stratmann, Z. Phys. **C60**, 763 (1993).

[9] X.M. Wang and X. Song, Phys. Rev. **C51**, 2750 (1995).

[10] X. Song, Phys. Rev. **D54**, 1955 (1996).

[11] K.G. Wilson, Phys. Rev. **179**, 1499 (1969).

[12] M.E. Peskin and D.V. Schroeder, An Introduction to Quantum Field Theory, (Addison-Wesley Publishing Co.), 631 (1995).

[13] M.A. Shifman, A.I. Vainshtein and V.I. Zakharov, Nucl. Phys. **B147**, 385 (1979).

[14] I. Balitsky, V. Braun and A. Kolesnichenko, Phys. Lett. **B242**, 245 (1990); **B318**, 648 (1993) Erratum.

[15] B.L. Ioffe, Nucl. Phys. **B188**, 317 (1981).

[16] E. Stein et al., Phys. Lett. **B343**, 369 (1995).

[17] J.M. Drouffe and C. Itzykson, Phys. Reports **C38**, 133 (1978).

[18] M. Göckeler et al., Phys. Rev. **D53**, 2317 (1996).

[19] S. Wandzura and F. Wilczek, Phys. Lett. **B72**, 195 (1977).

[20] H. Burkhardt and W.N. Cottingham, Ann. Phys. **56**, 453 (1970).

[21] R.L. Heimann, Nucl. Phys. **B64**, 429 (1973).

[22] L. Mankiewicz and Z. Rysak, Phys. Rev. **D43**, 733 (1991).

[23] J.L. Cortes, B. Pire and J.P. Ralston, Z. Phys. **C55**, 409 (1992).

[24] R. Erickson et al., SLAC-PUB 7177 (1996) and Proc. of Fifth European Acc. Conf. (1996).

[25] H. Band et al., E154 Technical Note 40 (1996), unpublished.

[26] T.E. Chupp et al., Phys. Rev. **C36**, 2244 (1987).

[27] H. Middleton, Ph.D. thesis, Princeton University, (1994) unpublished.

[28] T. Smith, Ph.D. thesis, University of Michigan, (1997) unpublished.

[29] M. Romalis, Ph.D. thesis, Princeton University, (1997) unpublished.

[30] R.M. Woloshyn, Nucl. Phys. **A496**, 749 (1989).

[31] C. Ciofi degli Atti, private communication.

[32] L. Frankfurt, V. Guzey, and M. Strikman, Phys. Lett. **B381**, 379 (1996).

[33] T. Agaki, E154 Technical Note 7 (1995), unpublished.

[34] G.T. Bartha et al.,Nucl. Instr. and Meth. **A375**, 59 (1989).

[35] H.R. Band, AIP Conf. Proc. **343**, 245 (1994).

[36] C. Møller, Ann. Phys. (Leipzig) **14**, 532 (1932).

[37] P.L. Anthony and Z.M. Szalata, Report No. SLAC-PUB-7201 (1996) unpublished.

[38] S. Churchwell, Ph.D. thesis, U. Mass. Amherst (1998).

[39] Y. Kolomensky, M. Olson, and P. Zyla, E154 Technical Note 55 (1997) unpublished.

[40] V. Breton et al., Nucl. Instrum. Methods **A362**, 478 (1995).

[41] P.E. Bosted, E154 Technical Note 29 (1995) unpublished.

[42] T.V. Kukhto and N.M. Shumeiko, Nucl. Phys. **B129**, 412 (1983).

[43] N.M. Shumeiko, Private Communication (corrections to errors in previous paper).

[44] I.V. Akushevich and N.M. Shumeiko, J. Phys. G: Nucl. Part. Phys. **20**, 513 (1994).

[45] M. Gari and W. Krümpelmann, Z. Phys. **A322**, 689 (1985).

[46] G. Höhler et al., Nucl. Phys. **B114**, 505 (1979).

[47] F. Iachello et al., Phys. Lett. **B43**, 191 (1973).

[48] J.G. Korner and M. Kuroda, Phys. Rev. **D16**, 2165 (1977).

[49] A. Lung, et al., Phys. Rev. Lett. **70**, 718 (1993).

[50] S. Galster, et al., Nucl. Phys. **B32**, 221 (1971).

[51] S. Blatnik and N. Zovko, Acta Phys. Austriaca **39**, 62 (1974).

[52] S. Stein et al., Phys. Rev. **D12**, 1884 (1975).

[53] DeForest and Walecka, Adv. in Phys. **15**, 1 (1966).

[54] W. Van Orden, PhD. Thesis, Stanford University (1978).

[55] L.W. Whitlow, et al., Phys. Lett. **B282**, 475 (1992).

[56] A. Bodek, et al., Phys. Rev. **D20**, 1471 (1979).

[57] L. Stuart, et al., SLAC-PUB-7391 Submitted to Phys. Rev. **D**, (1996).

[58] McCarthy, et al., Phys. Rev. **C15**, 1396 (1977).

[59] Arnold, et al., Phys. Rev. Lett. **40**, 1429 (1978).

[60] K. Abe et al., SLAC-PUB-7242 Accepted by Phys. Rev. Lett., (1996).

[61] Y.S. Tsai, SLAC-PUB-848 (1971).

[62] H. Olsen and L.C. Maximon, Phys. Rev. **114**, 887 (1959).

[63] M. Romalis and Y. Kolomensky, E154 Technical Note 54 (1997) unpublished.

[64] Y. Kolomensky, thesis, U. Mass. Amherst (1997).

[65] M. Olsen, thesis, Kent State U. (1998).

[66] R. Arnold, et al. SLAC-Proposal-E155 Extension (1997).

[67] K. Abe, et al. Phys. Lett. **B404**, 377 (1997).

[68] L. Rochester et al., Phys. Rev. Lett. **36**, 1284 (1976).

[69] Fortran subroutine EPLUS.F written by A. Bodek and P. Bosted.

[70] T. Sjostrand, Computer Physics Commun. **82**, 74 (1994).

[71] D. Wiser, Ph.D. thesis (1977).

[72] D. Sivers, S. Brodsky and R. Blankenbecler, Physics Reports **23**, No. 1 (1976).

[73] Y. Tsai, Rev. Mod. Phys. **46**, 815 (1974).